PERMEABILITY AND PORE STRUCTURE OF GRANULAR MATERIALS

Permeability and pore structure of granular materials

By **YAQIAN LIU,** B.Sc., M. Eng.

A Thesis

Submitted to the School of Graduate Studies in Partial Fulfillment of the Requirements for the Degree Doctor of Philosophy

McMaster University

DOCTOR OF PHILOSOPHY (2015) McMaster University

(Civil Engineering) Hamilton, Ontario

TITLE: Permeability and pore structure of granular materials

AUTHOR: Yaqian Liu, B.Sc., M.Eng.

SUPERVISORS: Professor Peijun Guo, Professor Stan Pietruszczak

NUMBER OF PAGES: xii, 191

Abstract

The influence of the microstructure on the permeability of porous media is very important for various engineering problems in different engineering disciplines. The challenges for research in this area include the characterization and the quantification of microstructure as well as proper involvement of such microstructure measures in mathematical models with clear physical meaning. This study focuses on the reconstruction of pore structure of porous materials, the quantitative description of pore structure using second-rank fabric tensors, as well as the determination of permeability as a function of microstructural measures via different approaches, including laboratory tests, theoretical analysis and numerical simulations.

This research is centred on the quantification of pore structure of porous materials. A procedure is established to reconstruct the microstructure of a porous material using 3D CT-scan images. A new algorithm is developed to quantify the internal structure based on the 3D CT-scan images. More specifically, two fabric descriptors, Mean Intercept Length and Areal Pore Size, are employed to construct fabric tensors as measures for the internal structure. The developed procedure and algorithm are verified for difference scenarios and then used to determine the internal structures of different materials.

An analytical model is developed to describe flow in porous medium with internal structures using the technique of homogenization. With the fluid-solid interaction taking into account on the particle level, the permeability tensor of a porous medium is derived from the macroscopic momentum balance equation of the fluid. The microstructure of the

porous media is taken into account using the fabric tensors (based on both the Mean Intercept Length and Areal Pore Size) obtained from 3D microstructure reconstructions. When interpreted in the classical meaning, the two tensors describe the directional dependency of the tortuosity and hydraulic diameter, respectively. The well-known Kozeny-Carmman model is recovered for isotropic materials.

In addition to the directional variation of mean pore sizes, the variation of pore size distribution in different directions also affect the permeability of porous materials. Pipe Network Models are used to explore the influence of pore size variation on the permeability of granular materials. A new algorithm is developed to compute the pore size distribution and its variation in different directions in porous media using the CT-scan images. When taking into account the directional variation of pore size distributions, Pipe Network Models can be used to determine the principal permeability of an anisotropic porous material. The success of this approach highly depends on reliable characterization of pore structures

To verify the theoretical and numerical approaches developed in this research, laboratory tests are carried out to obtain the permeability of different materials. To determine the anisotropy of permeability of granular materials with internal structure, a new permeameter is developed to allow the hydraulic conductivity of cohesionless materials to be measured when flow takes place in any direction relative to bedding plane of the specimens. Materials with different type of particle shape and particle size distributions are examined using this permeameter. Good agreements are obtained from comparisons of laboratory test results with theoretical models and numerical simulations.

Acknowledgements

I would like to begin by thanking my supervisor Professor Peijun Guo, for providing me the opportunity to pursue my Ph.D. and the continuous support on my research work and every aspect of my life. This thesis would not have been possible without his endless help over the years. I am also greatly grateful to my co-supervisor Professor Stan Pietruszczak for his precious instructions on my study. Appreciation is extended to the other members on my supervisory committee, Professor Samir Chidiac and Professor Marek Niewczas for their encouragement and comments on my work. Special thanks go to Professor Gyan Pande at Swansea University for his insightful guidance in the theory of Pipe Network Model.

Appreciation is especially extended to Mr. Peter Koudys for his enduring and unending help on my numerous laboratory tests. He helped design and make a number of key devices used in this study. It is his expertise that makes the experimental ideas come true. I also want to thank Jing Li and Yaping Lv for their assistance to perform the CT tests using the scanner in their department. Thanks to Dr. Tom Chow at Juravinski Cancer Centre for letting me use the CT scanner in their lab. I am also grateful to all my friends at McMaster University. It is you who make my life here so wonderful!

I would like to acknowledge the financial support from China Scholarship Council, National Sciences and Engineering Research Council and the Department of Civil Engineering, McMaster University.

To my family.

Table of Contents

Table of figures

List of tables

Chapter 1 Introduction

1.1 Background and motivation

Porous media can be viewed as a collection of particles or interconnected solid skeleton. The free space among particles or within solid skeleton provides the possibility that the second phases could move through it. Furthermore, the pore space is also a key factor that affects other properties of the material, e.g., strength, thermal conductivity, permeability and so on. Depending on what kind of physical process being investigated, numerous materials could be considered as porous media or pure "solid" under different circumstances. For instance, in agriculture irrigation problem, sandstone is usually seen as impermeable, i.e., pure solid. However, under high fluid pressure, the fluid may flow through the media and the pores cannot be neglected anymore. Therefore, the definition of porous media must be discussed in a certain size scale and is very much problem dependent. In this study, a material is regarded as a porous medium when another material phase or physical property (such as heat, electrical current) can move through it.

Depending on the compositing particles, the forming process and also the following geological processes, the porous structure may take different form which has great influence on the properties of the media. For instance, the minerals of clay tend to form a sheet-like structure. However, granular soils are more like Lego-packing structure. Fig.

1.1 shows an example of different structures formed by various particles in a wide range of size and shape.

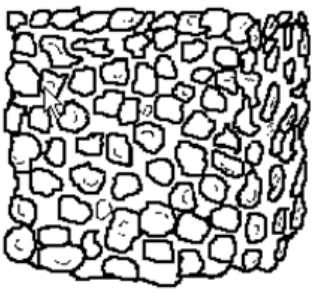

Granular: Similar to cookie crumbs and the size of the particle is usually smaller than 0.5cm.

Blocky: Blocks of which the shape is irregular and the diameter ranges from 1.5 to 5.0cm.

Prismatic: Vertical columns of soil with length being a number of centimeters long.

Columnar: Vertical columns of soil with a salt "cap".

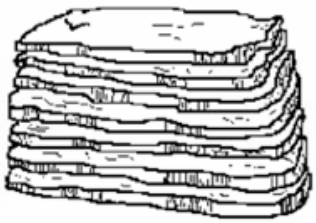

Platy: Thin, flat plates of soil with horizontal stratification.

Single grained: Soils that have very little or no consistency. The grains do not stick together.

Fig. 1.1 Different type of aggregates with different internal structure （Lowenfels and Yayne, 2010）

Three basic branches of transport problem including momentum, heat and mass transfer have been developed for a long time. These research results can found their applications in traditional engineering practices. Momentum transport can also be called fluid dynamics which usually deals with the fluid/gas flow with a certain type of

boundaries. It has a wide range of applications such as calculation forces and moments on aircraft, determining the mass flow rate of oil through pipelines. Some of the theories are even applicable in traffic engineering where the vehicles are viewed as the flowing fluid and the traffic facilities are treated as the permeating media. Mass transfer is defined as the net movement of a stream/material phase/fraction or a component from one location to another. It can be found in many processes, e.g., absorption, evaporation, drying, membrane filtration and distillation. The application includes the study of blood purification in kidneys or liver, the separation of chemical components in distillation columns, absorbers such as activated carbon beds. Heat transfer is actually the exchange of thermal energy between contacting systems or within a single system. The process depends on the temperature gradient which is very similar with fluid flow in fluid dynamics (Tiedje and Guo 2014).

Although these three problems are different in physical processes, they share great similarity in the mathematical equations and solutions. A systematic unified study has been comprehensively reviewed by Bird et al. (2007). Based on this fact, any advancement in one field has the possibility to be applied in the other two research areas. In this research however, focus will be mainly placed on the micro- and macro-level of fluid flow through porous media.

The most successful research achievement investigating the hydraulic properties of

porous media is probably Darcy's law which was formulated by Henry Darcy's experimental results (Darcy, 1856). The law acts as a constitutive equation between two vectors, viz., pressure gradient and velocity of fluid flow. The bridge between those vectors is the hydraulic conductivity or a second order tensor if the equation is expressed as a generalized form. Even after more than 150 years, it is still being used in the areas of earth sciences, hydrogeology, oil production etc. It resembles the Fourier's law in heat conduction problem, Ohm's law in electrical networks problem or Fick's law in diffusion theory. However, Darcy's law is still a phenomenological model leaving the hydraulic conductivity to be determined by running direct permeability tests.

Since the intrinsic permeability of a specific specimen should solely be a function of the structure, there should be a relationship between these two. Kozeny (1927) is the first researcher who established a relationship between the physical properties describing the structure of the media. After his work, a large number of engineers and researchers have attempted to solve this problem in different ways and express the permeability tensor with regard to different quantities including porosity, pore size distribution, particle size distribution etc.

When the Darcy's law is expressed in a generalized form, it implies that the medium could be anisotropic in regard of hydraulic conductivity properties. However, to this day, there is still no solid conclusion on how to calculate the hydraulic conductivity based on

the microstructure information. The difficulties not only come from the theoretical derivation itself, but also stem from the task of quantifying the microstructure of a porous medium.

In the past, some indirect tests can be done to obtain some information of the pore structure. For instance, mercury injection tests could be performed on sandstone to analyze the pore size distribution of a specimen. However, mercury itself would raise the toxic concern and also it is almost impossible to apply high mercury pressure on cohesionless porous media and low strength cemented material such as sand and clay respectively. Recent development on non-destructive detection techniques such as Computed Tomography (CT), Scanning Electron Microscope (SEM) make it possible to obtain more detailed information regarding the microstructure with a very high level of resolution.

Furthermore, the theoretical development on the process of homogenization is becoming a very promising tool to construct the bridge between the microstructure and the macro-level behaviour of fluid flow through porous media. To name a few, Whitaker (1986) derived the Darcy's law from the Navier-Stokes equations from a pore level to macro-level. Dullien (1975), Bear and Bachmat (1990) defined a tortuosity tensor which is a key factor calculating the anisotropic permeability of a medium. However, the definition is not unique among researchers. Moreover, how to quantify this tensor from

experimental data still remains a question.

Under certain loading condition, the pore structure of an isotropic medium may become anisotropic which in turn will affect the permeability of the medium. This is termed as induced anisotropy compared to inherent anisotropy. An initially anisotropic medium may become more “anisotropic” or less. It might be of interest in oil recovery operation to predict how the permeability changes during loading process. Unfortunately, there are very few reliable experimental or theoretical results to implement this work.

1.2 Research objectives and scope

The research objective of this study is to establish an integrated methodology to evaluate the hydraulic conductivity properties of porous media, especially those made of cohesionless materials. The study will facilitate the prediction of permeability using non-destructive techniques. To this end, the focus of this research will be placed on the following aspects:

1) Experimental studies on porous media made of cohesionless materials. New permeameter need to be devised to achieve this goal. Routine test procedures are also required to ensure the repeatability of the tests. Non-destructive techniques will be used to obtain the microstructure of the samples which represent the ones used in permeability tests;

2) Quantification of the microstructure of the sample. Image processing and analysis techniques will be employed and implemented.

3) Development and verification of analytical model on the evaluation of anisotropic permeability of porous media. The model must be able to connect the microstructure and permeability anisotropy.

4) A simple yet quiet accurate method of numerical simulation.

1.3 Outline

In Chapter 2, a comprehensive literature review is made on the key aspects of this research, including the experimental methods determining the anisotropic permeability of samples made of cohesionless materials, the advancement in non-destructive detection methods and their application in geotechnical engineering practices, the theoretical development of analytical models on predicting hydraulic properties of porous media, and the theoretical background of Pipe Network Model and its applications.

Chapter 3 will focus on the design of a new permeameter and the experimental studies utilizing this device to obtain the anisotropic permeability of cohesionless materials. A newly adapted tri-axial test procedure is presented to capture the variation of permeability of samples during loading process.

In Chapter 4, the emphasis will be placed on the quantification of the microstructure

of the investigated materials. Image analysis is implemented using Matlab to process the CT images and reconstruct the internal structure. The microstructure will be expressed in fabric tensors which are defined by different fabric descriptors.

The mathematical development of an analytical model is derived in Chapter 5. The techniques of homogenization are employed to fill the gap between the micro-level behaviour of fluid and that in a macro-level. Fabric tensors which have been obtained in Chapter 4 are incorporated into this model to construct the bridge.

In Chapter 6, a simple yet accurate Pipe Network Model (PNM) is discussed to numerically simulate the fluid flow in porous media. Image analysis is again utilized to obtain the pore size distribution information which is the critical input of PNM. However, the method differs from that in Chapter 4 in that not only the average pore size is obtained, but also the deviation from the mean value is attained. This chapter provides an integrated methodology of computing the permeability of porous media based on micro-CT scans.

Finally, Chapter 7 concludes this research and gives some suggestions for future work.

Chapter 2 Literature review

Comprehensive literatures covering the topics discussed in Chapter 1 are reviewed in this chapter.

2.1 Permeability tests on porous media made of cohesionless materials

It is widely accepted that most geo-materials exhibit anisotropic hydraulic property, no matter it is rock, cohesive soil or cohesionless soil (Bolton et al. 2000; Li et al. 2014; Chapuis and Denis 1989). Anisotropy of porous media is mainly a result of the shape, alignment and packing patterns of the particles. The hydraulic anisotropy, on the other hand, is affected by the voids created by the particle packing, i.e., the size, shape, arrangement and connectivity of the voids. This property is important in many field of study and engineering practice, e.g., water filtration, agricultural irrigation, the contaminant solute transport problem, nuclear waste storage and disposal safety, fluid-injection oil recovery planning, etc.

Numerous prediction models have been put forward by researchers in the past hundreds of years (Kozeny 1927; Bear 1972; Guo 2012; Pietruszczak and Pande 2012). However, the most reliable data still come from experimental results and all prediction models need to be verified by laboratory results. Therefore, it is very important to

measure the hydraulic conductivity of a material in different directions. Permeability tests on rocks and cohesive soils which can be cut into any shape are relatively easier to be performed in different directions (Chapuis and Gill, 1989). However, regular permeability tests on specimens made of cohesionless materials are difficult to be conducted when the direction of flow differs from the principal directions of the microstructure of the specimen. In the following sections, different techniques proposed by researchers to attack this problem are reviewed.

The anisotropic permeability can be represented by a second order, symmetric tensor (Liakopoulos 1956). Due to the difficulty of making samples with inclined bedding planes, most laboratory permeability measurements on cohesionless materials are made along principal directions. The permeability tensor is constructed and the degree of anisotropy can be evaluated based on the principal values. One group of this type of experiments and the corresponding devices are discussed below.

2.1.1 Direct measurements

Latini (1967) developed a rectangular permeameter with four walls made of permeable material which can act as porous stones or be blocked acting as impermeable walls. Two of them are on opposite faces but parallel to the bedding plane of the sample and the other two are perpendicular to the bedding plane. The remaining two walls are solid with piezometers which can be used to measure the head during flow. Once a

sample is made, two facing porous walls are blocked as impermeable walls and the pressure gradient is applied on the other two porous walls. In this way, the permeability along one direction can be measured. After that, the "roles" of those two pairs of porous walls are switched to measure the permeability along the direction perpendicular to the previous one. The advantage of this permeameter is that the permeability along orthogonal directions is measured on the same sample therefore the results are reliable. However, the operation of switching flow direction could be very tricky and most of the time the sample might be disturbed. Also, when the flow is along horizontal direction, lateral leakage between the top wall and the material is hard to control.

2.1.2 Indirect measurement

Indirect measurements usually take advantage of the simultaneous two or three dimensional flow. Flow net and governing equations are used to obtain the anisotropy ratio of permeability. Fontugne's (1969) apparatus is one example of this kind. This device is similar to the regular cylinder permeameter. The difference is that this one has two outlets across from one another on the vertical wall. In this manner, the horizontal flow can also be measured. By solving the flow equations numerically, different flow nets when the anisotropy ratio changes can be obtained. Comparing the test data and the numerical results, the anisotropy ratio can be determined. The question is to what extent the numerical results can resemble the real experimental results since all the assumptions

and boundary conditions are ideal scenarios? This is probably the reason that prevents it becoming popular in this area of research. Another permeameter of this kind was developed by Moore (1979).

Renard et al. (2001) proposed a prototype of a tensorial permeameter which they claim to be able to determine the full permeability tensor. This permeameter is a cubic box with each face connected to piezometers. A number of constant head permeability tests were performed with each test having different selected inlet and outlet boundaries. By conducting least square analysis using the head gradient and discharge data obtained from different tests, the full permeability tensor can be computed. This method has advantages that it is not necessary to know the principal directions of the permeability tensor before the test. However, due to the uncertainty of the head gradient measurement, the experimental results are not as good as they expected.

2.1.3 In-situ determination

All kinds of in-situ tests including pumping tests (Weeks 1969; Escobar 2008), tracer tests (Kenoyer 1988;), slug tests (Shinohara and Ramery 1975; Mas-Pla et al. 1997; Escobar 2008), seismic wave test (Parra 2000) etc. were developed to measure the hydraulic anisotropy on in-situ soils. These tests are important in obtaining aquifer hydrologic properties and the study of water/oil flow and contaminants transportation problems. However, they do have some disadvantages when comparing with indoor

laboratory tests. The first one is that almost all the in-situ tests assume that the soils are fully saturated which is not always true in natural conditions. The second one is that the interpretation of the test results is not intuitive and usually needs the aid of numerical simulation or flow net construction. This leads to the non-uniqueness of the results due to theory differences employed (e.g., Mas-Pla et al. 1997). The third one, some of them can only give an estimation of the anisotropy ratio but absolute permeability values are not available.

2.2 Permeability anisotropy ratio

The anisotropy of hydraulic permeability of granular soil has a significant influence on the water flow and pore pressure distribution, and hence on the deformation and failure of geotechnical structures. In general, homogeneous natural soil deposits have higher permeability in the horizontal direction than that in the vertical direction, owing to the cross-anisotropic internal structure formed during the deposition process of soil. The permeability anisotropy is characterized by the permeability ratio defined as $r_k = k_h / k_v$.

According to the analysis of Chapuis and Gill (1989) on more than 100 experimental measurements of permeability ratios, together with the test results of Chapuis et al. (1989), Rice et al. (1970), and Leroueil et al. (1990), the hydraulic anisotropy of homogeneous clays, sands and sedimentary rocks are comparable. More specifically, the $r_k = k_h / k_v$ ratio, which is related to the shape of particles, their arrangement, or the directional

tortuosity within the pore space, seems to be lower than 4. In particular, for granular materials, the experimental r_k values are in the range of 0.75 to 4.1, with 95% of the r_k values being reported at 2.1 ± 0.5. According to most experimental results, the anisotropy ratio of cohesive soils is in the 0.7 to 4 range, with $r_k = 1.6 \pm 0.4$ for 95% of the cohesive media. These findings suggest a practical upper limit of $r_{k\max} = k_{\max} / k_{\min} = 2.5$ for engineering soils. The test results also show that the $r_k = k_h / k_v$ ratio tends to increase with density, and the degree of permeability anisotropy decreases at high void ratios. These findings are generally consistent with that by Freeze and Cherry (1979), who observe that anisotropy ratios measured in small sediment core samples are commonly in the rage of 1 to 3, and Mitchell and Soga (2005) who suggest an average hydraulic conductivity ratio of about 2 as a result of microfabric anisotropy for many clays. It should be noted that higher $r_k = k_h / k_v$ values in laboratory tests may be a result of microstratifications, as observed by Leroueil et al. (1990) in tests on varved clay. Moreover, heterogeneous layers in large scale domains may have the effect of increasing macroscale anisotropy ratios to as much as 1000 or more (Freeze and Cherry, 1979).

More recently, flow simulations of computer-generated particle packs using different algorithms have been used to predict macroscopic transport in anisotropic porous media by taking into account the effect of microscopic pore structures. Various computer simulation approaches are developed to construct packing of particles to model porous medium that

consists of spherical particles, oblate ellipsoids and irregular particles. The Lattice Boltzmann Method (LBM) is usually used to model flow through granular assemblies.

Using the LBM to model flow through granular assemblies, the results show that the r_k ratio approaches approximately 3.5 when the aspect ratio $AR \geq 4$ with the porosity varying between 0.46 and 0.67. The LBM modelling results by Stewart et al. (2006) for random packs of mono-sized oblate ellipsoids yield $r_k = 1.95$, 3.21 and 7.72 for assemblies (porosity = 0.42-0.49) of ellipsoids having the aspect ratio of 3, 5 and 10, respectively. It should be noted that granular soils consisting of elongated particles with aspect ratio of 10 are rarely encountered in engineering practice. Koza et al. (2009) adopt LBM to model flow through granular assemblies of randomly distributed square particles. The results of 340 simulations follow normal distribution $\langle 1/r_k \rangle = 0.7$, $\sigma_k = 0.12$. The probability of $1/r_k < 0.4$ is 0.005, which implies that $r_{k\max} = 2.5$ can be practically considered as the upper bound of permeability ratio. Galindo-Torres et al. (2012) examine the permeability anisotropy of artificially constructed granular assemblies using the Voronoi tessellation method. The granular medium consists of a set of polygonal particles of different aspect ratios *AR* varying from 1 (isotropic) to 5 (anisotropic). The Voronoi construction ensures a random distribution of different size particles.

Using X-ray computed tomography (CT) technique to acquire real three-dimensional pore structures of material specimens, Masad et al. (2000) simulate flow in three granular

materials (Ottawa sand, glass beads and a silica sand) and observe minor permeability anisotropy with $r_k = 1.10$ to 1.67. In addition to tests on natural porous and granular materials, artificial granular materials are also used to measure the permeability anisotropy. In particular, to investigate the effect of flatness and orientation of particles, Witt and Brauns (1981) perform laboratory permeability tests on oriented arrays of uniform lenticular particles (flat lead lenses), with average values of diameter and height being 6.3 mm and 1.5 mm, respectively. For dense samples with porosity $\phi = 0.40 - 0.41$ (very close to minimum porosity) prepared by sedimentation, the measured average permeability ratio is $r_k = 2.3$. They conclude that even for a high degree of particle-flatness, the permeability-anisotropy barely exceeds a factor of about 2.5.

Following the well-known Carman-Kozeny equation (Carman, 1937), the permeability-anisotropy factor is equal to the square of the ratio of the pore-channel tortuosity. As a result, the existence of the maximum r_k ratio can be alternatively investigated by examining the tortuosity. By considering the tortuosity of granular media as a geometrical quantity, Witt and Brauns (1981) show theoretically that, in the case of non-spherical particles, the ratio of the maximum and minimum tortuosity in a granular assembly is no larger than $\sqrt{2.5}$. The recent work by Alam et al. (2006) shows that, for dense packings (at the porosity of 0.31) of non-deformable *quasi-random* monodisperse plate-like particles with the aspect ratio of 6.52, the values of tortuosity are mostly less than

1.5. When the particle plates are parallel, the tortuosity tends to vary between 1 and 2, and the high tortuosity is observed when flow is perpendicular to the plates. The scatterness of the tortuosity values reflects the effect of the internal directional variation of particle distribution. Similar results can be found in Galindo-Torres et al (2012). The findings regarding the directional tortuosity are generally in agreement with the argument that the maximum permeability anisotropy ratio is approximately 2.5. It should be noted that tortuosity may be viewed as a fudge factor in macroscopic transport equations to take into account the complex transport paths in a porous media. In general, tortuosity is not a simple *geometrical quantity*. Instead, it depends on various factors, including: the shape, size, and type of the grains, pores, and pore channels; mode of packing of the grains; grain size distribution; the orientation and non-uniformity of the grains (Dullien 1992; Salem and Chilingarian 2000).

2.3 Quantification of internal features of porous media

This section can be divided into two parts: the review on the development of acquisition techniques of the internal structure of objects and the description of the internal structure.

2.3.1 The acquisition of the internal structure of objects

For porous media made of cohesionless materials (sand for example), the particle

size distribution (PSD) and particle shapes are the simplest and most fundamental characteristics which have critical influences on the internal structure. They affect the void ratio range which the specimen could achieve (Miura et al., 1997). Actually, before the advent of modern non-invasive detection technology, particle size distribution is probably the only information we could obtain to quantify the internal feature of the specimen. Sieve analysis has been adopted and been in use for decades to measure the PSD. Depending on the materials being investigated, different methods could be used. These methods include: throw-action sieving, horizontal sieving, tapping sieving, supersonic sieving, wet sieving and air circular jet sieving (McGlinchey, 2005). Some other methods are also available such as laser and image analysis based techniques (White, 2003; Altuhafi et al., 2013). In some areas, real-time data reporting system has also been developed to continuously monitor the PSD information of a material (Kaye et al., 1996). Unfortunately, all of those methods have to destroy the specimen and in no way reflect the true structure of the specimen.

Compared to PSD, pore size distribution is more important in the study of fluid flow properties of porous media. There are various methods in the literature to accomplish this task. Those methods can be divided into invasive and non-invasive approaches.

Examples of invasive methods are:

1) Munari et al. (1985) used a combined bubble pressure solvent permeability

method to calculate the pore size distribution of various commercial and manmade membranes;

2) Permeation porometry utilizes the process of capillary condensation due to the presence of curved meniscuses. The pore size range however is relatively small (Diamond 1971), i.e., 1nm~60nm. It can be used on materials such as hydrated cement pastes or ceramics (Diamond 1971 and Seiyama 1983);

3) another methodology introduced by Brun et al. (1973) called thermoporometry makes use of the phenomenon that the melting and freezing points of a small portion of a liquid are lower than those of the bulk part. Therefore, the melting temperature of the frozen liquid imbibed into a medium during the melting process can be interpreted into pore size distribution data. This method needs sophisticated techniques to monitor the mobilization of the re-melted liquid in the specimen (Brun 1973, Mitchell 2008). Note that this method is sometimes termed as Nuclear Magnetic Resonance (NMR) Cryoporometry to highlight the use of NMR technique to monitor the mobilization of melted liquid;

4) another category of methods make use of actual experimental permeability tests and back-calculate the characteristics of the porous media. In this kind of methods, the interpretation of the experimental data highly depends on the transport models being used (Nakao 1994);

5) the last method is called mercury intrusion porosimetry which is more widely used in geotechnical engineering and oil recovery practice (Matthew et al. 1993, Katz and Thompson 1986). The pore size which could be measured using this test ranges from as high as 1mm to as low as nm level depending on the applied pressure (Diamond 1971). However, this test has its own drawbacks: firstly, Mercury intrusion test may raise the concern of toxicity (Bernhoft 2011) in routine laboratory work. Secondly, it is theoretically inappropriate being employed on cement-based materials (Diamond 2000, Chatterji 2001). Diamond (2000) proves that the air voids trapped in pastes are the main source of error leading to systematically calculated pore size distribution. The third, if the specimen is loosely packed or elastic/plastic internal structure may happen under high intrusion pressure, the interpretation of the results will be questionable (Giesche 2006).

The interpretation results of those invasive methods depend on the theory being used and sometimes are inconsistent between methods (Diamond 1971). More critically, those invasive methods are incapable of capturing the anisotropic pore structure since those methods never incorporate direction into their theory.

The simplest and oldest non-invasive method is optical microscopic observation which dates back to 16^{th} century (Kriss and Vesna 1998). Optical microscope is also referred as light microscopy which utilizes visible light and a series of magnifying lens to obtain the enlarged image of small objects. Therefore, it can provide direct visual of the

structure of the specimen. Images could be captured by photographic film or charge coupled device (CCD). The shape, size and distribution of particles and voids can be quantified directly. This technique is still being in use since it is straightforward and low-cost (Aydilek et al., 2002).

Some other microscopic technologies employing non-visible light were developed in the past century, such as: Scanning Electron Microscopy (SEM), Transmission Electron Microscopy (TEM), Field Emission Scanning Microscopy (FESEM) and Atomic Force Microscopy (AFM) (Nakao 1994). These technologies all have their own merits such as high resolution (nanometer level or even higher). They are good for viewing the shape and size of individual particles as performed by Guo and Su (2007) amongst others. However, the sample preparation methods of those technologies are usually complicated. It is really difficult to prepare a sample without damaging the initial structure of the sample since the first step always involves fractioning or sectioning the whole sample into slices (Zhao et al. 2000). More importantly, all methods using microscopic techniques can only view the surface of the specimen. If the internal structure is needed, the specimen has to be cut into slices or grinded layer by layer to obtain successive 2D images (Muhunthan et al., 2000). Again, this process may damage the internal structure of the specimen. Also, if the slice space is not uniform along the direction perpendicular to the slice surface, the constructed 3D image may be questionable.

The last non-invasive method is X-ray Computed Tomography (CT) which is commonly used in clinical practice for diagnostic or therapeutic purposes. It employs the fact that objects with different densities absorb different amount of x-rays. When a beam of X-ray passes through an object, a projection image could be captured on the opposite side of the beam source. By rotating the beam source, a series of projections reflecting the spatial variations of one cross section at different angle could be obtained. The word "Computed" highlights that the projection images will be processed by a computer to visualize the internal structure of the object. The X-ray beam of traditional CT is usually in a fan shape with a thickness between 1~10mm. After a slice being scanned (involving a complete rotation of the beam source), the object would be moved along its axial direction for next rotation. 3D images are constructed using a stack of 2D images. More advanced CT systems are capable using cone-shaped beam to simultaneously capture projection images in 3D space leading to a much faster scanning speed.

One thing to note is the reconstruction of the raw data acquired through the scans, i.e., the projection images. The projection images are of no use for direct analysis or interpretation. In fact, the projection images are the Radon transformation of the internal structure of the object (Deans 1983). The reconstruction of the raw data is actually to back calculate this transformation. One of the most widely used algorithms to implement this process is called filtered back projection technique (Herman and Gabor 2009). It is

computation effort inexpensive and easy to implement. In fact, there are a lot of algorithms in the literature but it is out of the scope of this research and no detailed literature review will be provided here.

2.3.2 Description of microstructure

To describe the microstructure of materials, some basic concepts of elements need to be defined in different number of dimensions (Kurzydlowski and Brian 1995): 1) 0D, point; 2) 1D, linear; 3) 2D, surface; 4) 3D, volume. Examples of them are impurities in polycrystals (point), fibers (linear), lamellar particles (surface) and grains/voids (volume). The basic attributes of those elements include their size, shape, numbers, distributions and directions. The size of those elements can be measured in length, area and volume for 1D, 2D and 3D elements respectively. The shape can be categorized by some mathematical expressions such as sphericity and roundness (Harr 1977; Liu and Matsuoka 2003; and Mitchell and Soga 2005). The numbers and distributions can be determined by counting or some invasive tests discussed in previous section (e.g., sieve analysis). However, the quantification of directional features is not an easy task.

The characterization of directional data was systematically investigated by Kanatani(1984). Formal least square approximation was applied and fabric tensors of different orders were defined. These fabric tensors were compared with a method of statistical test and a physical example (Kanatani 1984). Most of the later work by other

researchers employed similar form of fabric tensor.

Different measures have been used to describe the anisotropy of granular soils. It has been known that the anisotropic behaviour may be related to the distribution of the contact normals, the shape of particles, the directional distribution and shape of voids (Oda et al. 1985). Different fabric tensors can be defined using these measures, and applied in different areas of applications. For instance, the one defined by contact normal is more favorable in developing constitutive models because most mechanical responses can be related to the contact forces. On the other hand, as the hydraulic conductivity property depends more on the pore spaces in the media, the fabric tensor defined based on directional voids becomes more promising.

Inglis and Pietruszczak (2003) discussed the differences of various descriptors and they observed that the degree of anisotropy assessed by those descriptors follows a general trend: *MIL*(Mean Intercept Length) <*APS* (Areal Pore size Distribution) <*SLD* (Star Length Distribution) <*SVD* (Star Volume Distribution). Smit et al. (1998) also reported similar observations. In this study, *MIL* and *APS* will be used as the descriptor to define the fabric tensor.

2.4 Analytical model

Most prediction model of permeability of porous media are more or less based on the Kozeny-Carman model, which makes the permeability *K* a function of several geometrical

parameters (Kozeny 1927; Bear 1972):

$$K = \frac{\phi^3}{C_f \tau (1-\phi)^2 S^2} \tag{2.1}$$

where ϕ=porosity, S=specific surface of the solid volume , τ is the tortuosity and C_f is a shape factor. However, this correlation assumes the permeability in all directions are identical, which conflicts with experimental evidences (Harr 1962).

Wyllie and Gregory (1955) suggested that the exponent of porosity in KC equation is a constant which depends on the porosity and particle shape of porous media. They also attempted to calculate the constant using electrical tortuosity measurements assuming a shape factor. However, they admit that there are no theoretical consensus on the hydraulic tortuosity and electrical tortuosity.

Bourbie and Zinszner (1985) performed permeability tests on a total of 240 Fontainebleau sandstone samples. They came to a mathematical expression correlating the porosity with permeability. It is $k = 2.75\times10^{-5}\times\phi^{7.33}$ for $\phi < 8-9\%$ and $k = 0.303\phi^{3.05}$ for $\phi > 8-9\%$ where ϕ is the porosity of the sample. It can be seen that for the latter case, the expression resembles the KC equation very well and provides some information on tortuosity.

There are also some predictive models correlating the particle size of granular materials and permeability. The most famous one is by Hazen (1911). $k = C(D_{10})^2$ where C is an empirical coefficient and D_{10} is the effective particle size. Despite that the equation

is still in use for quick evaluation purpose in engineering practices, this equation contradicts with the basic fact that samples made of the same material with same D_{10} can have different porosity. The KC equation in fact has the same problem. As pointed out by Scheidegger (1974) and Hillel (1980), only the bulk volumetric parameter (e.g., porosity) is not adequate to predict the permeability since specimens with same porosity can have greatly different pore size distribution. Other models correlating permeability include Shepherd (1989), Herzer (1990) and Odong (2007).

To account for the pore size variation of porous media, Childs and Collis-George (1950) developed a model based on statistical theory. The basic philosophy is that different sequences of pairs of pores contribute differently to the overall permeability. By knowing the pore size distribution, the permeability can be calculated in a summation manner:

$$k = C\frac{\rho g}{\mu}\sum_{s=0}^{R}\sum_{\delta=0}^{R}\min(s,\delta)\cdot f(s)\Delta s\cdot f(\delta)\Delta\delta \qquad (2.2)$$

where C is a constant, ρ and μ are the density and viscosity of the fluid respectively, s and δ are the current radii of pores being considered, $f(s)\Delta s$ and $f(\delta)\Delta\delta$ are the pore space occupied by pores with radii $s \to s+\Delta s$ and $\delta \to \delta+\Delta\delta$ respectively, R is the pore size where the calculation stops. By changing R, the permeability of the medium at different moisture content could be computed. The limitation of their model lies in the fact that they ignored the influence of cells of different sizes. It may lead to overestimation of the permeability at low water content. Some other models based on statistical theory were

developed by other researchers (Marshall 1958; Millington and Quirk 1961; Juang and Holtz 1986).

Based on the concept of "critical area", Wong and Li (2011) developed a model making the permeability a function of the principal strains. The difficulties of applying this model to general conditions stem from its assumptions that the particles are regularly packed mono-sized spheres.

Scholes et al. (2007) made an attempt to obtain a more general model applicable to different types of soils. By assuming flow in different directions occurs within the same network of pores, the permeability is expressed as a function of tortuosity only. The major difference between this model and that of Wong (2011) lies in whether the flow path is a factor contributing to the permeability anisotropy. However, Scholes assumed deformable particles and non-changeable microstructure of soils, which obviously conflicts with well-established theory and experiment results.

Ahmadi et al. (2011) modified the REV model and the concept of Darcy flow to incorporate the influence of tortuosity, aiming at an analytical framework to assess the permeability of water through granular media. Distinct from Scholes's model in which the tortuosity is assumed to be constant in all directions, Ahmadi et al. took into account the directional variation of tortuosity using the tortuosity tensor (Bear and Bachmat 1991).

One key parameter in Bear and Bachmat's and Ahmadi et al.'s model is the

tortuosity tensor. However, the definition of tortuosity is not unique (Guo 2012). In literature, there are mainly four types of tortuosity.

1) The definition of geometric tortuosity is the ratio of geodesic distance and the Euclidean distance between two points (Gommes et al, 2009). It can also be expressed as the ratio of the shortest pathway to the straight-line length (Adler, 1992). Some researchers may even express it as the inverse of the above definition (Hillel, 2004).

2) In study of fluid flow problems, tortuosity is defined as the ratio of effective hydraulic path length to the length of the straight line connecting the opposite faces of the specimen (Clennel 1997). The effective hydraulic path length can be derived by averaging the flow lines in a certain period of time (Koponen et al., 1996). Feng and Yu (2007) proposed an approach to estimate the effective path length based on pore size distribution information. The definition employed by Bear (1972) is the square of the inverse of the above definition. The square originates from the process of homogenization which is used to project the micro-level potential gradient in the flow direction to macro-level gradient.

3) The electrical tortuosity is usually obtained by measuring the electrical resistance of a medium saturated by a certain fluid whose electrical resistance is known (Wyllie, 1954; Schopper, 1966; Dullien, 1979). Since the flow of ions through a porous medium, it is the most frequently used as the hydraulic tortuous (Winsauer eta al., 1952).

4) Diffusive tortuosity is defined as the ratio of diffusivity in free space to that in a porous medium (Currie, 1960; Epstein, 1989). However, the process of diffusion always involves chemical reactions making the tortuosity definition inconsistent (Sahimi, 2011).

2.5 Numerical simulation

The numerical simulation of fluid flow on a particle level can be divided into three categories: Computation Fluid Dynamics (CFD) model, Lattice Boltzmann Method (LBM) and Pipe Network Model (PNM).

Methods based on CFD are conceptually straightforward (Gruber et al., 2012; Adler et al., 1990). This type of methods usually uses the full microstructure of the specimen as the internal boundaries and Navier-Stokes equations are solved by using Finite Element Method, Finite Volume Method or Finite Difference Method. Due to the complexity of the microstructure of the media, the errors stemming from image acquiring, processing, transforming to volume (3D) or region (2D) for meshing and meshing itself will accumulate to some extent which may render the simulation results useless. On the other hand, assuming all the above errors could be minimized, this method might yield more accurate results, but even very small volume of specimen will produce large amount of meshing data, making the computational effort unaffordable, if not impossible.

Lattice Boltzmann Method: this method also utilizes Navier-Stokes equations and uses the micro-structure as the “obstacles”. Although it has been implemented by some

researchers on particle level, it is more suited for large scale turbulent flow but not applicable to compressible flows.

Assuming the soil to be a spatially periodic porous medium, Meegoda et al. (1989) used Finite Element Method to simulate the flow through soil at the microscopic level. Navier-Stokes equation was employed as the governing equation. A series of variables at the macroscopic, including the average specific surface area, average void ratio, anisotropy, tortuosity and the arrangement of particles, were assessed and an expression for the permeability based on the above variables was proposed.

In recent years, Pipe Network Model has become successful in simulating fluid flow in porous media (Blunt 2001; Chatzis and Dullien 1997; Diaz et al. 1987; Kralj and Pande 1994). It assumes the porous media is an interconnected network of pipes. The sizes of the pores are used as the sizes of the pipes. Washburn's equation (1921) is used to compute the fluid flow through one single pipe. Simultaneous equations of all the pipes are solved iteratively. This method is simple, computation effort inexpensive, yet accurate.

Chapter 3 Experimental study of permeability anisotropy

This chapter investigates the permeability anisotropy of granular materials. The focus is placed on the design of a new permeameter and the experimental studies utilizing this device to obtain the anisotropic permeability of cohesionless materials. The induced hydraulic variation of materials under loading process is also examined following adapted tri-axial test procedures.

3.1 Materials used in this study

Three granular materials (Ottawa sand C109, crushed limestone and Eston Lentils) and two fluids (de-aired water and mineral oil) are used in this study.

Ottawa sand C109 (Sand O) is a uniformly graded sand with particles rounded or sub-rounded. It is a standard sand that has been widely used in the past. Sand L is derived from crushed limestone. The particles of this material are more angular and elongated compared to Sand O (Guo and Su, 2007). The material is washed to make sure that no fines adhere to the particles.

Following ASTM D422-63 (ASTM 2007) and ASTM D854-10 (ASTM 2010), the particle size distribution curves and specific gravity of both materials were obtained (Fig. 3.1) and summarized in Table 3.1.

Table 3.1 Physical properties of Sand O and Sand L

Material	D_{10}(mm)	D_{50}(mm)	C_u	G_s
Sand O	0.220	0.376	1.80	2.65
Sand L	0.197	0.364	2.00	2.77

Note: D_{10}, effective particle size; D_{50}, average particle size; C_u, coefficient of uniformity; G_s, specific gravity

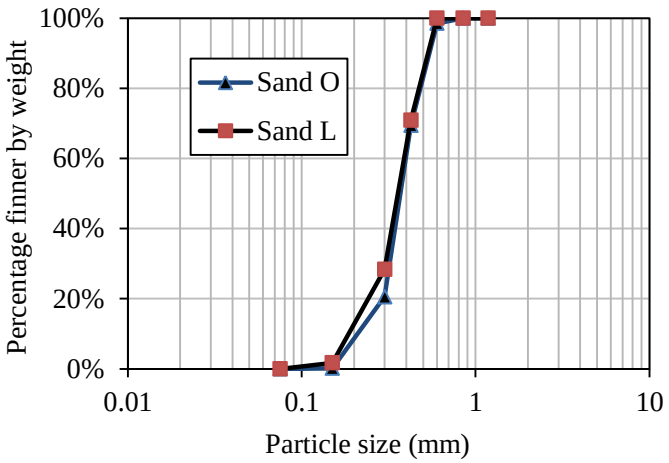

Fig. 3.1 Particle size distribution of Sand O and Sand L

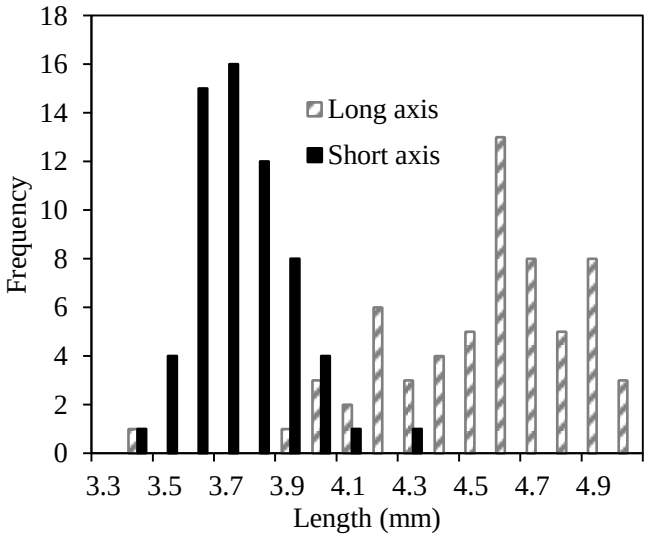

Fig. 3.2 Particle size distribution of Lentils

The third granular material is Eston Lentils, with the grains being flat and rounded (oblate spheroids). The length of the long axis of the beans is 4.49±0.31 mm and the short

axis is 2.19±0.17 mm. The specific gravity of the lentil was determined as 1.37. The length distribution of long axis and short axis are presented in Fig. 3.2.

Owing to its large grain sizes, the lentil packing has very high hydraulic conductivity when using water as the fluid. In order to obtain laminar flow in such packing, high viscosity mineral oil was employed in the permeability tests. The Mineral Oil (Heavy) used in this study is a nontoxic, odorless, transparent fluid manufactured by PENRECO (A division of Pennzoil Products Cie). The specific gravity and the dynamic viscosity of the mineral oil are 0.865 and 98 mPa•s at 20℃, respectively. When performing tests using lentils and mineral oil, the mineral oil from the outlet is collected and pumped back to the source tank to reduce the cost. It raises the question that the dynamic viscosity may change after circulation. Therefore, the dynamic viscosity of the reused and new oil was measured at different temperatures as shown in Fig. 3.3. Difference less than 1.19% is identified when the temperature is in the range of 21 ~ 23℃ (most of the tests are performed under this temperature range). The measured hydraulic conductivity was corrected to the temperature of 20℃ based on the viscosity changes.

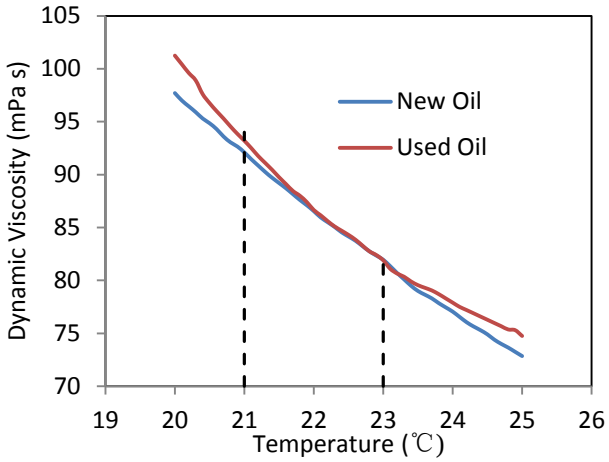

Fig. 3.3 The viscosity of the mineral oil at different temperature

3.2 Standard permeability test using regular permeameter

Constant head permeability tests were performed using a regular permeameter on Sand O and Sand L, following ASTM D2434-68 (ASTM 2006). The permeameter used is 101mm in diameter and 118mm in height. Specimens were made as described in ASTM D2434-68 and the mould was tamped gently to obtain required density. Care was taken to ensure the repeatability of the specimens for each material. The difference of void ratio was controlled in less than 0.02. For each material, three specimens were prepared and tested. Table 3.2 summarizes the void ratio *e* of testing specimens, the hydraulic gradient *i* and the hydraulic conductivity *K* for both materials.

Table 3.2 Testing parameter and results

Material	*e*	*i*	*k* (mm/s)
Sand O	0.555 ± 0.010	1.29	0.39 ± 0.005
Sand L	0.675 ± 0.010	1.20	0.30 ± 0.005

Note: *e*, void ratio; *i*, hydraulic gradient; *k*, hydraulic conductivity.

3.3 Anisotropic permeability test

3.3.1 Modified permeameter and sample preparation method

The permeameter recommended by ASTM (2006) is generally composed of a cylinder mold and a lid. When preparing the sample, the sand is deposited vertically into the mold, thus the bedding plane can only be horizontal. As a result, the flow of fluid is always perpendicular to the bedding plane. In order to obtain the variation of hydraulic conductivity when flow takes place in different directions relative to the bedding plane, the permeability tests were carried out by using a prism mould with an inner dimension of 100mm ×100mm ×400mm.

As shown in Fig. 3.4, the permeameter consists of three fixed plates (AB, BC and CD) and two removable plates (A'D' and A''B'). Plate AB is not a solid plate but a hollow square plate, as shown in the figure. Fittings are installed on A''B', CD and A'D' to be connected to outlet, inlet and piezometers respectively. Fig. 3.5 shows the photos of the permeameter before and after assembling.

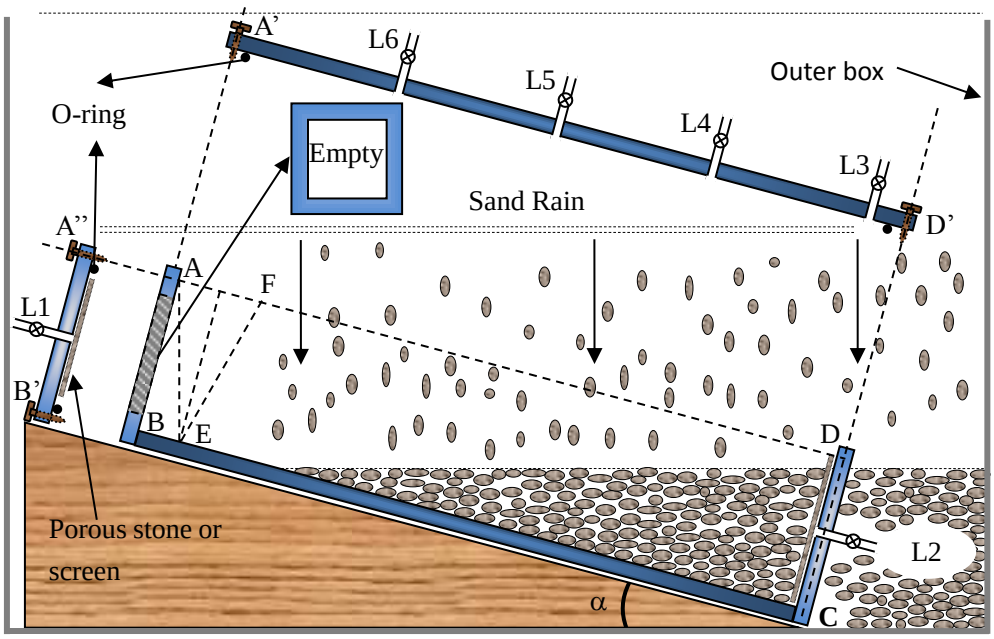

Fig. 3.4 Schematic diagram of the modified permeameter

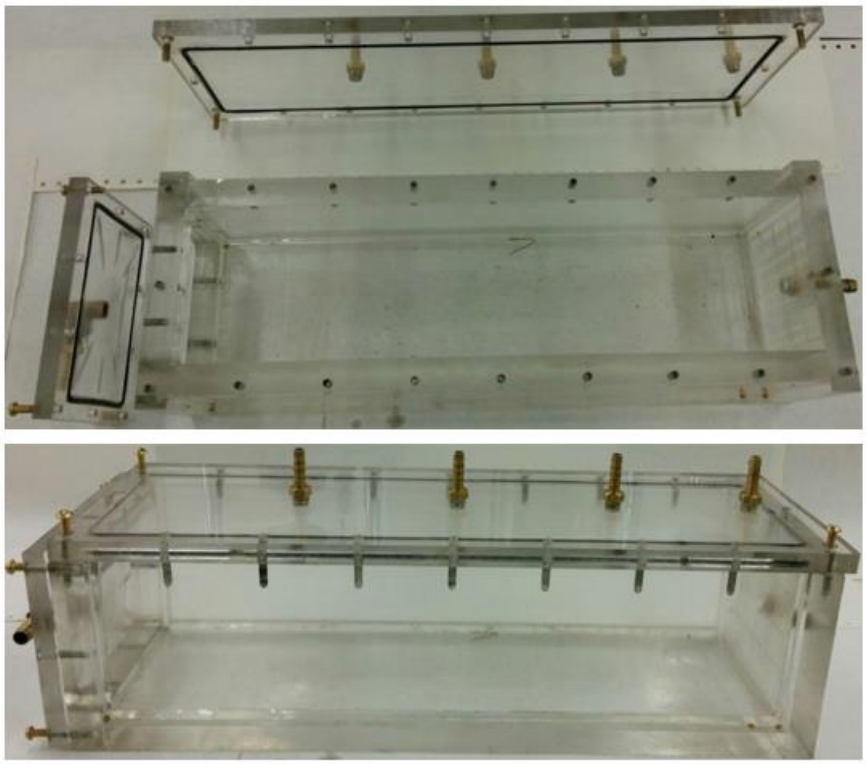

Fig. 3.5 Photos of the modified permeameter before and after assembling

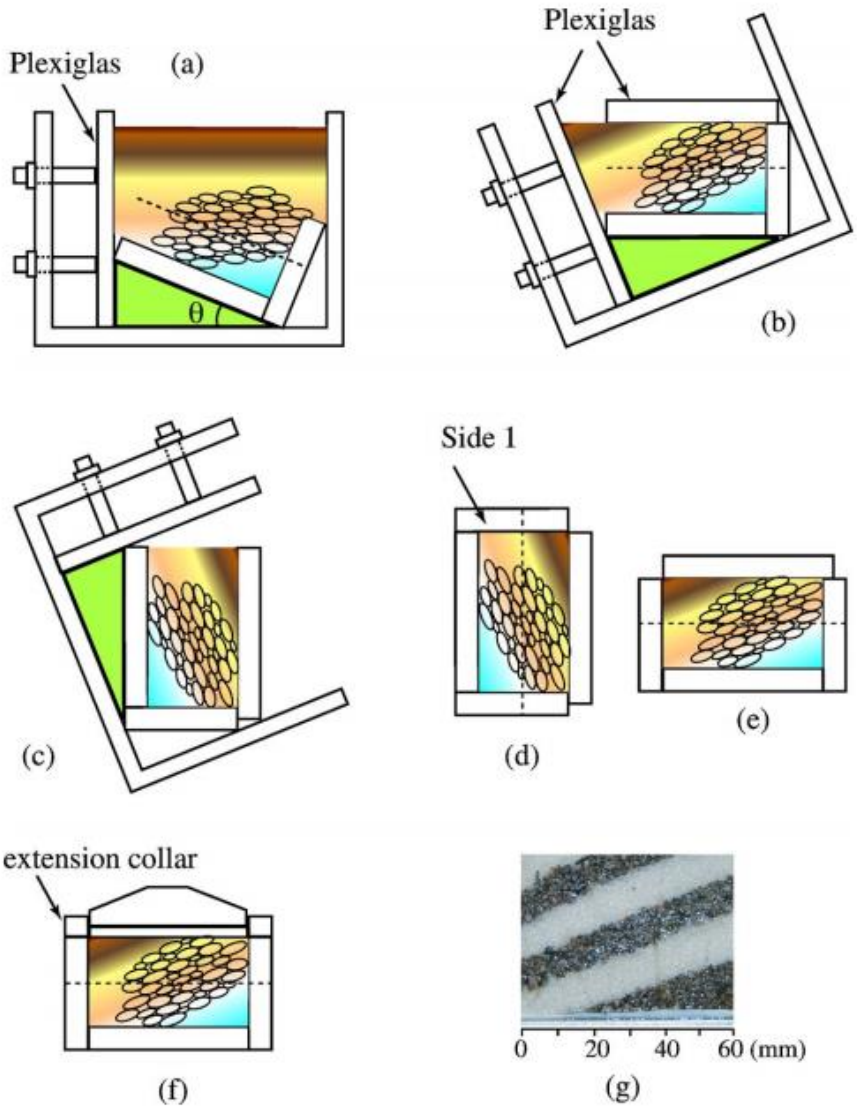

Fig. 3.6 Procedures of preparing a specimen with inclined bedding plane (Guo 2008)

The testing specimen is prepared following the procedure proposed by Guo (2008). When preparing a sample, A'D' and A''B' are first removed and the rest of the mold is placed on a wood stand which holds the mold at an angle α relative to the horizontal direction as shown in Fig. 3.4. The whole setup is then put into a bigger box. Sand rain method is employed to deposit particles into the mold. The "rain" has to start from the

lower end and move gradually to the higher end of the inclined mould to keep the material's surface horizontal. Once the outer box is filled up to the highest point of the mold, a thin metal sheet is placed on AD temporally and the outer box is turned conuterclockwise by an angle α so that AD is horizontal. The metal sheet is next removed and the surface of the sample is trimmed level. After cleaning the edges of the mold, plate A'D' is mounted. Care must be taken to prevent any particles to be trapped between A'D' and AD. At last, the mold is turned by 90 degrees and the plate A''B' is mounted. The bedding plane of the specimen makes an angle α with the vertical direction, as shown in Fig. 3.7. Fig. 3.6 shows the detailed procedures preparing a specimen with an inclined bedding plane proposed by Guo (2008).

During the process of deposition, the "rain" in the area ABE is disturbed by the hollow square plate AB. Therefore, it raises the concern that the alignment of the particles in the influenced area ABEF may not be the same as the other part of the specimen. However, the remaining part of the specimen is deemed as uniform enough to produce homogenous particle arrangement. To minimize the influence of potential non-uniformity in ABEF, only the flow between L3 and L4 is used to interpret the results. This will be verified in the following sections.

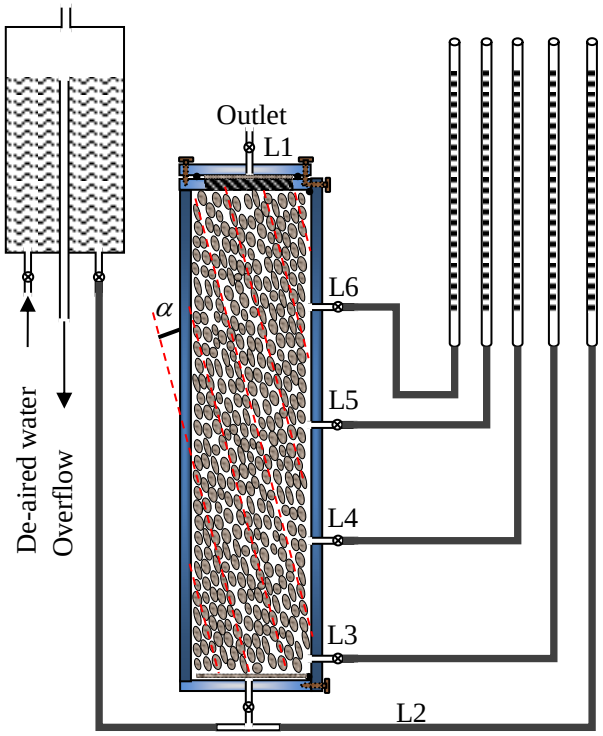

Fig. 3.7 The schematic diagram of the connection between the permeameter, fluid source and the measuring tubes

Once the specimen is prepared, the prism permeameter is connected to the water supply and graduated tubes to measure water pressure as shown in Fig. 3.7. Five graduated tubes are used to measure the hydraulic head at different locations.

It has been known that the degree of saturation has a significant influence on the permeability of porous media (Wyckoff and Botset 1936; Bear 1972). In order to obtain consistent results, the sample must be fully saturated. This is achieved by applying a negative pressure to introduce de-aired water into initially dry specimen (ASTM 2006). However, it is pointed out by Chapuis (2012) that water-tight seals may not necessarily

mean air-tight. Under vacuum, air may enter the specimen during the process of saturation if the permeameter is not air-tight. Chapuis et al. (1989) suggested a method to check airtightness of a permeameter: before introducing de-aired water into the specimen, apply vacuum and then close all valves. Then disconnect the vacuum and let the permeameter stand for a few minutes. At last, open slightly the inlet valve and, if the permeameter is airtight, there will be a noise of air flowing through the valve. In this study, a more rigorous method is proposed: before allowing the water to enter the specimen, apply vacuum through one of the fittings and connect another fitting with a negative pressure meter. All other fittings should be blocked at this stage. Let the permeameter stand for a while to allow the interior pressure stabilize and so for the negative pressure meter. Disconnect the applied vacuum and watch for any changes in the reading of the negative pressure meter. If negative pressure drops very quickly, it means that severe leakage of air presents. If the negative pressure meter can maintain at the same value or decrease a very small amount (less than 5%) within not less than 20 minutes (the typical time to saturate the sample), the permeameter is deemed as airtight.

3.3.2 Test results and discussions

Samples with different inclination angles of the bedding plane were made using Ottawa Sand and Lentils. The void ratios of Ottawa Sand and Lentils are controlled at 0.539 ± 0.018 and 0.532 ± 0.001, respectively. Constant head permeability tests were

performed using the modified permeameter. The hydraulic conductivity is determined by applying Darcy's Law:

$$k = \frac{QL}{At\Delta h} \tag{3.1}$$

where Q is the quantity of water discharged, L the distance between two adjacent fittings (L3~L6), A the cross section area of the specimen normal to the flow direction, t the running time, Δh the head difference between two fittings.

Fig. 3.8 presents the directional variation of measured hydraulic conductivity for the two materials. It should be noted that α=0 ° and 90 ° correspond to flow parallel and perpendicular to the bedding plane, respectively. The tests are repeated under the same condition for three times and the average values are used. It is observed that the hydraulic conductivity for flow parallel to the bedding plane is higher than that when the flow direction is normal to the bedding plane.

Following the work by Pietruszczak and Pande (2012), the coefficient of permeability can be expressed as:

$$k = k_0[1+\Omega_{ij}n_in_j + a_1(\Omega_{ij}n_in_j)^2 + a_2(\Omega_{ij}n_in_j)^3 + a_3(\Omega_{ij}n_in_j)^4 + ...] \tag{3.2}$$

where Ω_{ij} is a traceless symmetric second order tensor and n_i is the flow direction which makes an angle α with the bedding plane.

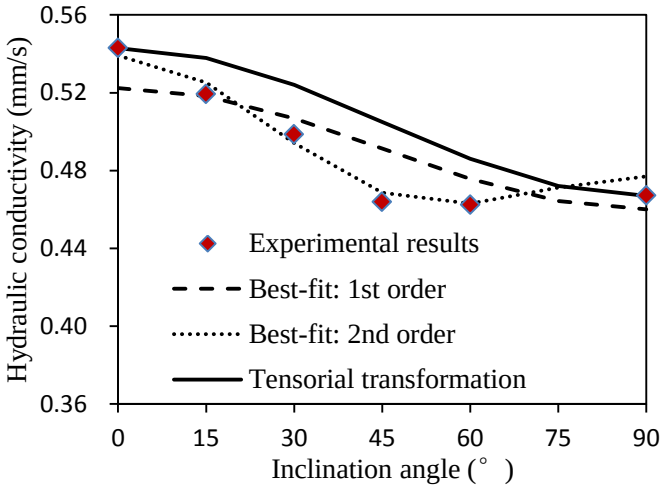

(a) Sand O (e=0.54)

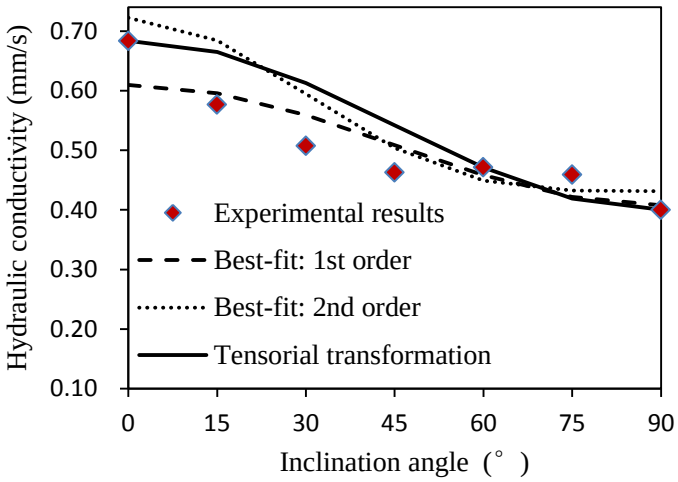

(b) Lentils (e=0.53)

Fig. 3.8 The hydraulic conductivity variation with inclination angle

Because the first and second principal material axes are in the bedding plane, the flow direction in the system of principal material axes is:

$$\vec{n} = (0, \cos\alpha, \sin\alpha)^{\mathrm{T}} \tag{3.3}$$

Considering the symmetry in bedding plane, we have

$$\Omega_1 = \Omega_2 \qquad \Omega_1 + \Omega_2 + \Omega_3 = 0 \tag{3.4}$$

Therefore,

$$\Omega_{ij} n_i n_j = \Omega_2 (3\cos^2 \alpha - 2) \tag{3.5}$$

Substituting Eq.(3.5) into Eq.(3.2) and best-fit approximations for measured hydraulic conductivity are computed including terms of the dyadic products up to order 2. The test data and best fitting curves are presented in Fig. 3.8.

For Ottawa sand, the first order approximation of the hydraulic conductivity with angle α can be expressed as $K(\alpha) = 0.062\cos^2\alpha + 0.460$ (mm/s), and for the Eston lentils, the first order best-fit curve is $K(\alpha) = 0.202\cos^2\alpha + 0.408$ (mm/s).

By assuming the hydraulic conductivity can be represented by a second order tensor, the hydraulic conductivity tensor is constructed employing the principal values, i.e., the values in the bedding plane and that in the direction perpendicular to the bedding plane. The hydraulic conductivity in different directions can be obtained by transformation of the tensor as follows:

$$K(\alpha) = K_{ij} n_i n_j = (\cos\alpha, \sin\alpha) \begin{bmatrix} K_h & 0 \\ 0 & K_v \end{bmatrix} \begin{pmatrix} \cos\alpha \\ \sin\alpha \end{pmatrix} \tag{3.6}$$

where K_{ij} is the hydraulic conductivity tensor constructed by values in the principal directions and n_i is a unit vector in the flow direction within the material coordinate system.

The hydraulic conductivity tensor of both materials are constructed in this manner and the hydraulic conductivity in different direction is estimated using Eq.(3.6). Fig. 3.8

also presents the hydraulic conductivity estimated from tensorial transformation. It shows that there is no significant difference between the two representations in Eqs. (3.2) and (3.6). Therefore the directional hydraulic conductivity can be represented by either scalar function or a second order tensor.

The measured permeability anisotropy ratios are summarized in Table 3.3. For comparison purposes, the test result for uniform lenticular lead particles reported by Witt and Brauns (1983) is also included. In all cases, higher hydraulic conductivity is obtained for flow parallel to the larger dimension of particles, whether the particles are elongated (prolate) or flattened/lenticular (oblate). The permeability anisotropy ratio of the dense packed uniform lenticular Eston lentils with flattened particles is in the range of 1.25 to 1.78, which is slightly higher than that of Ottawa Sand C109 that has sub-rounded (slightly elongated) particles. The permeability ratios of these two materials are lower than that of uniform flat lead lenses that have a larger aspect ratio of 4.2 in Witt and Brauns (1983).

Table 3.3 Testing materials and measured permeability-anisotropy ratio

Material	Particle shape	Aspect ratio	Porosity	k_{max}/k_{min}
Sand O	Sub-rounded, elongated	1.45	0.350	1.13-1.19
Lentils	Uniform, lenticular	2.05	0.347	1.25-1.78
Lead lenses (Witt and Brauns, 1983)	Uniform, lenticular	4.2	0.41	2.3

It should be noted that the permeability anisotropy of the different materials summarized in Table 3.3 reflects the inherent anisotropy of these materials. In the

following section, shear induced permeability anisotropy will be investigated.

3.3.3 Coaxiality between direction of flow and pressure gradient

To observe the flow lines within the sample, some methylene blue was attached on the walls of the mold. The reason for choosing methylene blue is that when it dissolves in water, it can release color continuously for a long time. Even very small amount of material can release a large amount of color. In this way, the trajectory of the color will resemble the flow lines, as shown in Fig. 3.9.

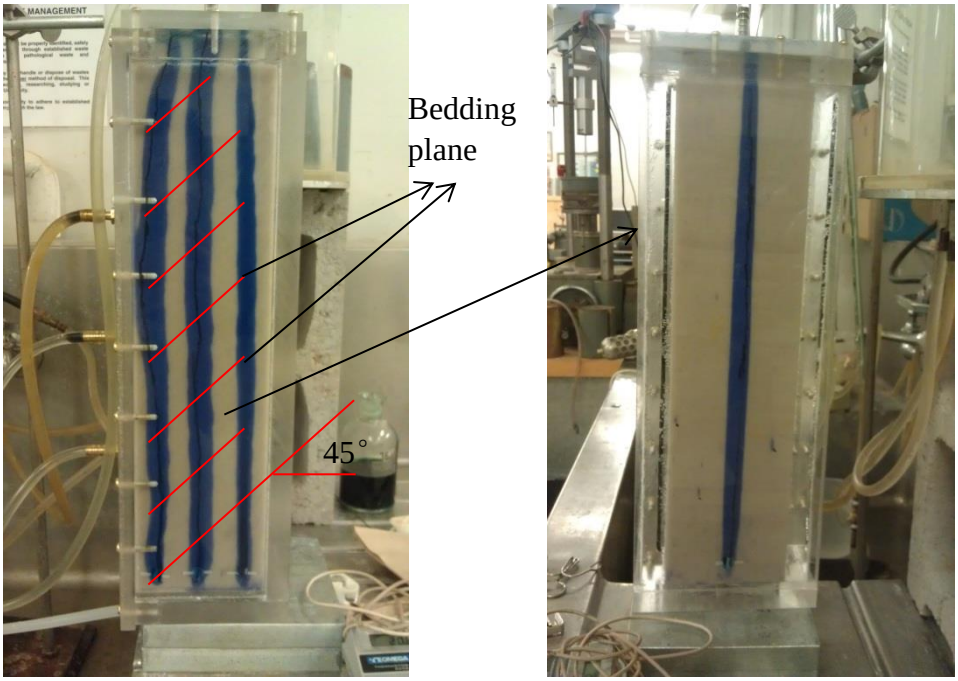

Fig. 3.9 The "flow lines" within the sample

Fig. 3.9 shows the flow lines in a test on Sand O with the bedding plane angle α=45°. For this case, the hydraulic gradient is in vertical direction while the bedding plane is

inclined at an angle 45°. Even though the hydraulic gradient makes an angle with the bedding plane, the flow lines are still along the direction of hydraulic gradient, at least on an average sense.

As discussed previously, the hydraulic conductivity can be represented in two ways, i.e., a scalar-valued function of direction or a second order tensor. Since the flow lines are almost coaxial with the hydraulic gradient for weak anisotropic material, the scalar-valued function is sufficient to describe the fluid flow, i.e., $v_i = K(\alpha)i_i$. When the anisotropy is strong, the generalized Darcy's law, $v_i = K_{ij}i_j$, may be required to describe the deviation of the fluid flow from the direction of hydraulic gradient.

3.4 Induced anisotropic permeability test

3.4.1 Test setup

The triaxial testing device is widely used to investigate the behavior of soils subjected to axisymmetric stress conditions. In this study, the triaxial apparatus is used to investigate the variation of permeability owing to fabric change (and volume change) induced by applied deviatoric stresses.

To investigate shear induced permeability anisotropy, drained triaxial compression tests on saturated Ottawa Sand C109 were performed. Falling head method was employed to measure the hydraulic conductivity when the sample is under a certain level of strain.

Cylindrical specimens (35 mm in diameter and 70mm in height) with the void ratio in the range of 0.48 to 0.64 were used in the tests.

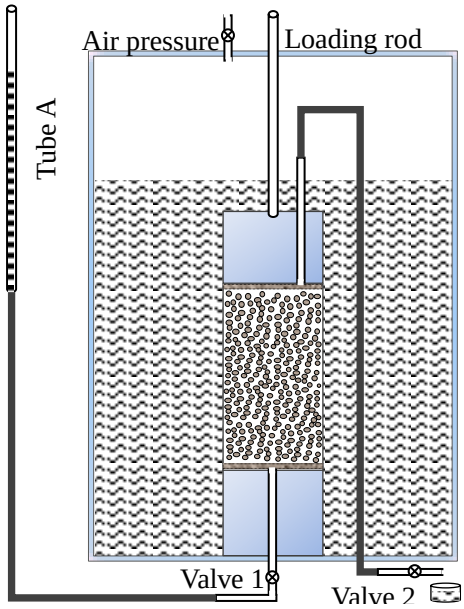

Fig. 3.10 Schematic diagram of the permeability testing setup

In the testing setup illustrated in Fig. 3.10, Tube A is used to measure the volume change during shear. It is also used as the water source for falling head permeability test. The system is calibrated in advance to correlate the water level change in Tube A to the volume change. During shear, Valve 2 is closed and Valve 1 is open to monitor the volume change of the specimen. At selected deviatoric stress levels, the axial compression is stopped and the axial deformation is maintained. The permeability test is carried out by opening both valves 1 and 2.

3.4.2 Test results

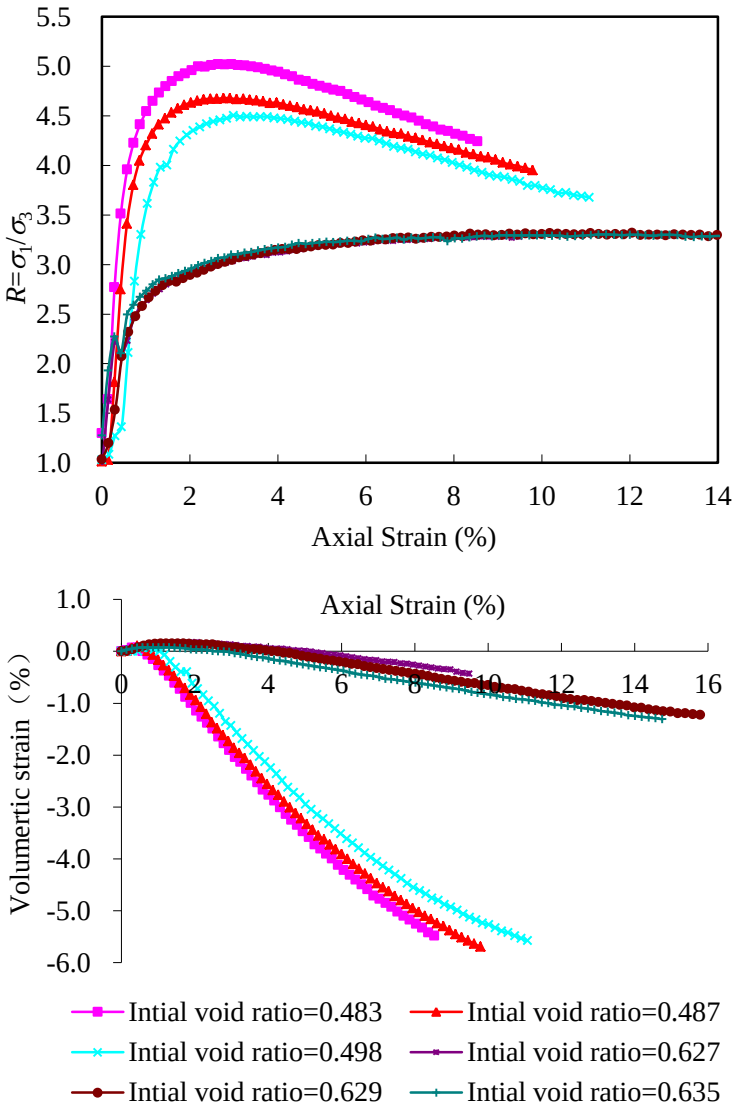

Fig. 3.11 Mechanical responses of soil samples with different void ratios

In order to investigate the relation between the hydraulic conductivity and fabric, six specimens with different initial void ratios e_0 were tested using a conventional triaxial apparatus and the permeability was measured using the falling head method at different

stages of shearing. In the triaxial compression tests, the confining pressure is kept as constant of σ_3 =100kPa for relatively dense samples with e_0=0.483~0.498, 50kPa for relatively loose samples with e_0=0.627~0.629, and 35kPa for the loosest one with e_0=0.635. Fig. 3.11 presents the evolution of the stress ratio $R= \sigma_1/ \sigma_3$ and the volumetric strains against the axial strains of the soil samples. As can be seen from the figure, with the increase of the initial void ratio, the specimen tends to have more dilation during shearing.

It has been known that the hydraulic conductivity increases as the void ratio of the soil increases. It is attributed to the increase of possible void path for the water molecule to go through. In general, the hydraulic conductivity of a soil can be related to its void ratio using the Kozeny-Carman equation (Taylor, 1948):

$$K = \frac{Ce^3}{1+e} \tag{3.7}$$

where C depends on soil structure and particle sizes. However, the Kozeny-Carman equation does not reflect the influence the fabric change explicitly.

The measurement of hydraulic conductivity of Ottawa Sand C109 at different deviator stress level during triaxial compression show that the hydraulic conductivity is not a unique function of void ratio as described by the Kozeny-Carman equation. Fig. 3.12 presents the hydraulic conductivity (K) at different stages in triaxial compression tests under drained condition. Prior to shearing, the hydraulic conductivity of the loose sand and dense sand (with e_0 = 0.63 and 0.49 respectively) are 0.25 mm/sec and 0.05 mm/sec on the

average. During the shearing stage, K continuously decreases as q/p is increased, even when dilation occurs with increasing void ratio. Herein $q=\sigma_1-\sigma_3$ and $p=(\sigma_1+2\sigma_3)/3$. It is likely that the decrease of K during the dilation stage is related to the rearrangement of particles, or fabric change. In other words, the flow path for water may be affected more by the fabric change than the increase of the void ratio.

It should be noted that there is an exception, the sample with the initial void ratio of 0.627, in Fig. 3.12. In this test, some sand grains were found in the drainage line after the test. These particles blocked the path of water flow in the tube and reduced the measured permeability.

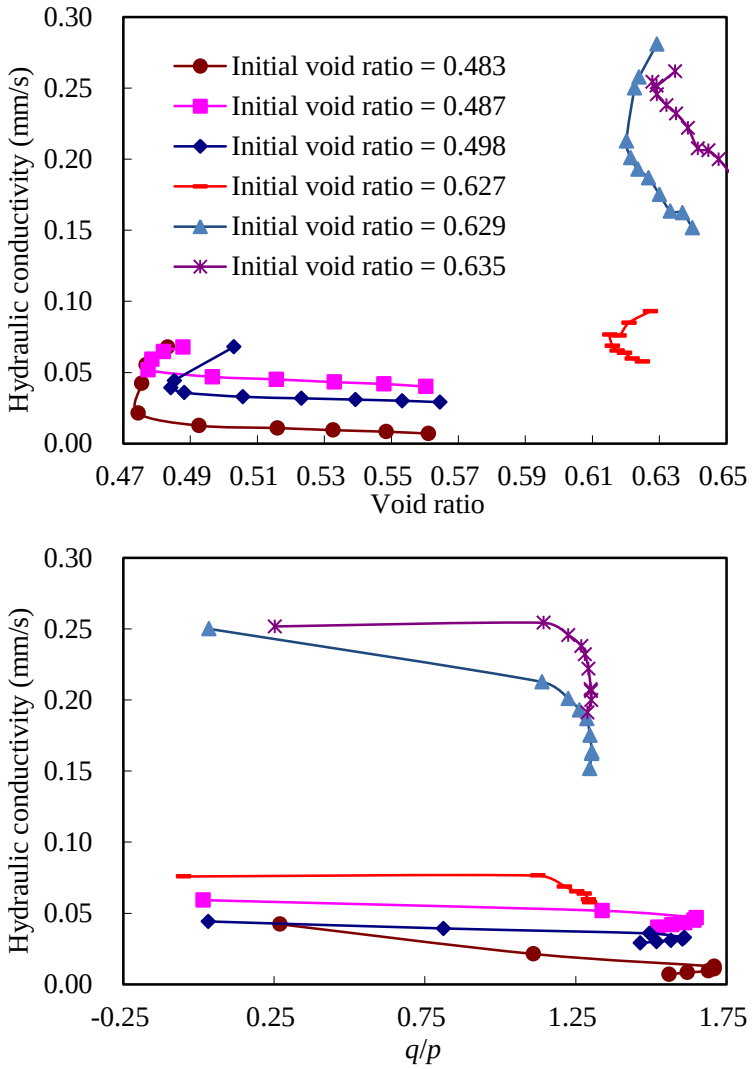

Fig. 3.12 The permeability measured at different deviator stress level in triaxial compression

3.5 Summary

In this chapter, laboratory permeability tests are performed on selected granular media and fluid (Sand O, Sand L, Eaton Lentils). The main work is summarized as follows:

1) Permeability tests are performed using ASTM suggested standard method, in

which the permeability anisotropy and the influence of the pore structure on permeability are not addressed;

2) A modified permeameter is devised to prepare samples with different inclination angle with respect to flow direction. This device makes it possible to measure the anisotropic hydraulic conductivity for flow in different direction within cohesionless materials with inherent anisotropy;

3) The test results of Ottawa Sand and Lentiles show that both materials display a certain degree of permeability anisotropy. While the anisotropic permeability can be characterized by a second order tensor, it can also be described as a function of direction for weak anisotropic materials;

4) Induced permeability anisotropy tests are performed utilizing a regular tri-axial compression device with some modifications. The test results show that the hydraulic conductivity along the axial direction of the sample decreases even though the overall void ratio is increasing with the increase of shear strain. It implies that not only the void ratio, but also the particle arrangement has some influence on the permeability of sand.

Chapter 4 Quantification of microstructure of granular materials

This chapter presents a methodology to reconstruct the microstructure of granular materials using micro-CT scan. Different descriptors are examined for proper quantification of the microstructure.

4.1 Introduction

Different measures have been used to describe the anisotropy of granular soils. It has been known that the anisotropic behaviour may be related to the distribution of the contact normals, the shape of particles, the directional distribution and shape of voids (Oda et al. 1985). Different fabric tensors can be defined using these measures, and applied in different areas of applications. For instance, the fabric tensor defined by contact normal is more favorable in developing constitutive models because the average stress in soil can be related to inter-particle forces at contacts (Wan and Guo, 2001). On the other hand, as the hydraulic conductivity property depends more on the pore structures in the media, the fabric tensor defined based on directional voids becomes more promising (Guo 2012).

The characterization of directional data is systematically investigated by Kanatani (1984). Formal least square approximation is applied and fabric tensors of different orders are defined. Most of the later works by other researchers employ similar form of fabric

tensor (Kanatani 1984).

Obviously, the key to characterize the microstructure of granular material is to obtain the arrangement of particles and the distribution of pore void in the material. In this study, micro-CT will be utilized to obtain the internal structure of granular materials.

4.2 Micro-CT scan

As a non-destructive internal structure measuring technique, X-ray Computed Tomography (CT) becomes more and more popular in the field of geotechnical engineering (Phillips 1997, Alshibli 2000). The X-ray image is a projection map of the linear attenuation of the X-ray after penetrating an object. The denser materials tend to absorb more X-ray than low-density ones. Therefore, on an X-ray image, the darkness of the pixels increases with the density of the material. By taking multiple scans, a bitmap of the density of the object can be reconstructed. More comprehensive description for the working principle about X-ray CT can be found in Goldman (2007) and Hsieh (2009). Higher resolution CT scanner appeared in early 1980s (Elliott and Dover 1982, Feldkamp et al. 1989) and then rapidly applied to other research areas from the clinics.

In this research, the X-ray images are obtained using an In-vitro 1172 Micro-CT scanner designed by SkyScan (Kontich, Belgium) and owned by the Department of Material Science and Engineering, McMaster University, Canada. SkyScan 1172 has a maximum resolution of 0.7μm for small samples. The voltage can range from 20kV to

100kV and the current can be adjusted between 0-250μA. The maximum power can reach 10W. The scanner uses the cone beam reconstruction technology and the target sample can be rotated continuously to get multiple projection images. The number of projection images depends on the increment of rotation angle. The more images obtained, the more accurate the reconstruction results will be. 3D image data set can be reconstructed from the projection images using the software "NRecon" provided by SkyScan. The detailed specifications of the In-Vitro 1172 scanner and working principle can be found at http://www.skyscan.be/products/1172.htm.

4.2.1 Sample preparation

Due to the limitation on the size of the sample by the micro-CT scanner, specimens used in the permeability tests cannot be placed in the scanner. Smaller samples have to be made. Two methods are used to prepare specimens for the CT scans.

4.2.1.1 Small cubic mould

A cubic mould was made using plexiglass having five fixed plates and a removable one as the lid. The dimension of the mould is 19.2mm×19.0mm×18.7mm. After the oven-dried sand is deposited into the mould by sand rain method the same method used to prepare specimens for permeability tests, the surface is trimmed and the removable lid is placed back. The sample is then sealed with tape carefully without disturbing the

specimen. The mould is weighed before and after filling sand so that the void ratio can be determined. The falling height is controlled to ensure the void ratio matches the ones used in permeability tests.

Owing to the size effect and boundary constraints of the small mould used in this method, it was identified that the small specimen does not have the same pore structure as the large size specimens used in the permeability tests. This will be further discussed in later sections. To obtain the anisotropic microstructure of the porous media, a more appropriate sample preparation method needs to be developed to produce the same microstructure as that of large size specimens.

4.2.1.2 Epoxy resin impregnation method

This method consists of three steps: 1) to prepare a specimen of the size ϕ50.8mm×H132.1mm; 2) impregnation of epoxy resin in the specimen and 3) cut the hardened specimen to small size for X-ray CT scan. Fig. 4.1 illustrates the apparatus used for Epoxy resin impregnation. The resin impregnation chamber is made of plexiglass with a removable lid that can be sealed well under vacuum.

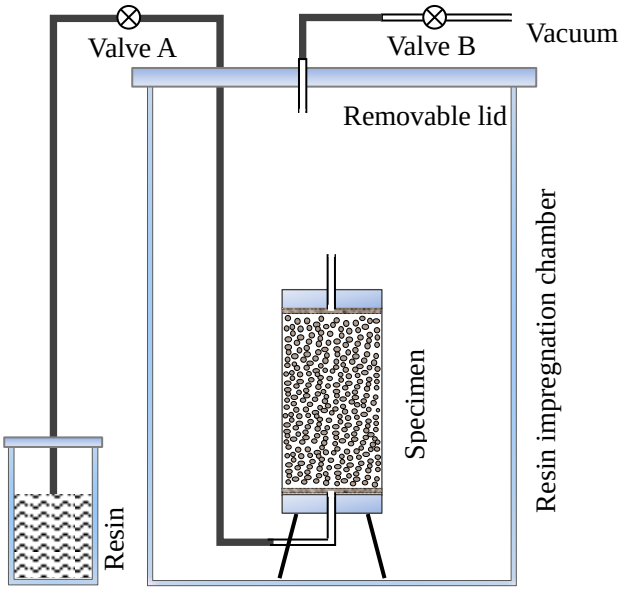

Fig. 4.1 Schematic of the resin impregnation apparatus

The specimen is first made using sand rain method, the same as that used to prepare specimens for permeability tests. The falling height is controlled to match the void ratio of the specimen used in permeability tests.

After the specimen is made, the plastic tubes are connected to the bottom of the sample. They are then placed in the impregnation chamber carefully. The lid is put back on the top of the chamber and all tubes are connected. With Valve A closed, Valve B is opened and the vacuum is applied to the chamber. Since the top of the specimen is open, the vacuum is applied to the inside of the sample. The negative pressure is adjusted carefully by a regulator attached to the vacuum pump. The negative pressure is maintained at -12.3kPa. This pressure is determined via a series of trial tests with the following constraints being satisfied: 1) the negative pressure must be high enough to

maintain a flow rate to finish the impregnation process as soon as possible, as the viscosity of the resin will increase with time lapsing; 2) the negative pressure cannot be too high to disturb the microstructure of the sample: if the pressure gradient is too high, the upward flow of the resin may disturb or even destroy the specimen (sand boiling).

The resin and hardener used in this study are manufactured by Buehler Ltd., Lake Bluff, Illinois. The volume ratio of resin to hardener used is 100:40 for the mixture, as recommended by the manufacturer. Using this ratio, however, the mixture will generate a high amount of heat in a very short period of time and solidifies too fast. Therefore, following Masad and Muhunthan (2000), acetone was used to decrease the viscosity and prolong the process of solidification. Through a series of trial tests, it was found that 1ml of acetone in every 100ml of resin and 40ml hardener can effectively reduce the solidifying time and the viscosity.

The impregnation procedures are summarized as follows:

1) Make a specimen using sand rain method in a model which is 50.8mm in diameter and 132.1mm in height;

2) Place the specimen and the mould in the impregnation chamber and connect all tubes as shown in Fig. 4.1;

3) Keep Valve A closed, open Valve B to apply the desired negative pressure to the chamber;

4) Mix the resin, hardener and acetone using previously determined mixing ratio;

5) Slowly open Valve A and observe the flow, close Valve A and B when the resin reaches the top of the specimen;

6) Let the specimen stand for 24 hours and observe if it is hard enough, leave it longer if not;

7) Cut the hardened specimen using diamond saw into a cuboid that has a cross section of 20mm×20mm.

4.2.2 X-ray CT scan images

In this study, the resolution of X-ray CT scanner is set at 26.3×26.3×26.3μm/voxel. The voltage, current and power of the generator are adjusted to 100kV, 40μA and 10W, respectively. The incremental rotation step is set to 0.5 degree to get more projection images. NRecon (SkyScan) was utilized to reconstruct the 3D images from those projection images. The so-called 3D image is merely a stack of 2D slices with each slice representing a cross-section of the specimen. The built-in function of "Ring artifacts reduction" and "beam hardening correction" were used to reduce the reconstruction error. These two correction operations are both performed in a try-and-error fashion until the reconstructed slice image is clear enough to define the regions of particles and voids.

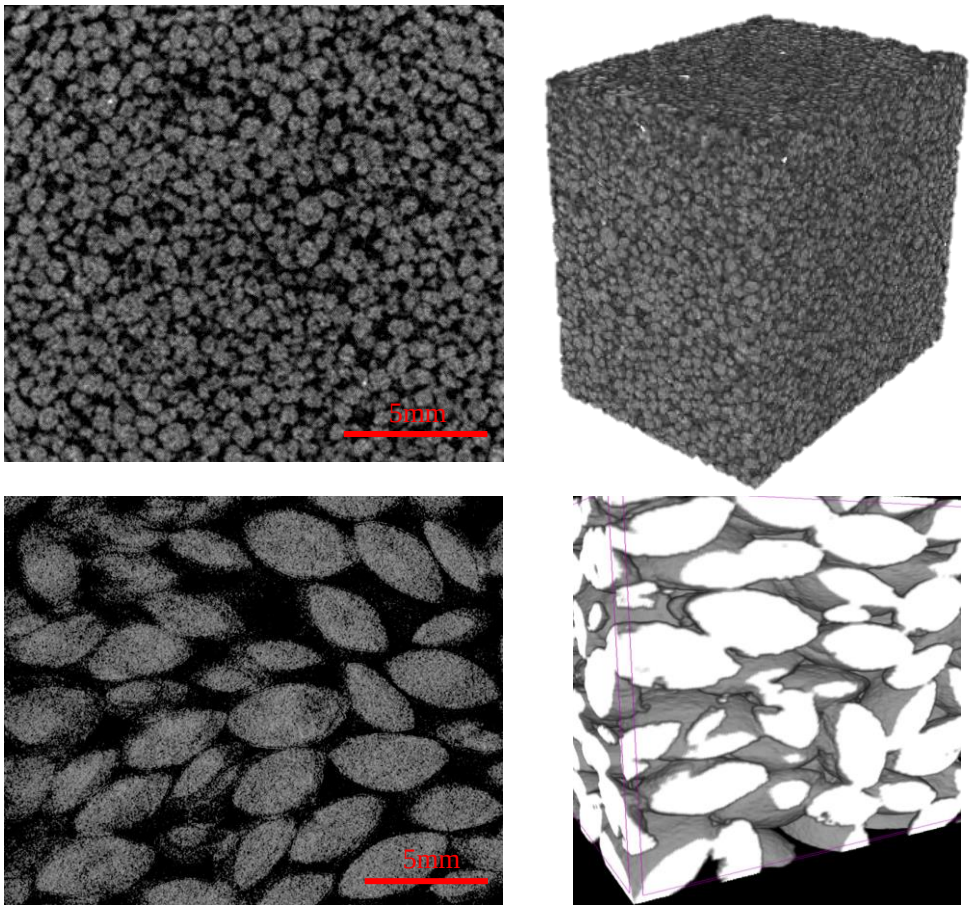

Fig. 4.2 Typical 2D slices and rendered 3D volume images obtained from Sand O (top half) and Lentils (bottom half)

Fig. 4.2 shows typical slices obtained from specimens made of Ottawa sand and Lentils and the rendered 3D volume images. They will be used to illustrate the process of image analysis. A Matlab script was developed to implement this analysis automatically.

4.3 Algorithm to identify fabric tensor

Inglis and Pietruszczak (2003) discussed the differences of various descriptors that can be used to characterize the internal structure of granular materials. These descriptors

include: *MIL*(Mean Intercept Length), *APS* (Areal Pore size Distribution), *SLD* (Star Length Distribution) and *SVD* (Star Volume Distribution). In this study, *MIL* and *APS* are used as the descriptors to define fabric tensor. The scan line method proposed by Oda et al.(1985) and Ghedia and Sullivan (2012) is further modified to characterize the fabric tensor for granular materials.

The original void fabric tensor in 2D space defined by Oda et al. (1985) is determined as:

$$V_{ij}^{Oda} = 4\left(\frac{1}{L} \sum_{\theta=-90^{\circ}}^{90^{\circ}} \bar{l}_{Oda}^{\theta} n_i^{\theta} n_j^{\theta} - \frac{1}{4} \delta_{ij} \right) \tag{4.1}$$

where n_i^{θ} is the unit vector with inclination θ, δ_{ij} is the identity tensor and L is the total intercept length of voids (Ghedia and Sullivan 2012) , as shown in Fig. 4.3. Ghedia and Sullivan (2012) simplified Eq.(4.1) into the following form:

$$V_{ij}^{Ghe} = \frac{1}{L} \sum_{\theta=-90^{\circ}}^{90^{\circ}} \bar{l}_{Ghe}^{\theta} n_i^{\theta} n_j^{\theta} \tag{4.2}$$

where $\bar{l}_{Ghe}^{\theta}$ is the mean length of line cutting voids at an angle θ (i.e., the Mean Intercept Length), which is defined as:

$$\bar{l}_{Ghe}^{\theta} = \frac{\text{Total length of voids measured by scan lines inclined at angle } \theta}{\text{Total number of individual voids crossed by scan lines at angle } \theta} \tag{4.3}$$

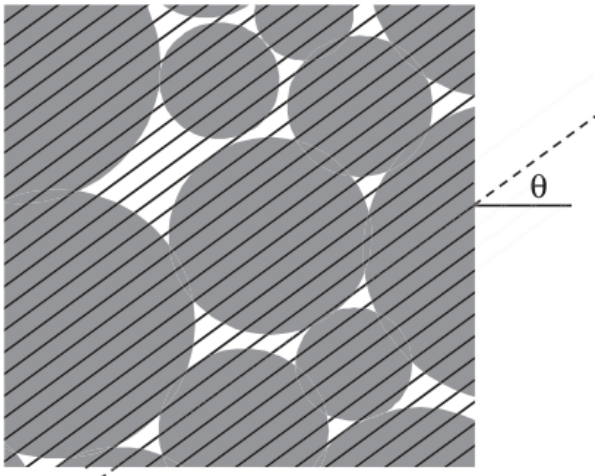

(a) general configuration of scan line method

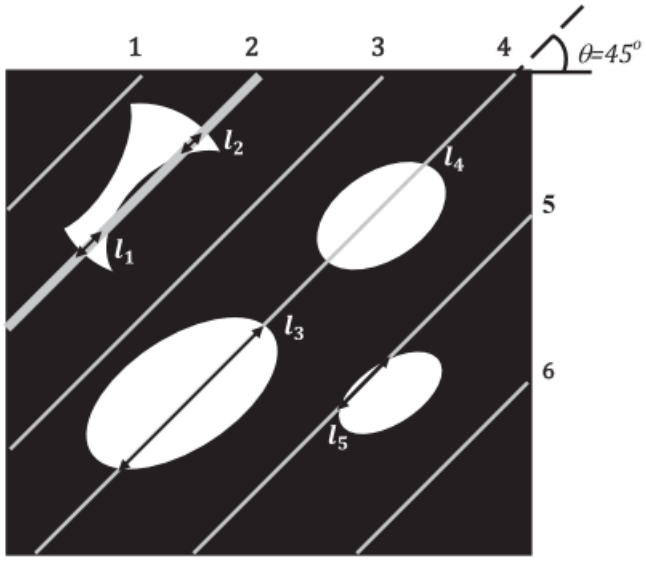

(b) θ=45°

Fig. 4.3 illustration of scan line method employed by Ghedia and Sullivan (2012)

Although Gehdia and Sullivan (2012) show that V_{ij}^{Ghe} defined in Eq.(4.2) captures the anisotropy of pore space distribution, it is inappropriate under some circumstances. As an example, let us examine a single elliptical void with horizontal scan lines shown in Fig. 4.4. In this case, the number of void is 1. The summation of all the intercept length is a function of scan line space Δy such that:

$$\begin{aligned} \bar{l}_{Ghe}^{\theta=0^\circ} &= \sum_{-b}^{b} \bar{l}_i^{\theta=0^\circ} = \sum_{-b}^{b} 2a(\sqrt{1-y^2/b^2}) \\ &= \frac{1}{\Delta y}\left[\sum_{-b}^{b} 2a(\sqrt{1-y^2/b^2})\Delta y\right] \\ &\approx \frac{1}{\Delta y}\int_{-b}^{b} 2a(\sqrt{1-y^2/b^2})dy = \frac{\pi ab}{\Delta y} \end{aligned} \tag{4.4}$$

where a and b is the half axis length of the ellipse. It can be seen that the Mean Intercept Length in this case is a constant assuming that the line space does not change with direction. It is also noted that the mean intercept length is independent of the scan line direction.

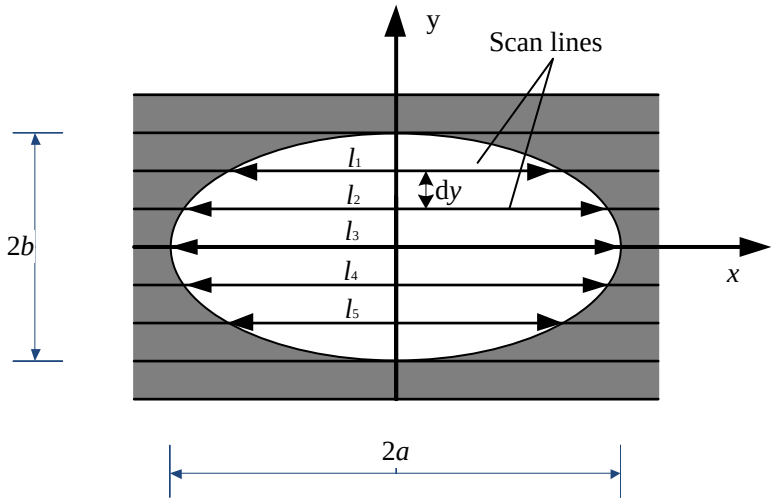

Fig. 4.4 A single ellipse void; Note: white and grey pixels represent void and solid part respectively

In order to avoid the problem in Eq.(4.4), two alternative descriptors are defined:

1) The average intercept length that is over the summation of all the intercept length of voids along all scan lines in the same direction θ:

$$\bar{l}_{All}^{\theta} = \frac{1}{N_v}\sum_{i=1}^{N_v} l_i^{\theta} \tag{4.5}$$

where N_v is the number of line segments that fall in voids. Refer to Fig. 4.5, in this case, N_v=15 and $\overline{l}_{All}^{\theta}$ can be calculated as:

$$\overline{l}_{All}^{\theta} = \frac{1}{15}(l_1 + l_2 + ... + l_{14} + l_{15}) \tag{4.6}$$

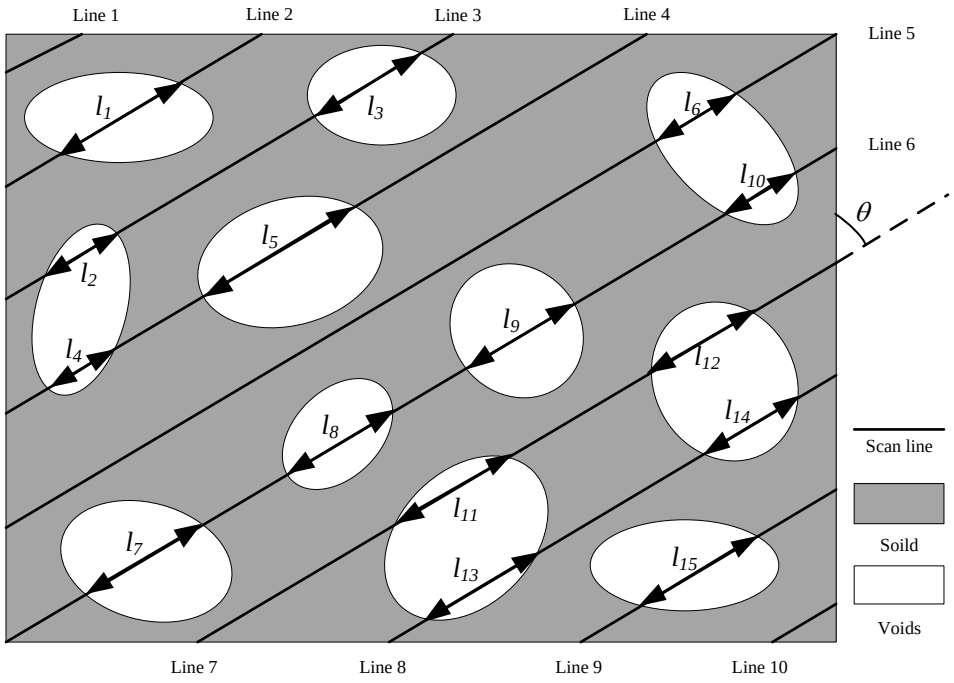

Fig. 4.5 illustration of scan line methods using multiple voids

2) The average of the mean intercept length of all scan lines in the direction θ:

$$\overline{l}^{\theta} = \frac{1}{15}(l_1 + l_2 + \ldots + l_{14} + l_{15}) \tag{4.7}$$

where N_{SCL} is the number of scan lines in direction θ and N_{vSCL} is the number of voids along a specific scan line in this direction. Refer to Fig. 4.5 again, N_{SCL}=10 and N_{vSCL} varies for different scan line, e.g, N_{vSCL} =2 for line 4 and N_{vSCL} =4 for line 6. In this case, $\overline{l}^{\theta}$ can be calculated as:

$$\bar{l}^{\theta} = \frac{1}{10}\left[l_1 + \frac{l_2 + l_3}{2} + \frac{l_4 + l_5}{2} + l_6 + \frac{l_7 + l_8 + l_9 + l_{10}}{4} + \frac{l_{11} + l_{12}}{2} + \frac{l_{13} + l_{14}}{2} + l_{15} \right] \quad (4.8)$$

In terms of the single elliptical void in Fig. 4.4, for both definitions, the theoretical $\bar{l}^{\theta=0}$ are computed as:

$$\begin{aligned} \bar{l}^{\theta=0} &= \frac{1}{2b/\Delta y}\sum_{-b}^{b} l_i^{\theta=0} = \frac{1}{2b}\sum_{-b}^{b} 2a(\sqrt{1-y^2/b^2})\Delta y \\ &\approx \frac{1}{2b}\int_{-b}^{b} 2a(\sqrt{1-y/b^2})dy = \frac{\pi ab}{2b} = \frac{\pi a}{2} \end{aligned} \quad (4.9)$$

and $\bar{l}^{\theta=90^{\circ}} = \pi b/2$. It is shown that the proposed definitions are better to be used in implementing the scan line method. The differences of these two definitions lie in the capability of handling low-quality image and will be discussed in later section.

4.3.1 2D formulation

Following Oda et al. (1985) and Ghedia and Sullivan (2012), the fabric tensor is defined as:

$$V_{ij} = 4\left(\int_{\Omega} l(\mathbf{v}) v_i v_j d\Omega - \frac{1}{4}\delta_{ij} \right) \quad (4.10)$$

where $l(\mathbf{v})$ is a dimensionless Normalized Mean Intercept Length in the direction of the unit vector ***v*** defined as:

$$l(\mathbf{v}) = \frac{\bar{l}(\mathbf{v})}{L} \quad (4.11)$$

with $\bar{l}(\mathbf{v})$ is the Mean Intercept Length in the direction ***v*** and L is defined as:

$$L = \int_{\Omega} \bar{l}(\mathbf{v}) d\Omega \quad (4.12)$$

$l(\mathbf{v})$ can also be expressed as:

$$l(\mathbf{v}) = \frac{1}{2\pi} V_{ij} v_i v_j \tag{4.13}$$

In discretized form, the fabric tensor is expanded as:

$$V_{ij} = 4\left(\frac{1}{L} \sum_{\theta=-90^\circ}^{90^\circ} \bar{l}^{\theta} \begin{bmatrix} \cos^2\theta & \cos\theta\sin\theta \\ \cos\theta\sin\theta & \sin^2\theta \end{bmatrix} d\theta - \frac{1}{4}\delta_{ij} \right) \tag{4.14}$$

with:

$$L = \sum_{\theta=-90^\circ}^{90^\circ} \bar{l}^{\theta} \Delta\theta \tag{4.15}$$

Although several researchers (Ghedia and Sullivan, 2012; Kuo et al., 1998) have implemented this formulation, a new program was developed in Matlab using the built-in Image Processing Toolbox (IPT) which is straightforward and more accurate.

Before discussing details of the numerical algorithm implemented in Matlab, it is necessary to introduce the data organization manner and direction convention in IPT. In general, the best way to store data in Matlab is the form of matrix, so as for the images. However, the direction convention in Matlab is slightly different from the intuitive one we usually use. The data entries of a matrix are stored in a column-major order, which means the elements of the first column are stored together in order (first direction/row number) and then the second column (second direction/column number). When a matrix is treated as an image, however, the first dimension (row number) is the second Cartesian axis (*y*-axis), and the second dimension (column number) is considered as the first Cartesian

axis (*x*-axis). Fig. 4.6(a) gives an example how a 4-by-4 logical matrix is displayed in IPT with the Cartesian axes superimposed on the image (note that the gridline will not be displayed in IPT and the grey color will be pure black). A 3D image is stored as 3D matrix with *x*-*y* plane called a "page".

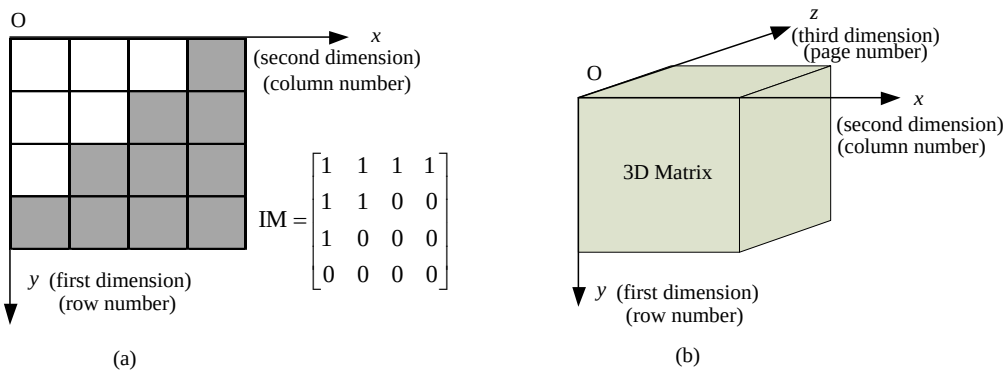

Fig. 4.6 data storage format and direction convention in IPT

The main framework of the Matlab script is shown in Fig. 4.8 and each part of the program is explained in details as follows.

The basic task of implementing the scan line method can be divided into four steps: 1) to define a scan line which makes an angle with *x*-axis; 2) to find out the intersecting points between the image and the scan line; 3) to determine the length of each segment and the phase (void/solid) it lies in; 4) to count the number of continuous phase segments and sum up the length statistics. The general practice is to keep the image unchanged and superimpose the scan line as well as the gridlines onto the image. By calculating the coordinates of the intersecting points using the equation of the scan line, the intercept

length of each phase can be obtained. However, due to the discrete nature of the image and the scan line, some approximation has to be made. Also, the problem of "ghost points" has to be addressed properly, e.g., Ghedia and Sullivan (2012). In this study, the Matlab built-in function *imrotate*() is utilized to rotate the image rather than the scan lines. Refer to Fig. 4.7, the function *imrotate*() rotates the input image by an angle in a counterclockwise direction around its center point. If the "method" of "loose" is used, a bigger image maybe generated to contain the original image. The extra part of the new image will be filled with zeroes. As the original image also has zeroes (voids), it may mix up with the new generated zeroes. In order to overcome this problem, all the entries of the original image are increased by 1 before rotation. The reason of doing this is that the scan line can keep horizontal (parallel to *x*-axis) so that the angle between the scan line and *x*-axis is kept the same, φ in Fig. 4.7. In this way, the coordinates of the intersecting points on the scan line, which can be easily obtained, could be directly used as the indices to extract the gray value from the matrix, i.e., the ordinates are the row number and abscissa are the column number. More details about this feature will be discussed in the sub function *SingleScan.m*.

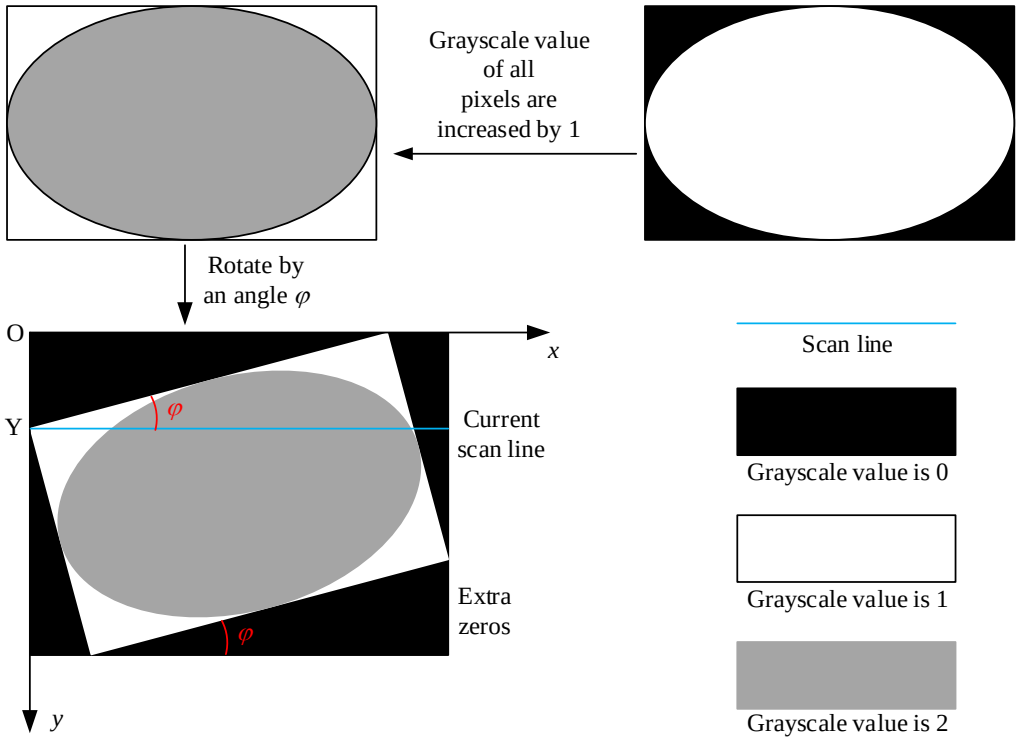

Fig. 4.7 the rotation of a binary image

For *SingleScan.m*, the input parameters are the rotated image as well as the position of the current scan line. As the scan line is always horizontal, the position of the current scan line can be solely determined by the *y* value, denoted as Y, see Fig. 4.7. The abscissa will keep the same: from 1 to the size of the second dimension of the matrix (it is a vector denoted as **X**). A vector pair (**Y, X**) generated from Y and the size of **X** can be used as the indices to extract values from the matrix, denoted as (**Y**, **X**). Regarding the segments lying in the extra zeroes, the function *find*() can be employed to locate the indices of the zeroes and then these indices can be excluded from the index vector pair (**Y**, **X**). Since the original part of the image has been increased by 1, the artificial zeroes can be easily removed from

the calculation. In this whole process, only the operation of matrix is needed and no calculation of the analytical intersecting points is required.

If the concept of Representative Element Area/Volume (REA/V) is to be implemented into the program, the method discussed above could also be used: compute the distance from every point to the center point, use the function *find*() to locate those points whose distances are greater than the radius of the REA/V and exclude those points from the scan line.

SingleScan is next used to compute the intercept length and count the number of voids intercepted by scan lines. Before doing this, a vector of 1's have to be deducted from the grey value of the pixels of the scan line (a vector) as they have been increased by 1's before image rotation. Then the total intercept length of particles can be obtained by summing up the vector entries (1 represents particle and 0 represents voids). The total length is the size of the scan line vector and then MIL is the difference between the total length and the intercept length of particles. The number of voids can be obtained by a counter marching along the scan line. It is straightforward and the details will be omitted here. The flow chart of *SingleScan* is shown in Fig. 4.9.

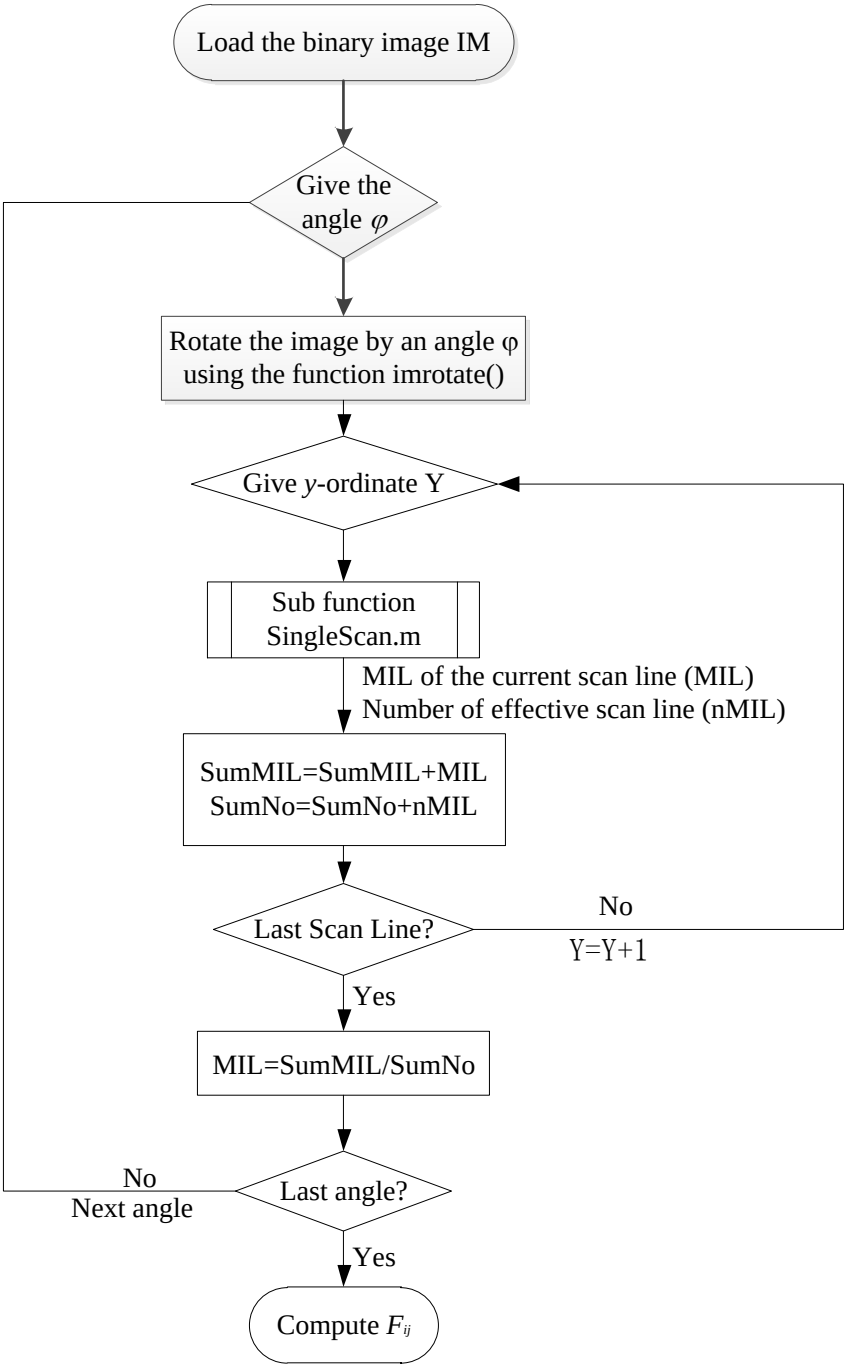

Fig. 4.8 the main framework of the 2D program

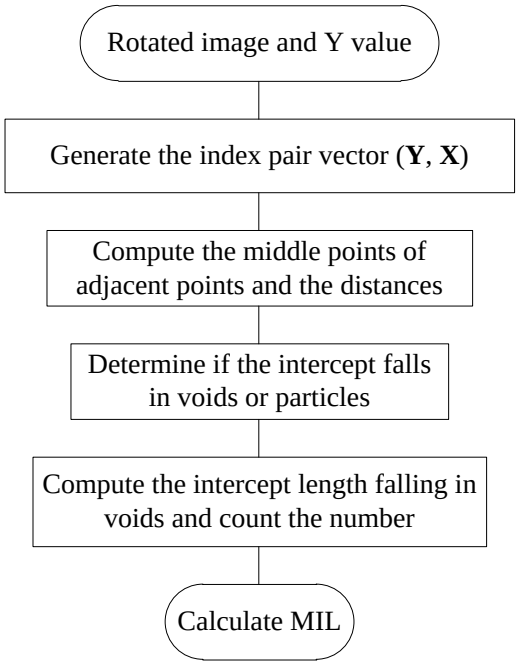

Fig. 4.9 The sub function *SingleScan*()

4.3.2 3D formulation

The fabric tensor based on a direction dependent quality in the 3D space is defined as (Oda et al. 1985):

$$V_{ij} = \frac{15}{2}\left(\int_{\Omega} l(\mathbf{v}) v_i v_j d\Omega - \frac{1}{5}\delta_{ij} \right) \tag{4.16}$$

where $l(\mathbf{v})$ is the Normalized Mean Intercept Length in direction **v** and it has been explained in Eq.(4.11) and Eq.(4.12). **v** is the unit vector determined by:

$$\mathbf{v} = \{\sin\varphi\cos\theta, \sin\varphi\sin\theta, \cos\varphi\}^{\mathrm{T}} \tag{4.17}$$

where (φ, θ) is the direction of the unit vector, see Fig. 4.10.

In 3D case, $l(\mathbf{v})$ can be written as:

$$l(\mathbf{v}) = \frac{1}{4\pi} V_{ij} v_i v_j \tag{4.18}$$

In discretized form, the fabric tensor is expanded as:

$$V_{ij} = \frac{15}{2}\left(\frac{1}{L}\sum_{k=1}^{m} \bar{l}^{(k)} v_i^{(k)} v_j^{(k)} \Delta\Omega - \frac{1}{5}\delta_{ij} \right) \tag{4.19}$$

or

$$V_{ij} = \frac{15}{2}\left\{ \left(\frac{1}{L}\sum_{\theta}\sum_{\varphi} \bar{l}^{(\theta,\varphi)} \begin{bmatrix} \sin^2\varphi\cos^2\theta & \sin^2\varphi\sin\theta\cos\theta & \sin\varphi\cos\varphi\cos\theta \\ \sin^2\varphi\sin\theta\cos\theta & \sin^2\varphi\sin^2\theta & \sin\varphi\cos\varphi\sin\theta \\ \sin\varphi\cos\varphi\cos\theta & \sin\varphi\cos\varphi\sin\theta & \cos^2\varphi \end{bmatrix} \right) - \frac{1}{5}\delta_{ij} \right\} \tag{4.20}$$

where $L = \sum_{\Omega} \bar{l}(\mathbf{v})\Delta\Omega$.

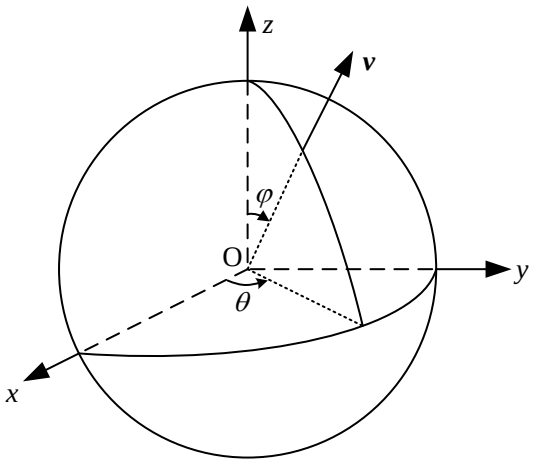

Fig. 4.10 illustration of the direction of the unit vector

It is noted that the integral in Eq.(4.16) is replaced by a summation. According to the rules of numerical integration, the angles (θ,φ) in Eq.(4.20) cannot be sampled or discretized evenly in the 3D space (Mattias and Malcolm, 1999). Instead, the angles should be sampled based on Gauss Quadrature rules. The Gauss points and the corresponding

weighting coefficients can be found in Mattias and Malcolm (1999).

When performing digital image analysis, 3D image is stored as a 3D matrix, of which each entry represents the grey value of the corresponding point. In Eq. (4.20), the *MIL* is required along every direction determined by θ and φ. The *MIL* is determined in the following two steps, refer to Fig. 4.11.

1) Find out all the slices which makes an angle θ with *x*-O-*z* plane, e.g., slice OBCD and EFGH. On these slices, any line in this plane makes an angle θ with *x*-axis. After getting all the grey scale value information on the slice, it can be sampled out and treated as a 2D image.

2) The slice is re-plotted in Fig. 4.11 (b) and re-labeled following the direction convention in IPT, i.e., *y*'-axis is the first dimension of the matrix and *x*'-axis represent the second. Using the 2D code (needs a little modification to be used as a sub function), the MIL can be easily computed.

Again, the slices are not obtained by analytically calculating the intersecting points between the plane and the cube. It is achieved by a similar way described in 2D code. The objective is to get a set of parallel slices (planes) which makes an angle θ with *x*-axis (denoted as Γ^{θ}). From the point of operating a matrix, it is easier to get a slice normal to any of the principal directions than getting a slice inclined at a non-right angle to them. This merit will be taken advantaged in implementing the algorithm. Refer to Fig. 4.11(a), any Γ^{θ}

can be obtained by rotating the plane *z*-O-*x* by an angle θ around a pole which is in this plane and parallel to *z*-axis, e.g., OD, EH, etc.. Therefore, if all the slices which is normal to *z*-axis (parallel to *x*-O-*y* plane) rotate in the opposite direction by an angle θ, a new 3D image (matrix) will be generated, which is possibly bigger than the original due to the filling of extra 0's (refer to Section 4.3.1 for explanation). Note that the size along *z*-axis doesn't change. Now the task is simplified into getting a set of planes parallel to the plane *z*-O-*x*. It can be achieved by extracting 2D matrix from the 3D matrix in the following manner:

$$2D\_IM = 3D\_IM(Y, :, :) \tag{4.21}$$

where *2D_IM* and *3D_IM* are the extracted 2D image slice matrix and 3D matrix respectively; *Y* changes from 1 to the size of the first dimension of the 3D matrix.

After getting the 2D slice matrix, the rest of the job will be the same with the 2D program with the exception that only one angle φ is needed for the scan lines.

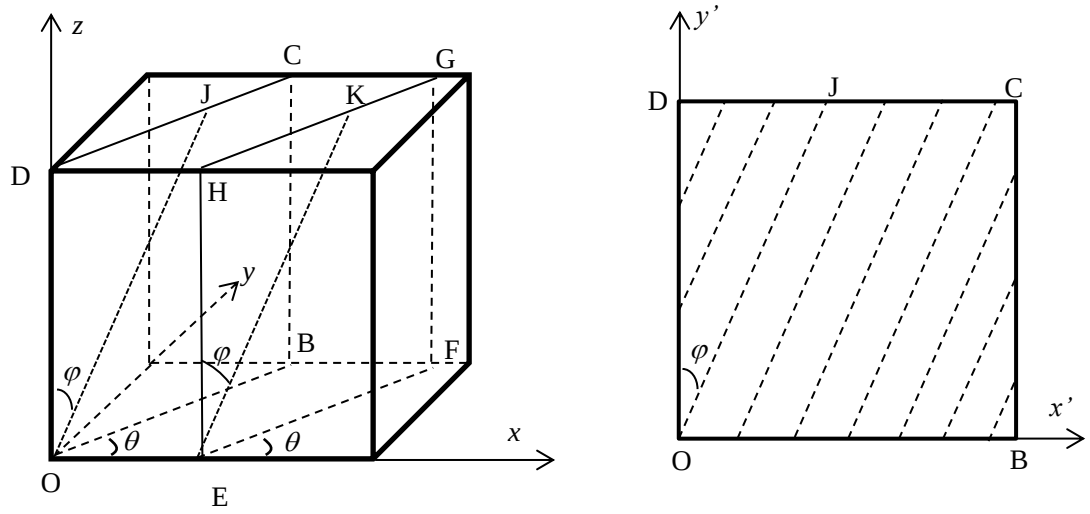

(a) 3D view of the image (b) 2D view of one slice

Fig. 4.11 Schematic diagram of 3D images

4.3.3 The implementation of Areal Pore Size

The concept of Areal Pore Size distribution (*APS*) proposed by Inglis and Pietruszczak (2003) is also implemented in this study. This quantity represents the pore size in the plane perpendicular to the direction of interest.

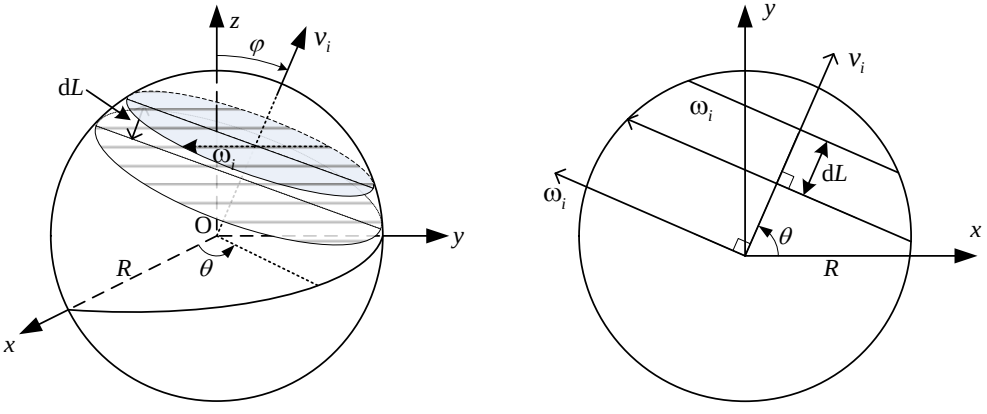

(a) *APS* in 3D space (b) *APS* in 2D space

Fig. 4.12 The definition of *APS*

The definition of Areal Pore Size (*APS*) defined by Pietruszczak (2003) is explained as follows:

Refer to Fig. 4.12 (a), let us examine a set of parallel planes with a unit normal v_i superimposed on a spherical representative volume with a radius of *R*. The distance between the planes is d*L*. On each plane, uniformly distributed scan lines along the direction of ω_i (perpendicular to v_i as they are in the plane) are used to obtain Mean Intercept Length in this direction:

$$g(\omega_i) = \frac{\sum I(\omega_i)}{N(\omega_i)} \tag{4.22}$$

where $I(\omega_i)$ is the segment length of scan line that lies in void phase and $N(\omega_i)$ is the number of the segments in the direction of ω_i. This quantity is averaged over all directions and normalized by 2π:

$$\rho_A(v_i) = \frac{1}{2\pi}\int_{C(v_i)} g(\omega_i)\mathrm{d}C \tag{4.23}$$

$\rho_A(v_i)$ is the average *MIL* on the plane perpendicular to v_i. Finally, *APS* is obtained by averaging $\rho_A(v_i)$ over all the planes:

$$APS(v_i) = \frac{1}{2R}\int_{-R}^{R} \rho_A(v_i)\mathrm{d}L \tag{4.24}$$

The discrete form of Eq.(4.24) is:

$$APS(v_i) = \frac{1}{M}\sum_{j=1}^{M}\rho_A^{(j)}(v_i); \quad \rho_A^{(j)}(v_i) = \frac{1}{k}\sum_{k}\frac{\sum I(\omega_i^{(k)})}{N(\omega_i^{(k)})}; \quad \omega_i^{(k)}\cdot v_i = 0 \tag{4.25}$$

where *M* is the number of planes perpendicular to **v**.

The above expression is defined in 3D space. However, it can also be expressed in 2D space. Refer to Fig. 4.12 (b), the plane in Fig. 4.12 (a) which is perpendicular to v_i is replaced by a line in the direction ω_i in 2D condition. Therefore, the following holds:

$$\rho_A(v_i) = g(\omega_i) = \frac{\sum I(\omega_i)}{N(\omega_i)} \tag{4.26}$$

and

$$APS(v_i) = \frac{1}{M}\sum_{j=1}^{M}\rho_A^{(j)}(v_i); \quad \rho_A^{(j)}(v_i) = \frac{\sum I(\omega_i)}{N(\omega_i)}; \quad \omega_i^{(k)} \cdot v_i = 0 \tag{4.27}$$

It can be seen that $APS(v_i)$ in 2D space is merely the Mean Intercept Length in the direction $\boldsymbol{\omega}$, which is perpendicular to the direction of $\boldsymbol{v}$. In other words, $APS(v_i)$ can be viewed as the average pore size in the direction perpendicular to **v**. This also holds for the 3D scenario: if the cross sections of the pore space in the direction of $\boldsymbol{v}$ are all circles with the same diameter, the void in this direction can be treated as a circular pipe and the *APS* in this direction is readily determined as the diameter of the pipe.

The technique of rotating images rather than calculating the intersection points between planes and the 3D image is also employed here. In the original definition (Eq.(4.24)), *APS* and $\rho_A(v_i)$ are both obtained in a spherical representative volume with a radius *R*. However, a more general method is to include the whole 3D image as the sampling domain. It is relatively easy to incorporate the concept of representative volume in the program as discussed in the previous sections. Therefore, the following discussion focuses on the analysis using the whole 3D image (matrix).

Refer to Fig. 4.13, OJ is in the direction of v_i as defined in Eq.(4.25). It is determined by the angle pair (φ, θ). ADC and BEKL are two examples of planes perpendicular to v_i. It is clear that the intersection of the cut-out plane with the 3D image is not necessarily a rectangular shape. A 2D Cartesian coordinate system is associated to the two cut-out slices following the IPT direction convention. The orientation of coordinate axes on the slices can be arbitrary since the orientation of the scan line varies from 0 to 2π.

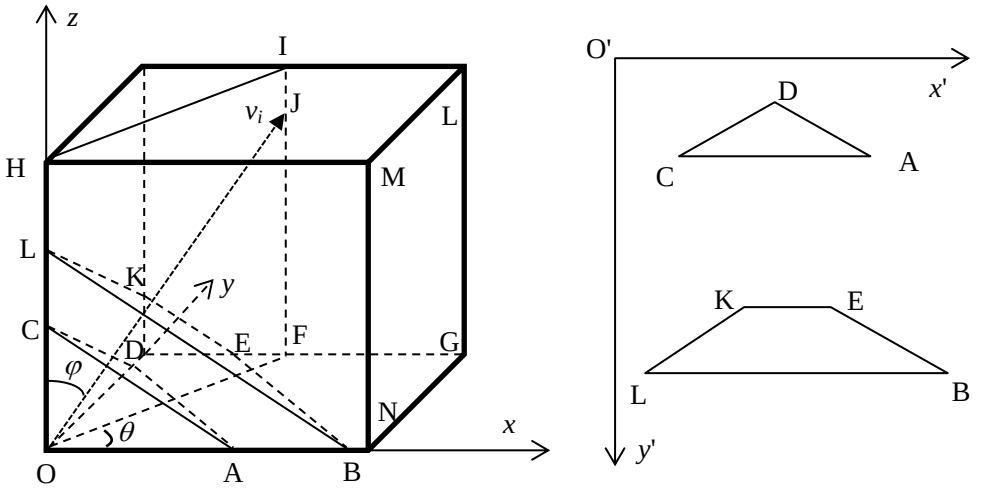

(a) 3D view of the image (b) 2D view of the slices

Fig. 4.13 Schematic diagram of 3D images and the sampling planes

The critical task now is how to rotate the images to obtain the cutting out planes without analytical calculations. Refer to Fig. 4.13, when $\varphi=\pi/2$ and $\theta=0$, OJ is along x-axis. The corresponding cut-out plane will be a set of planes parallel to y-O-z plane. Rotation of OJ in x-O-y plane by an angle $\theta\neq0$ is equivalent to rotating all x-O-y planes in the opposite direction by the same amount while fixing OJ. The 2D slice image (matrix)

can be obtained by using the same method in Eq.(4.21):

$$2D\_IM = 3D\_IM(:, X, :) \tag{4.28}$$

with X ranging from 1 to the second dimension of the new generated 3D image (matrix).

Now consider the new generated 3D image (matrix) after rotating all x-O-y planes by an angle θ, only φ is the angle needs to be addressed. Now, OJ can only be in x-O-z plane or planes parallel to x-O-z plane. If $\varphi=\pi/2$, OJ is in the same direction with z-axis. If $\varphi\neq\pi/2$, it can be obtained by rotating z-axis by an angle $\pi/2-\varphi$ in x-O-z plane. This is equivalent to rotating all x-O-z plane images in the opposite direction by the same amount. Eq.(4.28) still applies here to get the 2D images (matrix).

After the 2D images are obtained, the mean intercept length on each plane can be computed using the developed 2D algorithm which is adapted to a sub function *imageprocess.m*. Averaging, either it is in-plane or over planes with the same direction normal is performed to determine the measure of *APS*. A fabric tensor can finally be constructed based on this measure following Eq.(4.20). It should be noted that the mean intercept length in Eq.(4.20) is replaced by *APS*. The identification process is shown in Fig. 4.14.

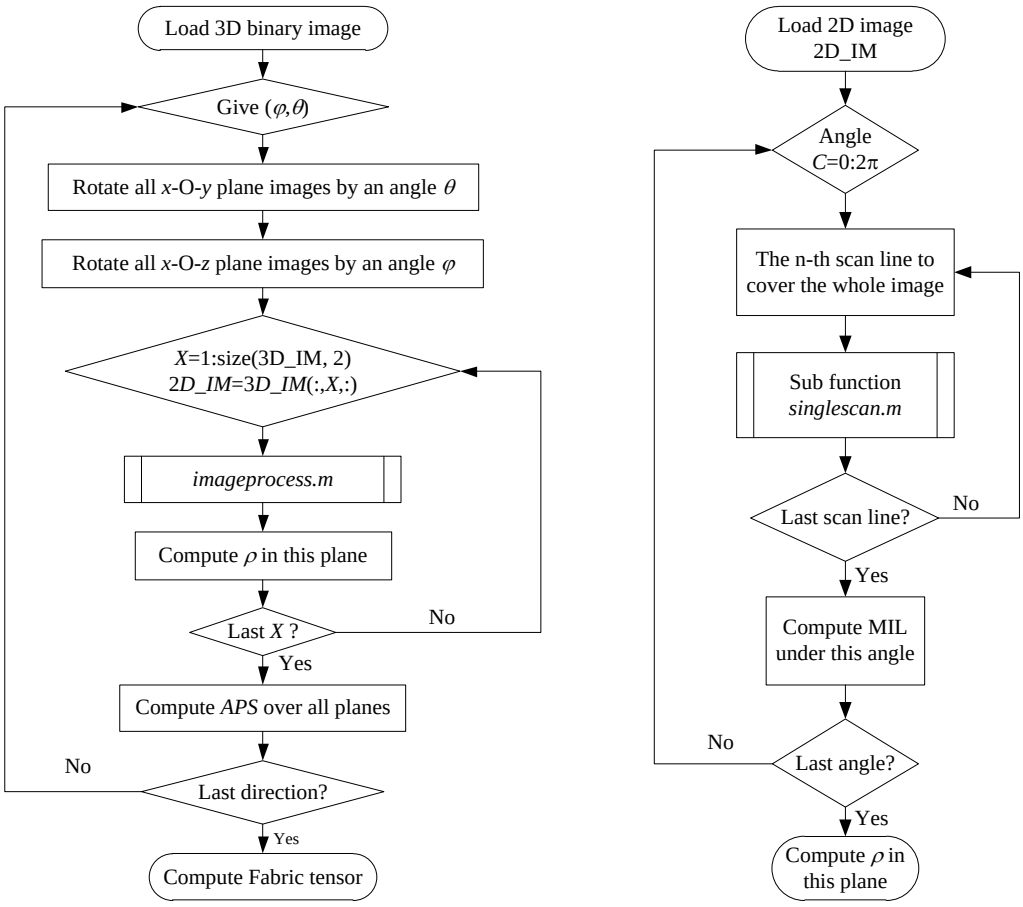

(a) 3D operation (b) The sub function *imageprocess.m*

Fig. 4.14 The flowcharts to calculate the fabric tensor based on *APS*

4.4 Verification of the developed algorithms

The most intuitive way to verify a program is to apply the program to some simple image of which the analytical value of the desired quantities are known. In this section, a circle and ellipses with different semi-axes length will be analysed with the program. The results will be compared with the analytical values.

4.4.1 Absolute length verification

The key part of all the algorithms presented in this chapter is the 2D program. All the quantities are constructed from the Mean Intercept Length in a 2D plane. The accuracy of the 2D program affects all the following calculations. The primary difference between the algorithm developed in this study and that in the literature is the rotation of the image rather than the scan lines. This raises a question: are the properties of the original image are retained after rotation? This will be examined first.

A single circle and an ellipse enclosed by a rectangular domain are rotated by an angle, varying from 0 to 2π. The relative percent error of area and void fraction of different phases are calculated at different angle. The relative percent error is defined as:

$$err(\xi) = \frac{|\xi - \xi_0|}{\xi_0} \times 100\% \qquad (4.29)$$

where ξ is the quantity examined in the rotated image and ξ_0 is the value of the original image (the angle is 0).

The test image consists of a circle with a diameter of 100 pixels enclosed by a square domain with a side length of 105 pixels. The inside of the circle is defined as void (grayscale value=0) and the other part is defined as solid (grayscale value=1). The void fraction ratio (*VFR*) is calculated as 71.2% and the area of the void is 7845 pixel^2. The relative percent error of the two quantities obtained using the proposed algorithm are presented in Fig. 4.15.

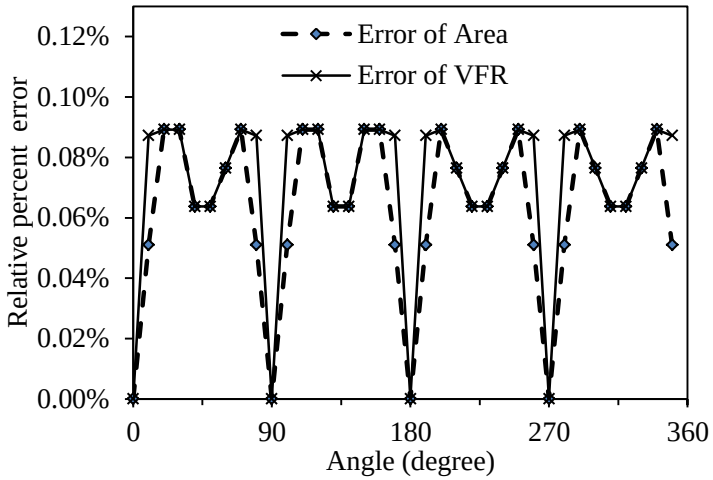

Fig. 4.15 Relative percent error of the area of the void and the void fraction ratio when the image is rotated by different angles

As shown in Fig. 4.15, the maximum error is less than 0.1% for both quantities. The results clearly show that both the area and the *VFR* can be calculated correctly from the rotated image.

Next, the absolute value of the *MIL* of a circle is examined. The analytical value of MIL intersected by a set of scan lines at an arbitrary angle is:

$$MIL = \frac{1}{n}\sum_{1}^{n} y(x) = \frac{1}{d/\Delta x}\sum_{1}^{n} y(x) = \frac{1}{d}\sum_{1}^{n} y(x)\Delta x \qquad (4.30)$$

when $n \to \infty$, one has

$$MIL = \frac{1}{d}A = \frac{1}{d}\frac{1}{4}\pi d^2 = \frac{1}{4}\pi d \qquad (4.31)$$

For a circle with d=100 pixel, the theoretical Mean Intercept Length is *MIL*=78.5 pixel. Fig. 4.16 presents the relative error of the calculated *MIL* using the rotated image. Two definitions (Eq. (4.5) and Eq.(4.7)) of the discrete form of *MIL* are used. As shown in the figure, *MIL* estimated according to Eq. (4.5) deviates more than that based on the second

definition from the analytical value. The error is induced by the discrete nature of the image, since the intercept number on the boundary could be miscounted after the image is rotated.

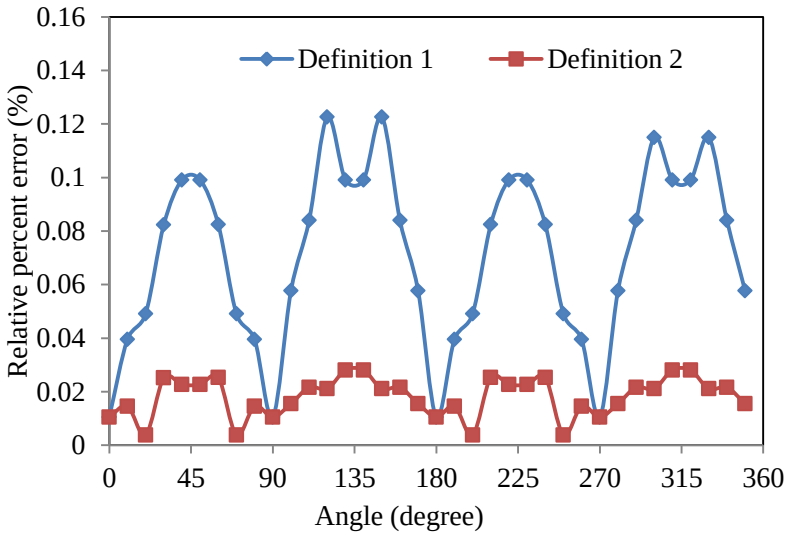

Fig. 4.16 Relative error of the computed MIL using two different definitions

Refer to Fig. 4.17, the black part represents the extra zero's due to the operation of rotation; the white part represents the particle and the grey part represents the void. The red lines are the scan lines which intersect the image. As can be seen, the boundaries of the solid and void parts are inevitably "rough". This leads to a miscounting of the number of the voids if the first definition is used. Ideally, the boundary should be perfectly smooth and the number of the void intercepts should be one for all the three scan lines. However, due to the "rough" boundary of the void, the numbers of the void intercepts of the three scan lines are 4, 3 and 2 respectively (from top to bottom). Although there is very little influence on the total intercept length, the number of the intercepts is

misleading. When the size of the image is small, this may induce significant error. However, if the second definition is used, the intercepts on the boundary are first averaged and counted as one void segment. In this way, the influence of the rough boundary is minimised. Therefore, the second definition of *MIL* provides improved estimate. This is particularly important for images of poor quality.

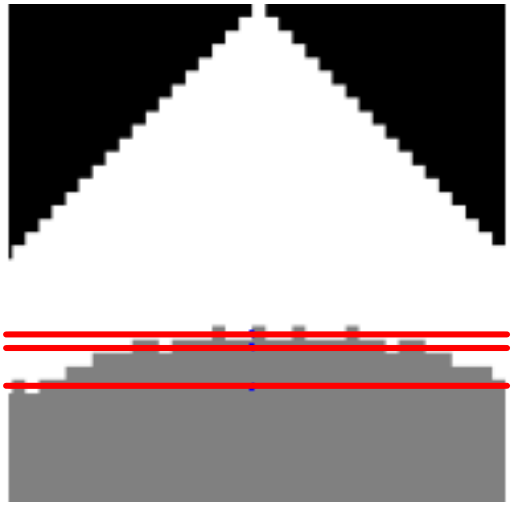

Fig. 4.17 An illustration of the discrete boundary of an image after rotation

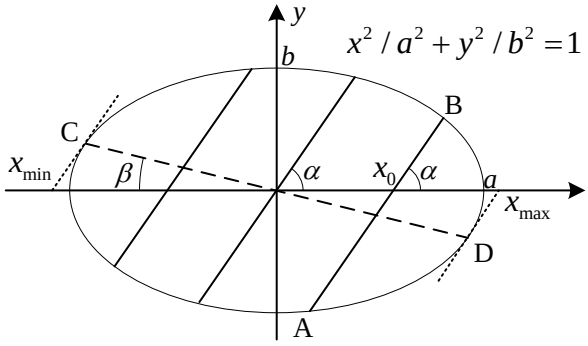

Fig. 4.18 single elliptical void

The second case used to verify the code is an elliptical void with axial lengths being 200 and 100 pixels respectively (a=100, b=50, see Fig. 4.18). In order to verify the

accuracy of the developed code, we should first determine the theoretical value of *MIL* that varies with the direction of scan lines, as shown in Fig. 4.18.

According to Eq.(4.9), the theoretical values of *MIL* when α=0 or α=π/2 are computed as πa/2 and πb/2, respectively. When $\alpha \neq 0$ or π/2, the length of an arbitrary chord AB can be expressed as:

$$l_{\mathrm{AB}} = \frac{2\sqrt{2}ab\tan\alpha}{a^2\tan\alpha^2 + b^2}\sqrt{a^2\tan\alpha^2 + b^2 - {x_0}^2\tan\alpha^2} \qquad (4.32)$$

The theoretical value of *MIL* is then:

$$MIL = \frac{1}{x_{\max} - x_{\min}}\int_{x_{\min}}^{x_{\max}} \frac{2\sqrt{2}ab\tan\alpha}{a^2\tan\alpha^2 + b^2}\sqrt{a^2\tan\alpha^2 + b^2 - {x_0}^2\tan\alpha^2}\,dx_0 \qquad (4.33)$$

where the elliptical integral can be calculated numerically. The detailed derivation of above equations as well as the numerical integration can be found in Appendix, section 4.7.

The theoretical and measured values of *MIL* at different angles are presented in Fig. 4.19. It can be seen that, the measured values are very close to the theoretical values.

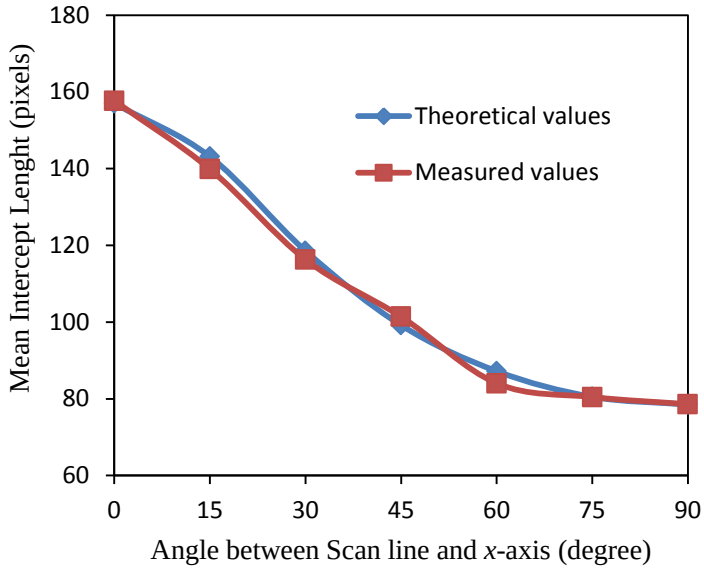

Fig. 4.19 Comparison between the measure and theoretical values of MIL

Regarding the 3D cases, some ellipsoids with different axial lengths are considered. The principal axes of the ellipsoid coincide with the axes of the Cartesian coordinate system. Due to the difficulty to derive the analytical *MIL* in an arbitrary direction, only the expressions of *MIL* along principal directions are considered. For an ellipsoid, the theoretical value of *MIL* along principal directions can be found in Inglis (2001):

$$MIL = \frac{2}{3} l \tag{4.34}$$

where l is the axial length of the ellipsoid along the direction being examined. The parameters of the ellipsoids, the analytical *MIL*, the measured *MIL* as well as the relative percent error are summarized in Table 4.1. The maximum relative percent error is 0.2%, proving the accuracy of the developed code.

Table 4.1 Analytical and measured MIL values of ellipsoids with different sizes

Axial length			Analytical MIL			Measured MIL			Percent error		
x	*y*	*z*	*x*	*y*	*z*	*x*	*y*	*z*	*x*	*y*	*z*
100	100	100	66.7	66.7	66.7	67.0	67.0	67.0	0.05	0.05	0.05
200	100	100	133.0	66.7	66.7	133.0	67.0	67.0	0.05	0.1	0.1
100	200	100	66.7	133.0	66.7	67.0	133.4	67.0	0.05	0.05	0.05
100	100	200	66.7	66.7	133.0	66.7	66.7	133.4	0.05	0.05	0.05
200	100	50	133.0	66.7	33.3	133.6	66.7	33.3	0.20	0.05	0.1

Note: the unit of Axial length and *MIL* is pixels and the percent error %; *x*, *y* and *z* are the directions along which a quantity is measured.

4.4.2 Characterizing the degree of anisotropy

The main purpose of the developed code is to compute the fabric tensor based on the Mean Intercept Length of voids or other descriptors. It is necessary to examine if the program is able to capture the anisotropy of a known pore structure. The Degree of Anisotropy (*DA*) is defined as the ratio between the maximum and minimum eigenvalues of the computed fabric tensors, which are determined using Eq.(4.14) and Eq.(4.20) for 2D and 3D images respectively.

4.4.2.1 Single void

1) A series of 2D images with single elliptical void with varying Aspect Ratio (*AR*) between 0.2~3.0 are first examined, see Fig. 4.20 (a).

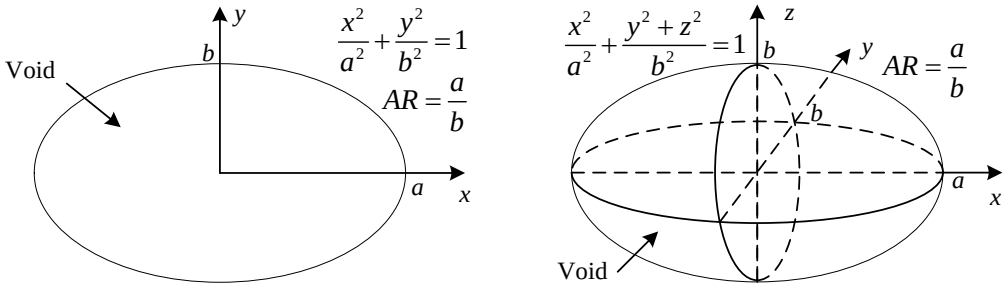

(a) 2D case (b) 3D case

Fig. 4.20 Single elliptical void

As an example, the fabric tensor of two elliptical voids with aspect ratio (*AR*) being 1.0 and 2.0 are computed as:

$$F_{ij}^{AR=1.0}=\begin{bmatrix}1.0000 & 0.0012\\ 0.0012 & 1.0000\end{bmatrix} \quad DA=1.00 \tag{4.35}$$

$$F_{ij}^{AR=2.0}=\begin{bmatrix}1.3311 & 0.0005\\ 0.0005 & 0.6689\end{bmatrix} \quad DA=1.99 \tag{4.36}$$

The degree of anisotropy (*DA*) of each case is plotted against the *AR* in Fig. 4.21. A linear relationship between the degree of anisotropy and the aspect ratio of the void is obtained demonstrating that the code is capable of capturing the anisotropy of the single elliptical void, as shown in Fig. 4.21.

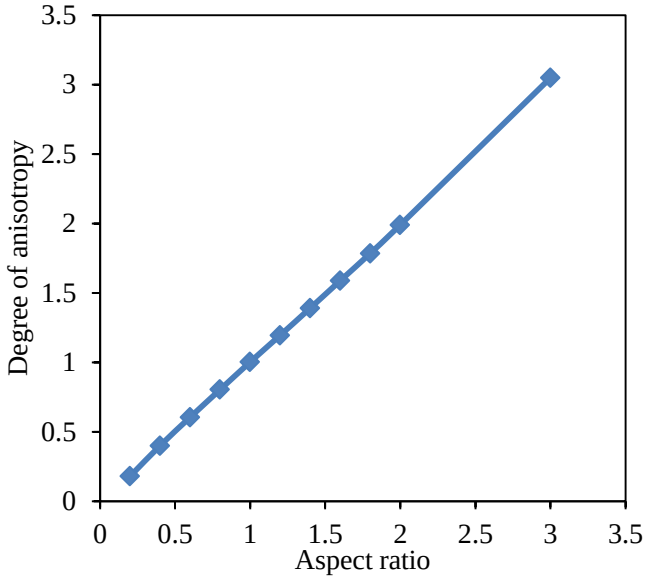

Fig. 4.21 Aspect ratio VS. degree of anisotropy

2) 3D images: ellipsoids with different *AR* are examined using the 3D code. The ellipsoids used here are cross-anisotropic which means that two of the three axes are the same in length. The degree of anisotropy is plotted against the aspect ratio in Fig. 4.22. Note that the degree of anisotropy is computed using two fabric descriptors, i.e., Mean Intercept Length and Areal Pore Size. It can be seen that when the aspect ratio is small, which means the void is isotropic, the degree of anisotropy computed using these two measures tend to be the same. However, the *DA* determined from *MIL* is more sensitive to variation of the aspect ratio. This observation is in agreement with the findings by Inglis (2001).

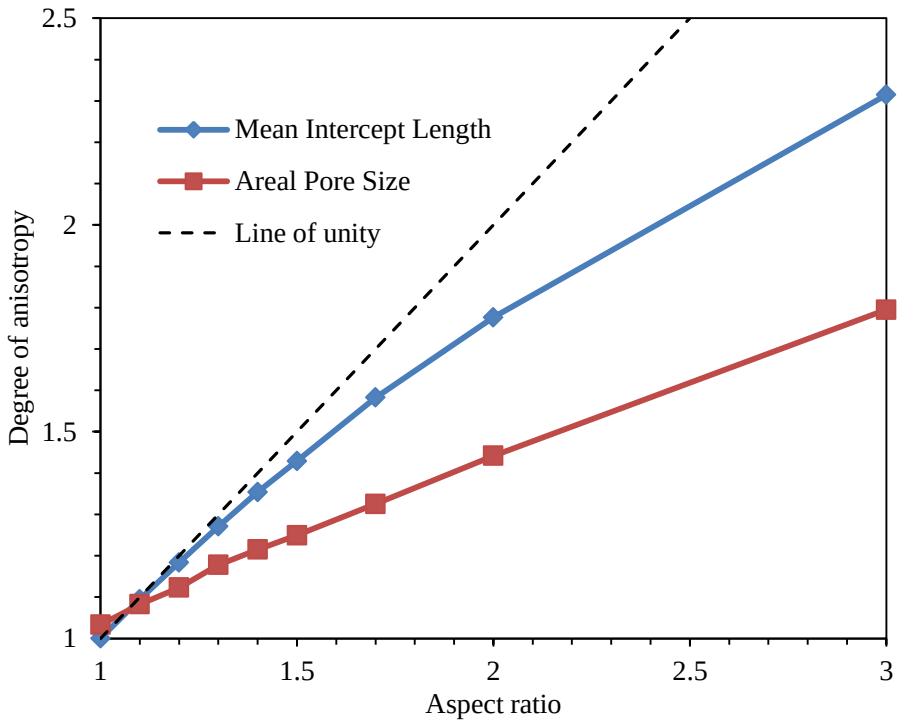

Fig. 4.22 *DA* Vs. *AR* of ellipsoids using two different fabric descriptors

4.4.2.2 Multiple voids

Multiple elliptical voids with different size distribution and packing pattern are studied in this section.

1) Array of mono-sized elliptical voids

The size of the ellipse is a=100, b=50 (Fig. 4.20 (a)). Denote the number or rows as r and columns as c (e.g., 2 rows and 2 columns, in Fig. 4.23). The *MIL* in different directions of each scenario is computed and presented in Fig. 4.24, for cases with r and c varying between 1 and 10.

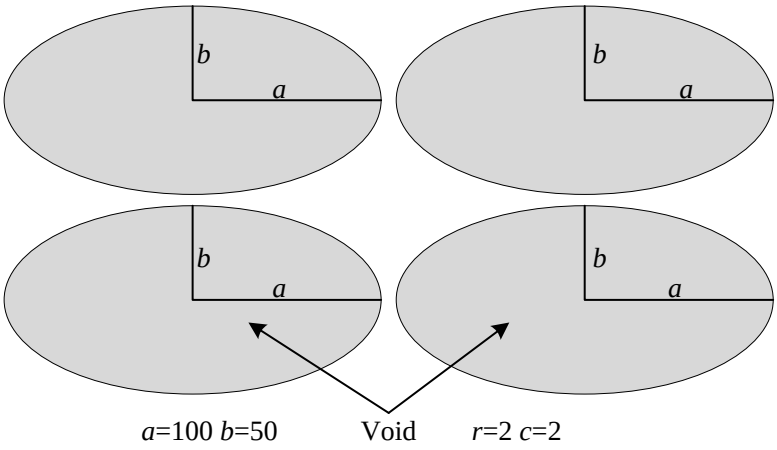

Fig. 4.23 Illustration of regular packing of elliptical voids (2 by 2 array)

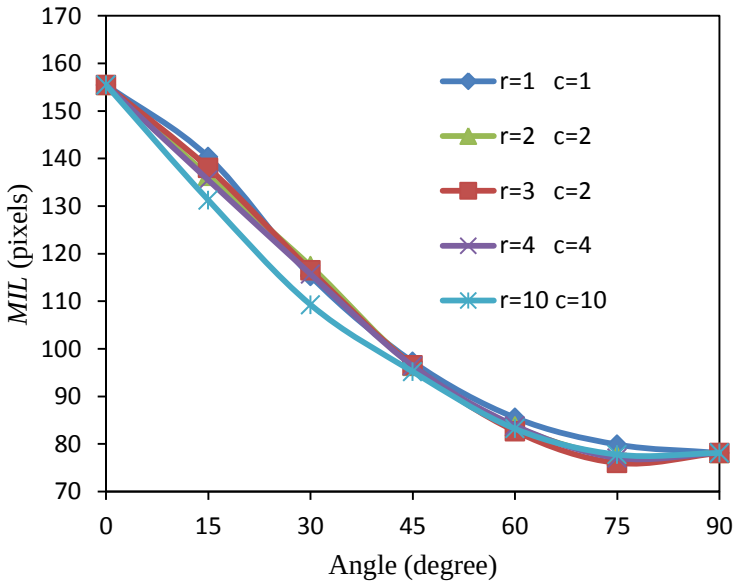

Fig. 4.24 *MIL* of elliptical void packing having different rows and columns

It can be seen from the figure that the *MIL* in different direction of the void packing consisting of multiple mono-sized elliptical voids is the same with the single void. This is reasonable since the *MIL* is averaged over all void segments.

2) Random packing of mono-sized elliptical voids

For this case, mono-sized elliptical voids are packed randomly. Refer to Fig. 4.25,

the direction and number of voids along each direction are listed in Table 4.2. All packing patterns have the same number of voids and each direction has the same number of voids as well. The only difference among Pattern 1 through 3 is the locations of the voids.

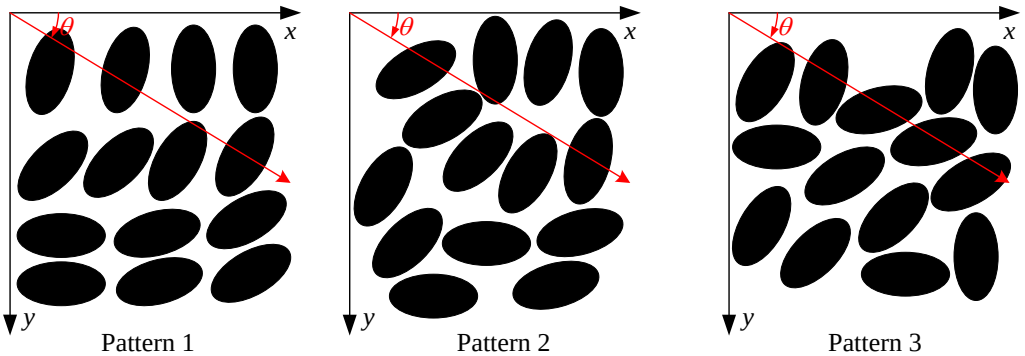

Pattern 1 Pattern 2 Pattern 3

Fig. 4.25 Different patterns of random packing of mono-sized elliptical voids

Table 4.2 Distribution of voids and directions

Direction (degrees)	90	105	120	135	150	165	180
Number of voids	2	2	2	2	2	2	2

Note: The direction is the angle between the major axis of the ellipse and *x*-axis

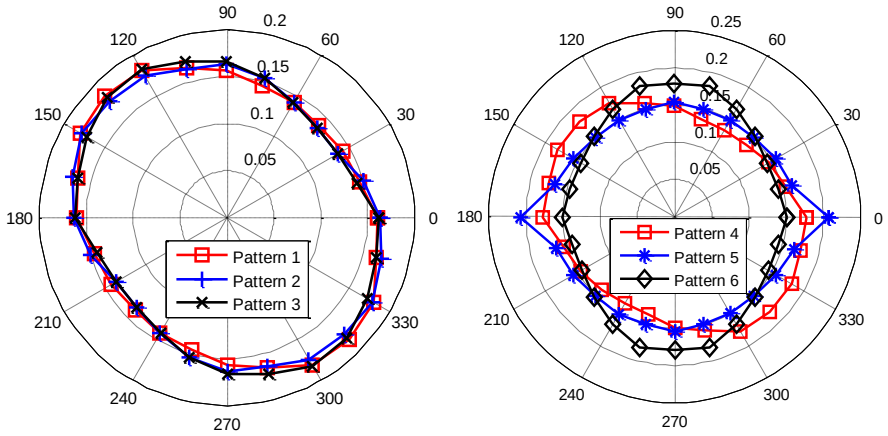

(a) Mono-sized elliptical void packing (b) Multiple-sized elliptical void packing

Fig. 4.26 Normalized MIL variation of different packing patterns

The normalized *MIL* of all patterns are presented in Fig. 4.26 (a). It shows that the overall distribution of *MIL* of all three patterns are very close, which means the *MIL* is

independent of the packing pattern when the constituting voids only change their locations. The rose plot of the *MIL* distribution has a major principal direction around 135°, which is consistent with the principal direction of the pore ellipses listed in Table 4.2. Therefore, the distribution of *MIL*'s can be represented by an ellipse with the major axis direction in the direction of θ=135°. Fig. 4.26 (a) also shows that the positioning of individual void does not have any influence of fabric. Some information has been smoothed out by the process of averaging. This may raise an issue when the voids are aligned in a preferential direction. An extreme condition will be considered and discussed in details later.

3) Random packing of multiple-sized elliptical voids

In this case, both the sizes and orientations of the voids vary randomly, with some extreme conditions being considered. The size of the voids and the orientations are listed in Table 4.3 and illustrated in Fig. 4.27. For Pattern 4, the size of voids gradually get bigger and their directions change from θ=90° to 180°. Pattern 5 and Pattern 6 have only two sizes of voids oriented in two directions.

Table 4.3 Distribution of voids and directions

	Pattern 4							Pattern 5		Pattern 6	
Direction (degree)	90	105	150	135	150	165	180	90	180	90	180
Major axis length (pixel)	40	50	60	70	80	90	100	40	100	100	40
Minor axis length (pixel)	20	25	30	35	40	45	50	20	50	50	20
Number of voids	2	2	2	2	2	2	2	8	6	6	8

Note: The direction is the angle between the major axis of the ellipse and *x*-axis

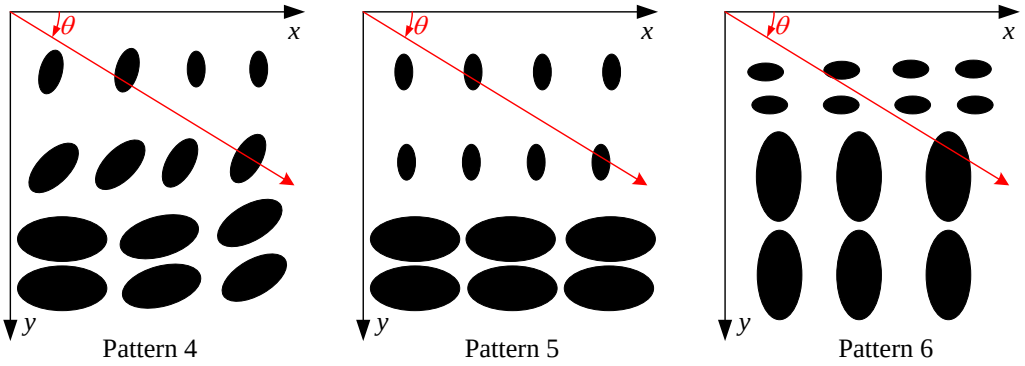

Fig. 4.27 Random packing of multiple-sized elliptical voids

The computed *MIL*'s of Pattern 4 through 6 are presented in Fig. 4.26(b). The rose plot of *MIL* of Pattern 4 has a major principal direction around 150 °. Table 4.3 shows that the distribution of direction is still symmetric about 135 °, however, the void sizes of the voids with θ close to 180 ° are bigger than that of the voids with θ around 90 °. The major principal direction of the rose plot of *MIL* drifts from 135 ° towards 180 °. This is more obvious in Pattern 5 and 6. The maximum *MIL* of Pattern 5 and 6 appears clearly at 180 ° and 90 ° respectively. The difference between the principal directions of *MIL* in Patterns 5 and 6 is related to the dominant orientation of large size voids. In other words, not only the void orientation, but also the void sizes affect the principal direction of *MIL*. The size of the voids plays the role as a weighting factor for the void orientation.

4.4.3 Comments

Overall, the descriptors for pore structure as well as the corresponding fabric tensors are able to capture the anisotropy of the voids. However, under some circumstances, an

approach of volume homogenization may undermine some features of the internal structure. As an example, Fig. 4.28 (a) presents a periodic packing of three circular voids and (b) shows the directional variation of *MIL*. It can be seen that the packing is almost isotropic in terms of *MIL*. However, Fig. 4.28 (c) shows that the distributions of intercept length along two selected directions are different. It means that even though the average value of intercept length (*MIL*) may be the same, the distributions of individual intercept length could be different. Such difference is lost in the process of averaging.

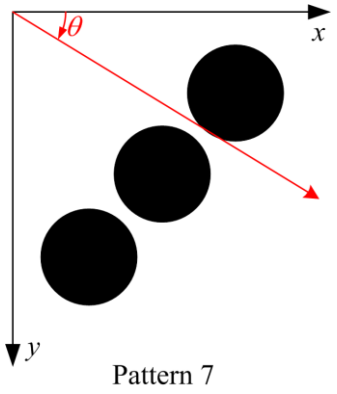

(a)

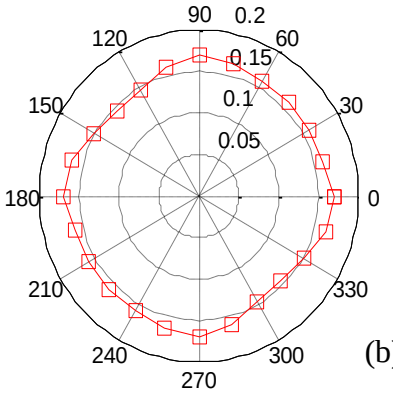

(b)

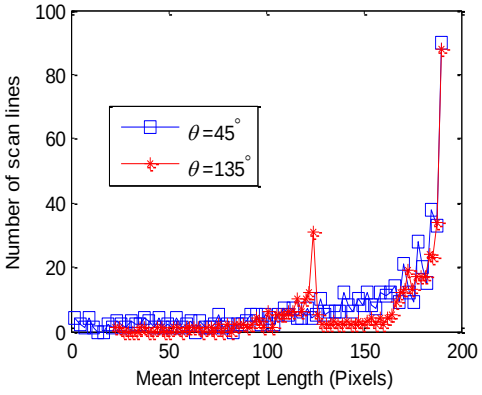

(c)

(a) Periodic packing with circles

(b) Normalized *MIL*

(c) The distribution of intercept length along two directions

Fig. 4.28 Illustration of periodic packing of circular voids and the measured *MIL*

4.5 Microstructure reconstruction of 3D CT scan images

4.5.1 Pre-processing of the raw CT images

The images obtained from CT scan are grayscale bitmap, as shown in Fig. 4.29 (a). However, the developed code in this chapter needs binary images as input, either 2D or 3D. Therefore, before processing, the grayscale images have to be converted into binary images. A MATLAB script is developed to implement this process automatically following the procedures below:

1) The stake of images is first smoothed using an adaptive noise-removal filtering algorithm (Lim 1990). By filtering, the gray-scale value of each pixel is replaced by an average value of the neighbourhood pixels so that isolated darker pixels surrounded by brighter pixels can be removed, or vice versa. The purpose of this step is to remove the artificial noises caused by the CT scanner and the reconstruction program. It can significantly increase the accuracy of the following segmentation operation. An example of filtered image is shown in Fig. 4.29 (b), comparing with the original image shown in Fig. 4.29 (a).

2) The separation of phases (void and solid) is performed using a global image threshold method proposed by Otsu (1979). In the original algorithm, the threshold is chosen to minimize the intraclass variance of the black and white pixels. The operation of threshold is used to convert the grayscale image to binary image, with pixels having

greater gray-scale value being set to one and others to zero. This might be right in a sense of satisfying the algorithm standard, but may not satisfy the physical properties of the specimen, e.g., porosity. As the separation results are directly related to the pore size, correction becomes a must.

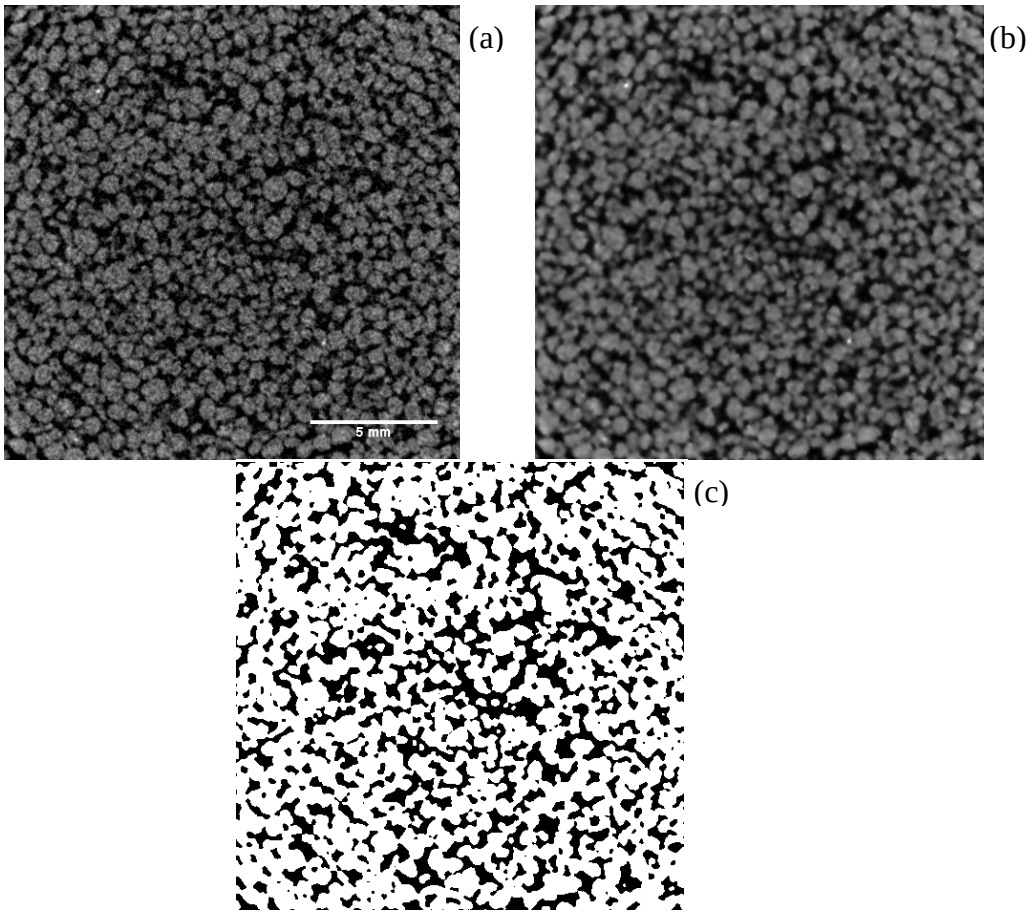

Fig. 4.29 Pictures illustrating the process of image analysis. (a) an original grayscale bitmap of Sand 0. (b) filtered image. (c) binarized image.

In this study, a modification to Otsu's method (1979) is made to ensure the correct global void ratio of the specimen. To achieve this goal, a coefficient λ is applied to the original threshold. Every time λ is changed, the porosity of the stake of binarized images

is calculated and compared with the actual porosity. By changing λ iteratively, the threshold and λ are selected when the "porosity" of image matches that of the specimen. Fig. 4.29(c) illustrates the example of the processed binarized image.

4.5.2 **Results and discussions**

Based on the binary images, the fabric tensors are computed using the code developed in this chapter. The fabric tensor, eigenvalues and the degree of anisotropy are listed as follows:

Ottawa sand made using small cubic mould:

$$F_{ij}^{MIL} = \begin{bmatrix} 1.0018 & -0.0018 & 0.0001 \\ -0.0018 & 0.9995 & 0.0011 \\ 0.0001 & 0.0011 & 0.9987 \end{bmatrix} \quad Eig = \begin{bmatrix} 0.9976 \\ 0.9996 \\ 1.0028 \end{bmatrix} \quad DA = 1.01 \quad (4.37)$$

$$F_{ij}^{APS} = \begin{bmatrix} 1.0031 & 0.0019 & 0.0032 \\ 0.0019 & 1.0077 & 0.0043 \\ 0.0032 & 0.0043 & 0.9891 \end{bmatrix} \quad Eig = \begin{bmatrix} 0.9877 \\ 1.0025 \\ 1.0098 \end{bmatrix} \quad DA = 1.02 \quad (4.38)$$

Ottawa sand impregnated with epoxy resin:

$$F_{ij}^{MIL} = \begin{bmatrix} 1.0709 & 0.0019 & 0.0008 \\ 0.0019 & 1.0808 & -0.0005 \\ 0.0008 & -0.0005 & 0.8483 \end{bmatrix} \quad Eig = \begin{bmatrix} 0.8483 \\ 1.0706 \\ 1.0811 \end{bmatrix} \quad DA = 1.27 \quad (4.39)$$

$$F_{ij}^{APS} = \begin{bmatrix} 0.9730 & -0.0053 & 0.0034 \\ -0.0053 & 0.9677 & 0.0038 \\ 0.0034 & 0.0038 & 1.0593 \end{bmatrix} \quad Eig = \begin{bmatrix} 0.9641 \\ 0.9763 \\ 1.0596 \end{bmatrix} \quad DA = 1.10 \quad (4.40)$$

Lentils sample:

$$F_{ij}^{MIL} = \begin{bmatrix} 1.1781 & -0.0240 & -0.0089 \\ -0.0240 & 1.1224 & -0.0105 \\ -0.0089 & -0.0105 & 0.6995 \end{bmatrix} \quad Eig = \begin{bmatrix} 0.6991 \\ 1.1138 \\ 1.1871 \end{bmatrix} \quad DA = 1.70 \quad (4.41)$$

$$F_{ij}^{APS} = \begin{bmatrix} 0.9253 & 0.0135 & 0.0177 \\ 0.0135 & 0.9543 & 0.0145 \\ 0.0177 & 0.0145 & 1.1203 \end{bmatrix} \quad Eig = \begin{bmatrix} 0.9194 \\ 0.9572 \\ 1.1234 \end{bmatrix} \quad DA = 1.22 \quad (4.42)$$

As discussed in Section 4.2.1.1, the Ottawa sand sample made using small cubic mould cannot represent the one used in permeability test. This is justified by comparing Eq.(4.37) and Eq.(4.38) with Eq.(4.39) and Eq.(4.40). The sample made by using the small cubic mould is basically isotropic, no matter which fabric measure is used.

From Eq.(4.39) to Eq.(4.42), the results show clearly cross-anisotropic features of the specimens made of granular materials using the sand rain method described in Chapter 3. The axis of symmetry is the normal of the bedding plane. The *MIL* in the bedding plane is greater than that in the deposition direction. In the principal space, $F_{ij}(i \neq j)$ is very close to zero which means the fabric tensors are coaxial with the material principal direction. As for the same material, the degree of anisotropy computed by *MIL* is greater than that by *APS*. The principal directions of those two types of fabric tensor are coaxial and the major/minor principal directions are at right angle.

4.6 Summary

In this chapter, Micro-CT is utilized to obtain the microstructure of the samples being investigated. Due to the size effect and the limitation of the micro-CT scanner,

small samples have to be prepared. However, the small sample cannot represent the true microstructure of the full scale sample which is used in permeability test. In order to avoid this problem, resin impregnation procedures are implemented to prepare a larger sample. After the resin impregnated sample solidifies, it is cut into smaller size or oversize scan is used to obtain the microstructure of the sample.

A new algorithm was developed to implement the computation of fabric tensors based on the measures of Mean Intercept Length and Areal Pore Size. Rather than rotating the scan lines and computing the intersection points with the image, the image instead was rotated. As the scan lines always keep horizontal, it is much easier to calculate the intersection points and the intercept length of each phase.

The absolute value of *MIL* of regular shape single void is examined using the developed code and the results are compared with analytical solution. The code is accurate and reliable.

Single elliptical void is examined using the code and it is proven to be able to capture the anisotropy of the void. In terms of void packing, both mono-sized and multiple-sized elliptical voids are considered. It is shown that the code is able to capture the anisotropy of the void.

The sample of Ottawa sand and lentils are scanned using a high resolution CT scanner and the images are processed. The resulting binary images are used to compute

the fabric tensor based on the fabric descriptors. Both materials display cross-anisotropic properties in terms of *MIL* as well as *APS*. The axis of symmetry is in the direction of deposition. The degree of anisotropy of Lentils is greater than that made of Ottawa Sand.

4.7 Appendix Analytical value of *MIL* of a scan line intersecting an elliptical void

Refer to Fig. 4.18, the intersecting points of an arbitrary chord AB and the ellipse can be solved by the following equations set:

$$\begin{cases} \dfrac{x^2}{a^2}+\dfrac{y^2}{b^2}=1 \\ y=\tan\alpha(x-x_0) \end{cases} \tag{4.43}$$

where x_0 is the intersect point between the chord AB and x-axis.

After solving for the coordinates of A (x_A, y_A) and B (x_B, y_B), the length of AB is expressed as:

$$l_{AB}=\sqrt{(x_A-x_B)^2+(y_A-y_B)^2}=\frac{2\sqrt{2}ab\tan\alpha}{a^2\tan\alpha^2+b^2}\sqrt{a^2\tan\alpha^2+b^2-{x_0}^2\tan\alpha^2} \tag{4.44}$$

The *MIL* in the direction α is determined by:

$$\begin{aligned} MIL &= \frac{1}{x_{\max}-x_{\min}}\int_{x_{\min}}^{x_{\max}} l_{AB}\,dx_0 \\ &= \frac{1}{x_{\max}-x_{\min}}\int_{x_{\min}}^{x_{\max}} \frac{2\sqrt{2}ab\tan\alpha}{a^2\tan\alpha^2+b^2}\sqrt{a^2\tan\alpha^2+b^2-{x_0}^2\tan\alpha^2}\,dx_0 \end{aligned} \tag{4.45}$$

where $x_{\min}$ and $x_{\max}$ are the abscissas of the intersecting points of two tangent lines bounding the ellipse. Their values can be determined in three steps:

1) The midpoints of all scan lines in the same direction are all on a straight line and make an angle β with x-axis (Bronshtein et al., 2012). The following holds:

$$a^2 \tan\alpha \tan\beta + b^2 = 0 \tag{4.46}$$

2) The coordinates of intersecting points C (x_C, y_C) and D (x_D, y_D) can be obtained by solving equations set:

$$\begin{cases} \dfrac{x^2}{a^2} + \dfrac{y^2}{b^2} = 1 \\ y = -\tan\beta x \end{cases} \tag{4.47}$$

3) The values of $x_{\min}$ and $x_{\max}$ are:

$$\begin{aligned} x_{\min} &= x_C - \frac{y_C}{\tan\alpha} \\ x_{\max} &= x_D - \frac{y_D}{\tan\alpha} \end{aligned} \tag{4.48}$$

Close scrutiny of Eq.(4.45) shows that the closed form integration does not exist. Numerical integration is needed. Therefore, Eq.(4.49) is used to evaluate the *MIL*.

$$\begin{aligned} MIL &= \frac{1}{N}\sum_{i=1}^{N} l_{AB}^{i} = \frac{\Delta x_0}{x_{\max} - x_{\min}} \sum_{i=1}^{N} l_{AB}^{i} \\ &= \frac{\Delta x_0}{x_{\max} - x_{\min}} \sum_{i=1}^{\Delta x_0/(x_{\max}-x_{\min})} \frac{2\sqrt{2}ab\tan\alpha}{a^2\tan\alpha^2 + b^2} \sqrt{a^2\tan\alpha^2 + b^2 - x_0{}^2\tan\alpha^2} \end{aligned} \tag{4.49}$$

Different value of Δx_0 is used and the computed MIL are presented in Fig. 4.30. It shows that when Δx_0 <5, the MIL will converge to a constant value for any angle.

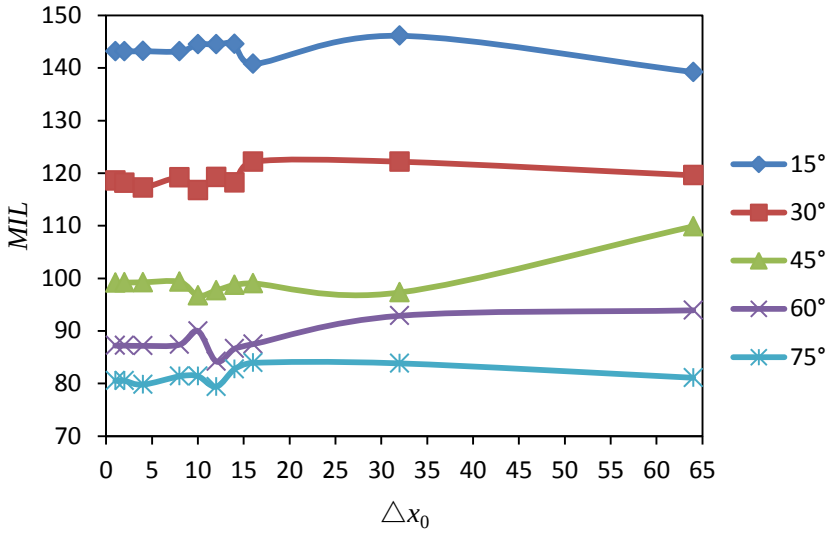

Fig. 4.30 Computed MIL using different Δx_0 values

Chapter 5 Analytical model of anisotropic hydraulic conductivity based on microstructure of porous media

5.1 Introduction

In this chapter, the focus is placed on developing an analytical model bridging the microstructure of porous media and the hydraulic conductivity properties. The microstructure is obtained by micro-CT scan and quantified using the fabric tensors introduced in Chapter 4. The fabric tensors are then incorporated in the model for permeability by the means of volume homogenization. More specifically, tortuosity is made a function of the fabric tensor defined by Mean Intercept Length, which reflects the pore size in the direction of flow. The pore size perpendicular to the flow direction is taken into account via the volume homogenization of local drag force between the solid phase and the fluid.

Since the fabric tensor is involved in the development of the permeability model, once the fabric evolution law under certain stress path is known, the model could be easily extended to the stress induced hydraulic conductivity anisotropy.

5.2 Derivation of the model

5.2.1 Preliminary

For the problem of single phase flow through a homogeneous medium, a Representative Element Volume (REV) can be defined as a minimum volume in which when the size of the volume increases, the physical properties, say porosity or density, does not fluctuate (Bear, 1972). It means that the physical properties of the REV represent the whole medium in a statistical sense and this REV is small enough to facilitate the statistical operation within this volume. As a result, the analysis for the influence on flow can be carried out in the REV shown in Fig. 5.1.

In this REV, the fluid in the pores and the solid particles are referred as phase α and β, respectively.

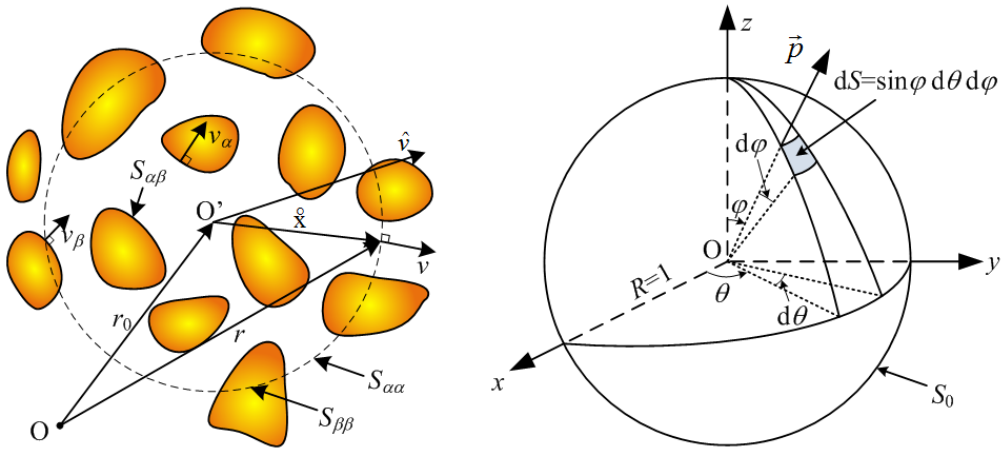

(a) 2D view of the REV (b) 3D view of a unit sphere

Fig. 5.1 Illustrations of the quantities

Some other quantities are defined as follows:

$S_{\alpha\alpha}$: the area around the REV that intersects the fluid (phase α);

$S_{\beta\beta}$: the area around the REV that crosses the particles (phase β);

$S_{\alpha\beta}$: the total area of the interfaces between particles and the fluid;

$S_0 = S_{\alpha\alpha} + S_{\beta\beta}$: the total area enclosing the spherical REV;

$S_{0a} = S_{\alpha\alpha} + S_{\alpha\beta}$: the total area enclosing the fluid;

U_α: the volume of phase α in REV;

U_0: the total volume of REV;

v: the unit normal in the direction determined by (θ, φ);

$dS = R^2 \sin\varphi \, d\varphi d\theta$: the infinitesimal surface area on REV in the direction of v;

$d\Omega = \sin\varphi \, d\varphi d\theta$: the solid angle in the direction of v.

The homogenization of a certain quantity which is a function of its position $f(\boldsymbol{x})$ is performed following Bear and Bachmat's (1990) and Whitaker's (1999) work:

Volumetric intrinsic phase average: $\overline{f}^{\alpha} = \frac{1}{U_\alpha}\int_{V_\alpha} f_\alpha dV$;

Volumetric phase average: $\overline{f} = \frac{1}{U_0}\int_{V_\alpha} f dV$;

Areal intrinsic phase average: $\tilde{f}_A = \frac{1}{S_{0\alpha}}\int_{A\alpha} f dS$;

Areal average: $\tilde{f}_A = \frac{1}{S_0}\int_A f dS$.

5.2.2 Derivation of the permeability tensor

The analytical model developed in the flowing sections follow the same principles in Bear and Bachmat (1990), which is briefly outlined for the sake of completeness.

The macroscopic momentum balance equation of the fluid in a porous medium can be expressed as:

$$\phi\rho_\alpha \frac{\mathrm{D}_\mathrm{m}\overline{V_i^\alpha}^\alpha}{\mathrm{D}t} = -\phi\frac{\overline{\partial p}^\alpha}{\partial x_i} - \phi\overline{\rho g\frac{\partial z}{\partial x_i}}^\alpha + \phi\frac{\overline{\partial \tau_{ij}}^\alpha}{\partial x_j} \qquad (5.1)$$

where $\overline{(.)}$ means the value is the volume average of the corresponding quantity; ϕ is the volumetric porosity of the medium; ρ_α is the density of the fluid; p is the pore pressure at a specific location; V_i is the velocity of the fluid. τ is the drag force exerted by the flowing fluid on the intersection surface between two phases. The physical meaning of the above equation is that the product of mass and acceleration (or the inertial force, LHS of Eq.(5.1)) is equal to the sum of pressure forces, external body forces and viscous forces (three terms on RHS of Eq.(5.1), respectively). All the volume-averaged terms in Eq.(5.1) must be obtained from local quantities through proper homogenization processes.

For steady flow, the inertial force on the LHS is negligible compared to the other three forces on the RHS of Eq.(5.1). Hence it vanishes in the following derivation. The first and second terms on the RHS of Eq.(5.1) can be expanded as:

$$\overline{\frac{\partial p}{\partial x_i}}^{\alpha} + \overline{\rho g \frac{\partial z}{\partial x_i}}^{\alpha} = \phi\left(\frac{1}{\phi U_0}\int_{S_{\alpha\alpha}} \mathring{x}_i v_j \frac{\partial \overline{p}^{\alpha}}{\partial x_j} dS + \frac{1}{\phi U_0}\int_{S_{\alpha\beta}} \mathring{x}_i v_j \frac{\partial \overline{p}^{\alpha}}{\partial x_j} dS\right) + \phi\left(\frac{1}{\phi U_0}\int_{S_{\alpha\alpha}} \mathring{x}_i v_j \overline{\rho}^{\alpha} g \frac{\partial z}{\partial x_j} dS + \frac{1}{\phi U_0}\int_{S_{\alpha\beta}} \mathring{x}_i v_j \overline{\rho}^{\alpha} g \frac{\partial z}{\partial x_j} dS\right) \tag{5.2}$$

Because $\frac{1}{\phi U_0}\int_{S_{\alpha\beta}} \mathring{x}_i v_j \frac{\partial \overline{p}^{\alpha}}{\partial x_j} dS = \frac{1}{\phi U_0}\int_{S_{\alpha\beta}} \mathring{x}_i v_j \overline{\rho}^{\alpha} g \frac{\partial z}{\partial x_j} dS = 0$, the above equation becomes:

$$\begin{aligned}\overline{\frac{\partial p}{\partial x_i}}^{\alpha} + \overline{\rho g \frac{\partial z}{\partial x_i}}^{\alpha} &= \phi\left(\frac{\partial \overline{p}^{\alpha}}{\partial x_j} + \overline{\rho}^{\alpha} g \frac{\partial z}{\partial x_i}\right)\frac{1}{\phi U_0}\int_{S_{\alpha\alpha}} \mathring{x}_i v_j \frac{\partial \overline{p}^{\alpha}}{\partial x_j} dS \\ &= \phi\left(\frac{\partial \overline{p}^{\alpha}}{\partial x_j} + \overline{\rho}^{\alpha} g \frac{\partial z}{\partial x_j}\right) T_{ji}^{*}\end{aligned} \tag{5.3}$$

where

$$T_{ij}^{*} = \frac{1}{\phi U_0}\int_{S_{\alpha\alpha}} \mathring{x}_i v_j dS = \frac{1}{U_{\alpha}}\int_{S_{\alpha\alpha}} \mathring{x}_i v_j dS \tag{5.4}$$

is a second order tensor representing the averaging process and acting as the transformation between the local body forces to the macroscopic ones. It can be seen that it is a function of the geometry of the flow channels. Bear and Bachmat (1990) defined T_{ij}^{*} as the tortuosity tensor.

The last term on the RHS of Eq.(5.1) is the average viscous resistance to the fluid flow, which is determined as follows:

$$\begin{aligned}\overline{\frac{\partial \tau_{ij}}{\partial x_j}}^{\alpha} &\cong -\mu \frac{1}{U_0}\int_{S_{\alpha\beta}} \frac{(V_{\alpha j}^{\alpha} - V_{\beta j}^{\beta})(\delta_{ij} - v_i v_j)}{\bar{\Delta}_\alpha / C_\alpha} dS \\ &= -\mu \frac{C_\alpha}{\bar{\Delta}_\alpha}(\bar{V}_{\alpha j}^{\alpha} - \bar{V}_{\beta j}^{\beta}) \frac{S_{\alpha\beta}}{U_0}\left(\frac{1}{S_{\alpha\beta}}\int_{S_{\alpha\beta}} (\delta_{ij} - v_i v_j) dS\right) \\ &= -\mu \frac{C_\alpha}{\bar{\Delta}_\alpha^2}\phi(\bar{V}_{\alpha j}^{\alpha} - \bar{V}_{\beta j}^{\beta})\left(\alpha_{ij}\right)\end{aligned} \tag{5.5}$$

where $\alpha_{ij} = \frac{1}{S_{\alpha\beta}}\int_{S_{\alpha\beta}} (\delta_{ij} - v_i v_j) dS$ is the surface average of the tangential unit vector of $S_{\alpha\beta}$, which introduces the effect of the configuration of the solid-fluid interface and transforms the force resisting the flow to an averaged viscous force at the fluid-solid surface; $\bar{\Delta}_\alpha$ is the average hydraulic radius defined as $\bar{\Delta}_\alpha = U_\alpha / S_{\alpha\beta}$; C_α is the shape factor depending on the shapes of the cross-section of the flow channels and C_α=2, 1.779 and 1.675 for a circle, square and equilateral triangle, respectively (Bear and Bachmat 1990); $\bar{V}_{\alpha j}^{\alpha} - \bar{V}_{\beta j}^{\beta}$ is the volume average of the relative velocity between the fluid and solid phases.

Inserting Eq.(5.3) and Eq.(5.5) into Eq.(5.1), after some rearrangement, we obtain:

$$\phi(\bar{V}_{\alpha j}^{\alpha} - \bar{V}_{\beta j}^{\beta}) = -\frac{1}{\bar{\mu}_\alpha^{\alpha}}\left(\frac{\phi\bar{\Delta}_\alpha^2}{C_\alpha}\alpha_{ij}^{-1}T_{il}^{*}\right)\left(\frac{\partial \bar{p}^{\alpha}}{\partial x_l} + \bar{\rho}^{\alpha} g \frac{\partial z}{\partial x_l}\right) \tag{5.6}$$

Eq.(5.6) can be considered as the generalized form of Darcy's Law. The term in the first bracket on the RHS of Eq.(5.6) is the intrinsic permeability tensor which is a function of the microstructure of the medium:

$$k_{ij} = \frac{\phi\bar{\Delta}_\alpha^2}{C_\alpha}\alpha_{il}^{-1}T_{lj}^{*} \tag{5.7}$$

The permeability tensor is related to the microstructure by the tortuosity tensor and another tensor α_{ij} which is a function of the microstructure. These two tensors and the hydraulic radius still need to be determined.

5.2.3 Determination of average hydraulic radius

The hydraulic radius $\bar{\Delta}_\alpha$ is defined as the ratio of fluid volume to the fluid-solid interface area (Das, 1983). In the literature (e.g., Revil and Cathles 1999), this quantity is usually estimated by the effective particle size or d_{10} (the particle size in the particle size distribution curve corresponding to 10% finer). In this study, $\bar{\Delta}_\alpha$ is estimated from the particle gradation curve. According to the definition, the average hydraulic radius is computed as:

$$\bar{\Delta}_\alpha = \frac{U_\alpha}{S_{\alpha\beta}} = \frac{\phi}{1-\phi}\frac{U_\beta}{S_{\alpha\beta}} \tag{5.8}$$

where U_α and U_β are the volume of the fluid- and solid-phase in the medium respectively, $S_{\alpha\beta}$ is the fluid-solid interface area and ϕ is the porosity of the medium. Note that $U_\beta / S_{\alpha\beta}$ in Eq.(5.8) is the inverse of the specific surface area of the material in the original Kozeny-Carman equation (Carman 1937; Dullien 1979).

With the knowledge of the particle size distribution and shape of the compositing particles, the volume and the surface area of the particles can be obtained. Eq. (5.8) can be rewritten as:

$$\bar{\Delta}_\alpha = \frac{\phi}{1-\phi}\frac{\sum U_{\beta i}}{\sum S_{\beta i}} \tag{5.9}$$

where $U_{\beta i}$ and $S_{\beta i}$ are the volume and the surface area of the *i*th particle group. Since most of the particle size distribution curves are given in terms of the weight of particle groups of a certain size, Eq.(5.9) can also be expressed in terms of weight W_i of particles in different groups. The particle shape of the materials used in this study are rounded, sub-rounded (Ottawa Sand) or lenticular (Eaton Lentils). The particles are assumed to be transverse-isotropic ellipsoids with aspect ratio *AR*. In other words, if two of the axes of the ellipsoid have the same axis length 2*b*, the third axis length is *AR**2*b*. The formula calculating the volume and surface area of ellipsoid can be found in Broshtein et al. (2012). The hydraulic radius $\bar{\Delta}_\alpha$ is determined as:

$$\begin{aligned}\bar{\Delta}_\alpha &= \frac{\phi}{1-\phi}\frac{\sum \frac{4\pi}{3} AR b_i^3}{\sum 4\pi \left(\frac{1+2AR^{1.6}}{3}\right)^{\frac{1}{1.6}} b_i^2} \\ &= \frac{\phi}{1-\phi}\frac{AR}{3}\left(\frac{3}{1+2AR^{1.6}}\right)^{1.6}\frac{\sum W_i}{\sum W_i / b_i}\end{aligned} \tag{5.10}$$

if the particle is spherical with *AR*=1, Eq.(5.10) simplifies to

$$\bar{\Delta}_\alpha = \frac{\phi}{1-\phi}\frac{1}{3}\frac{\sum W_i}{\sum W_i / r_i} \tag{5.11}$$

with r_i being the radius of the particle in the *i*th particle group.

Utilizing Eq.(5.9) and Eq.(5.10) and the particle size distribution information

presented in Chapter 3, the average hydraulic radius of Sand O (ϕ=0.351) and Lentils (ϕ=0.347) used in the anisotropic permeability tests are computed as 2.42×10^{-5}m and 2.85×10^{-4}m respectively.

5.2.4 Tortuosity tensor and its relation with the fabric

According to the definition in Subsection 5.2.2, the tortuosity tensor is defined as:

$$T_{ij}^{*}=\frac{1}{U_{\alpha}}\int_{S_{\alpha\alpha}}\mathring{x}_i\,v_j\,dS \tag{5.12}$$

where $\mathbf{\mathring{x}=r-r_0}$ with $\mathbf{r}$ and $\mathbf{r}_0$ being the position vectors of a point on $S_{\alpha\alpha}$ and the center of the REV, as shown in Fig. 5.1.

Similar to Guo (2012), consider a test line in the direction of v and passing the center of the REV. If the probability that this test line intercepts voids on S_0 is $P(\mathbf{v})$, T_{ij}^{*} in Eq.(5.12) becomes:

$$T_{ij}^{*}=\frac{1}{U_{\alpha}}\int_{S}P(\mathbf{v})\,\mathring{x}_i\,v_j\,dS \tag{5.13}$$

following Guo (2012), this probability consists of two parts:

$$P(\mathbf{v})=P_1(\mathbf{v})P_2(\mathbf{v}) \tag{5.14}$$

where $P_1(\mathbf{v})$ is the probability for the test line to intersect the voids on the surface of the REV and $P_2(\mathbf{v})$ is the probability for the test line to intersect the voids within the REV. $P_1(\mathbf{v})$ can be considered as the areal porosity on the surface of REV. It should be noted that the average area porosity is the same as the volumetric porosity, i.e., $P_1(\mathbf{v})=\phi$.

The second term $P_2(\mathbf{v})$ can be related to the Normalized Mean Intercept Length $l(\mathbf{v})$ introduced in Chapter 4. It is called "density function" by Oda et al. (1985) reflecting the spatial distribution of voids. Denote $\bar{l}(v)$ as the Mean Intercept Length in the direction of ***v*** and $l(\mathbf{v})$ is a dimensionless measure:

$$l(\mathbf{v}) = \frac{\bar{l}(\mathbf{v})}{L} \tag{5.15}$$

with

$$L = \int_{\Omega} \bar{l}(\mathbf{v}) d\Omega \tag{5.16}$$

and

$$\int_{\Omega} l(\mathbf{v}) d\Omega = 1 \tag{5.17}$$

Define $P_2(\mathbf{v}) = \beta l(\mathbf{v})$ and it should satisfy the following requirement:

$$\int_S P_2(\mathbf{v}) dS = S_{\alpha\alpha} = S_0 \phi \tag{5.18}$$

Therefore:

$$\begin{aligned} &\int_S \frac{\beta l(\mathbf{v})}{\phi} dS = S_0 \\ &\Rightarrow \frac{\beta}{4\pi\phi} \int_{\Omega} l(\mathbf{v}) d\Omega = 1 \end{aligned} \tag{5.19}$$

Comparison of Eq.(5.17) and Eq.(5.19) gives β=$4\pi\phi$ and $P_2(\mathbf{v}) = 4\pi\phi l(\mathbf{v})$. As a result, the tortuosity tensor becomes:

$$\begin{aligned} T_{ij}^{*} &= \frac{1}{U_{\alpha}} \int_{S} \phi [4\pi\phi l(v)] \mathring{x}_i \, v_j dS \\ &= \frac{4\pi\phi^2}{U_{\alpha}} \int_{\Omega} l(v) R v_i v_j R^2 d\Omega \\ &= \frac{4\pi\phi^2 R^3}{\phi 4\pi R^3 / 3} \int_{\Omega} l(v) v_i v_j d\Omega \\ &= 3\phi \int_{\Omega} l(v) v_i v_j d\Omega \end{aligned} \tag{5.20}$$

Recall the definition for fabric tensor in Section 4.3, i.e., Eq.(4.19). The integration term in Eq.(5.20) can be written as:

$$\int_{\Omega} l(v) v_i v_j d\Omega = \frac{2}{15} F_{ij}^{MIL} + \frac{1}{5} \delta_{ij} \tag{5.21}$$

where F_{ij}^{MIL} is the fabric tensor defined by Mean Intercept Length. Therefore, the tortuosity tensor is related to the fabric tensor as:

$$T_{ij}^{*} = 3\phi \left(\frac{2}{15} F_{ij}^{MIL} + \frac{1}{5} \delta_{ij} \right) = \frac{\phi}{5} \left(2F_{ij}^{MIL} + 3\delta_{ij} \right) \tag{5.22}$$

The fabric tensor is a symmetrical tensor with its trace being 3. When the medium being considered is isotropic with regard to *MIL*, $F_{ij}^{MIL} = \delta_{ij}$ and $T_{ij}^{*} = T_{\alpha 0}^{*} \delta_{ij}$ with $T_{\alpha 0}^{*} = \phi$. The tortuosity of an isotropic material increases with the increase of the volumetric porosity.

Alternatively, T_{ij}^{*} can be expressed as:

$$T_{ij}^{*} = \phi \left(\frac{2}{5} D_{ij} + \delta_{ij} \right) \tag{5.23}$$

in which $D_{ij} = F_{ij}^{MIL} - \delta_{ij}$. Eq.(5.23) recovers the tortuosity tensor in Guo (2012).

5.2.5 Fabric dependency of permeability

According to Kanatani (1984) and Inglis and Peitruszczak (2003), the fabric descriptors (*MIL* and *APS*) introduced in Section4.3, Chapter 4 can be expressed:

$$f(v_i) = C(1 + D_{ij}v_iv_j + D_{ijkl}v_iv_jv_kv_l + \ldots) \tag{5.24}$$

where $f(v_i)$ is the value of the descriptor in the direction of $\boldsymbol{v}$; C is the mean value of the corresponding descriptor and $\boldsymbol{D}$'s are traceless, symmetrical even-order tensors. $\boldsymbol{D}$'s describe the deviator components of the fabric tensors. In the simplest scenario, only the second order component is considered:

$$f(v_i) = f_0(1 + D_{ij}v_iv_j) = f_0(\delta_{ij} + D_{ij})v_iv_j \tag{5.25}$$

The bracketed term in Eq.(5.25) can be alternatively expressed as a normalized fabric tensor $A_{ij} = \delta_{ij} + D_{ij}$ with A_{ii}=3 and D_{ii}=0.

In the following section, the fabric tensor defined by Mean Intercept Length (*MIL*) and Areal Pore Size (*APS*) are denoted as F_{ij}^{MIL} and F_{ij}^{APS} which are consistent with Chapter 4. As a result, the Mean Intercept Length in direction $\boldsymbol{v}$ can be expressed as:

$$\bar{l}(v) = \bar{l}_0 F_{ij}^{MIL} v_i v_j \tag{5.26}$$

where $\bar{l}_0$ is the average value of $\bar{l}(v)$ in all directions. Referring to Eq.(5.16), we have:

$$\bar{l}_0 = \frac{\int_\Omega \bar{l}(\mathbf{v})d\Omega}{\int_\Omega d\Omega} = \frac{L}{4\pi} \tag{5.27}$$

Similarly, the Areal Pore Size can be expressed as:

$$APS(v) = APS_0 F_{ij}^{APS} v_i v_j \tag{5.28}$$

where APS_0 is the average value of $APS(\boldsymbol{v})$ in all directions.

To take into account the effect of directional variation of areal porosity and hence the hydraulic radius on permeability, two assemblies of particles illustrated in Fig. 5.2 are examined. In Fig. 5.2 (a), the areal porosity and hence the hydraulic radius is directional dependent. However, in Fig. 5.2 (b), the hydraulic radius of the particle assembly is an equivalent system of assembly (a) with the same porosity and directional variation of *MIL* while the areal porosity is independent of direction. For flow in the same direction $\boldsymbol{v}$, the equivalence is achieved in these two systems when

$$(V_{si}^* |_{S_{\alpha\beta}} - V_i^m | \Delta) A_i = (V_{si}^* |_{S_{\alpha\beta}} - V_i^m | \Delta)^{eq} A_i^{eq} \tag{5.29}$$

in which $V_{si}^* |_{S_{\alpha\beta}} - V_i^m |_{\Delta}$ is the local relative velocity between the α-phase relative to the β-phase, A_i is the local pore area on the plane perpendicular to the $S_{\alpha\beta}$ – surface. The superscript "eq" stands for quantities in the equivalent system of directional-independent assembly Fig. 5.2 (b). It follows that

$$V_{si}^* |_{S_{\alpha\beta}} - V_i^m |_{\Delta} \; A_0 \phi_0 \; \delta_{ij} + D_{ij}^A \; t_j = V_{si}^* |_{S_{\alpha\beta}} - V_i^m |_{\Delta}^{\;eq} A_0 \phi_0 \delta_{ij} t_j \tag{5.30}$$

and

$$V_{si}^* |_{S_{\alpha\beta}} - V_i^m |_{\Delta} = \delta_{ij} + D_{ij}^A \; ^{-1} \; V_{sj}^* |_{S_{\alpha\beta}} - V_j^m |_{\Delta}^{\;eq} \tag{5.31}$$

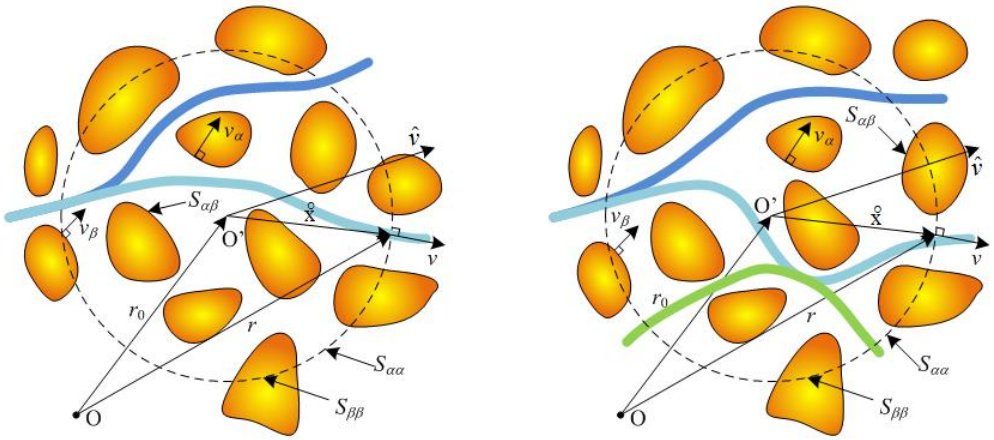

(a) Directional-dependent hydraulic radius (b) Directional independent hydraulic radius

Fig. 5.2 Assembly of granular particles of different configurations

As a result, the local velocity gradient in Assembly (a) is related to that in the equivalent assembly (b) as

$$\begin{aligned}\frac{\partial V_i^m}{\partial s_v} &= \delta_{il} + D_{il}^{A\ -1} \frac{\partial V_l^{eq}}{\partial x_k^{eq}} T_{kj}^{-1} v_j \\ &= \delta_{il} + D_{il}^{A\ -1} T_{lk}^{-1} \frac{\partial V_k^{eq}}{\partial x_j^{eq}} v_j \\ &= \delta_{il} + D_{il}^{A\ -1} T_{lk}^{-1} \frac{\partial V_k^{eq}}{\partial s_v}\end{aligned} \tag{5.32}$$

Using the same method as in Eq.(5.5), the average velocity gradient is determined as:

$$\begin{aligned}\frac{1}{U_0}\int_{S_{\alpha\beta}} \frac{\partial V_i^m}{\partial s_v} dS &= \underbrace{\frac{1}{U_0}\int_{S_{\alpha\beta}} \frac{\delta_{ij} + D_{ij}^{A\ -1}\ V_{sj}^*|_{S_{\alpha\beta}} - V_j^m|_\Delta}{\Delta}\ dS}_{\text{tangential velocity}}^{eq} \\ &= C_\alpha \phi \left[\ \delta_{il} + D_{il} \quad \delta_{lj} + D_{lj}^A\ \right]^{-1} \left(\delta_{jk} - \nu_j \nu_k\right)^{\alpha\beta} \frac{\overline{V_k^m}^\beta - \overline{V_k^m}^\alpha}{\Delta_\alpha^2}\end{aligned} \tag{5.33}$$

The expression of permeability tensor in Eq.(5.7) becomes:

$$k_{ij} = \frac{\phi \bar{\Delta}_\alpha^2}{C_\alpha} \alpha_{im}^{-1} \ \delta_{ml} + D_{ml} \quad \delta_{lk} + D_{lk}^A \ T_{kj}^* \tag{5.34}$$

Replacing $\delta_{ml} + D_{ml}$ and $\delta_{lk} + D_{lk}^A$ with F_{ml}^{MIL} and F_{lk}^{APS} yields:

$$k_{ij} = \frac{\phi \bar{\Delta}_\alpha^2}{C_\alpha} \alpha_{im}^{-1} F_{ml}^{MIL} F_{lk}^{APS} T_{kj}^* \tag{5.35}$$

According to Guo (2012), $\alpha_{ij} = (2\delta_{ij} + T_{ij}^*)/3$, Eq. (5.35) becomes:

$$k_{ij} = \frac{\phi \bar{\Delta}_\alpha^2}{C_\alpha} \left[\frac{1}{3} (2\delta_{im} + T_{im}^*) \right]^{-1} F_{ml}^{MIL} F_{lk}^{APS} T_{kj}^* \tag{5.36}$$

Substituting Eq.(5.22) into Eq. (5.36) gives:

$$\begin{aligned} k_{ij} &= \frac{\phi \bar{\Delta}_\alpha^2}{C_\alpha} \left[\frac{2}{3} \delta_{im} + \frac{1}{3} \frac{\phi}{5} \ 2F_{im}^{MIL} + 3\delta_{im} \ \right]^{-1} F_{ml}^{MIL} F_{lk}^{APS} \frac{\phi}{5} \ 2F_{im}^{MIL} + 3\delta_{im} \\ &= \frac{3\phi^2 \bar{\Delta}_\alpha^2}{C_\alpha} [(10 + 3\phi)\delta_{im} + 2\phi F_{im}^{MIL}]^{-1} F_{ml}^{MIL} F_{lk}^{APS} (2F_{kj}^{MIL} + 3\delta_{kj}) \end{aligned} \tag{5.37}$$

The permeability tensor is connected to the microstructure of the medium by using fabric tensors defined by Mean Intercept Length and Areal Pore Size, which represent the pore size in and perpendicular to the flow direction respectively.

5.3 Comments on the model

5.3.1 Comparison with Kozeny-Carman equation

If the material is isotropic, both of the fabric tensors F_{ij}^{MIL} and F_{ij}^{APS} become δ_{ij} and the permeability tensor shrinks to:

$$k_{ij}^{iso} = \frac{3\phi^2}{2 + \phi} \frac{\bar{\Delta}_\alpha^2}{C_\alpha} \delta_{ij} \tag{5.38}$$

The permeability in any direction is the same:

$$k_0^{iso} = \frac{3\phi^2}{2+\phi}\frac{\bar{\Delta}_\alpha^2}{C_\alpha} \tag{5.39}$$

normalizing the permeability by $\bar{\Delta}_\alpha^2 / C_\alpha$ gives:

$$k_0^{Nor} = \frac{k_0^{iso}}{\bar{\Delta}_\alpha^2 / C_\alpha} = \frac{3\phi^2}{2+\phi} \tag{5.40}$$

Recall the generalized form of Kozeny-Carman equation:

$$k_{KC} = \frac{\phi\bar{\Delta}_\alpha^2}{C_\alpha \tau^2} \tag{5.41}$$

where τ is the hydraulic tortuosity factor.

Regarding the hydraulic tortuosity factor τ, it has been reported in the literature (Dullien 1979; Ho and Strieder 1981; Mauret and Renaud 1997) that τ can be related to porosity ϕ via:

$$\tau = \phi^{-p} \tag{5.42}$$

with p in the range of 0.4~0.5. Normalizing the permeability in Eq.(5.41) by $\bar{\Delta}_\alpha^2 / C_\alpha$ gives:

$$k_{KC}^{Nor} = \frac{k_{KC}}{\bar{\Delta}_\alpha^2 / C_\alpha} = \frac{\phi}{\tau^2} \tag{5.43}$$

The normalized permeability with different expressions of τ are plotted against the porosity in Fig. 5.3. As can be seen from the figure, the normalized permeability predicted using Eq.(5.39) is very close to Kozeny-Carman equation when $\tau = \phi^{-0.4}$.

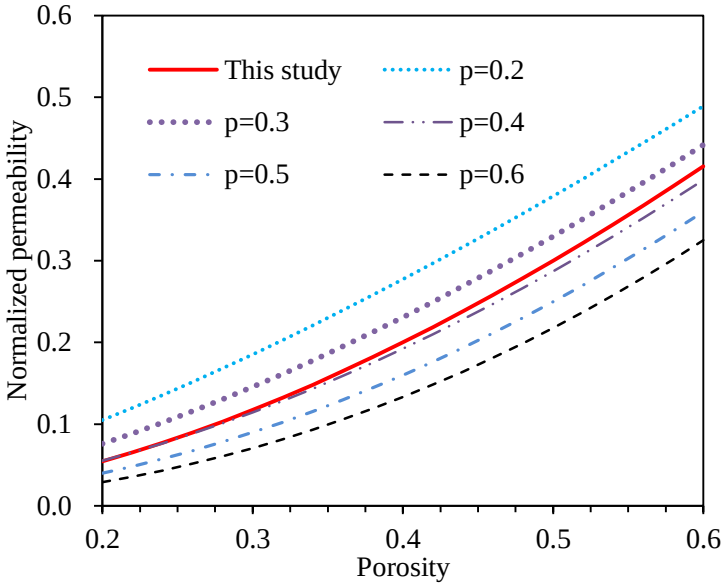

Fig. 5.3 Comparison with Kozeny-Carman equation

5.3.2 Relation between *MIL* and *APS*

Areal Pore Size and Mean Intercept Length describe the sizes of the pore space in two orthogonal directions. These two measures may be correlated to each other since the pore space is an integrated volume with a given volumetric porosity.

Refer to Fig. 5.4, assume the material is cross-anisotropic and the axis of symmetry is *z*-direction (normal of the bedding plane). The fabric tensor based on *MIL* can be decomposed into the following form:

$$F_{ij}^{MIL} = MIL_0(D_{ij} + \delta_{ij}) = \begin{bmatrix} \omega_1 & 0 & 0 \\ 0 & \omega_1 & 0 \\ 0 & 0 & -2\omega_1 \end{bmatrix} + \begin{bmatrix} 1 & 0 & 0 \\ 0 & 1 & 0 \\ 0 & 0 & 1 \end{bmatrix} \tag{5.44}$$

The fabric tensor F_{ij}^{APS} defined by the Areal Pore Size can be expressed as:

$$F_{ij}^{APS} = APS_0(D_{ij}^A + \delta_{ij}) = \begin{bmatrix} \omega_2 & 0 & 0 \\ 0 & \omega_2 & 0 \\ 0 & 0 & -2\omega_2 \end{bmatrix} + \begin{bmatrix} 1 & 0 & 0 \\ 0 & 1 & 0 \\ 0 & 0 & 1 \end{bmatrix} \tag{5.45}$$

where MIL_0 and APS_0 are the spatial average value of *MIL* and *APS*; v_i is the unit vector in the direction of interest; δ_{ij} is the Kronecker delta; D_{ij} and D_{ij}^A are the deviatoric component of the fabric tensor defined by *MIL* and *APS*, respectively.

For linearly independent orthogonal unit vectors **m**, **n** and **v**, the following relation holds,

$$m_i m_j + n_i n_j = \delta_{ij} - v_i v_j \tag{5.46}$$

According to the definition of Areal Pore Size, the *APS* in direction **v** can be expressed as the average of the *MIL* on a plane (**m** and **n** are in this plane) which is perpendicular to **v**:

$$APS(\mathbf{v}) = \frac{1}{2\pi}\int_C MIL(\mathbf{n})dC \tag{5.47}$$

where $n_i v_i$=0 and dC is the differential angle measured in this plane. Eq.(5.47) becomes:

$$\begin{aligned} APS(v) &= \frac{1}{2\pi}\int_C MIL_0(D_{ij}+\delta_{ij})n_i n_j dC \\ &= MIL_0 + \frac{MIL_0}{2\pi}\int_C D_{ij} n_i n_j dC \\ &= MIL_0 + \frac{MIL_0}{2\pi}\int_C \frac{1}{2} D_{ij}(m_i m_j + n_i n_j)dC \\ &= MIL_0 + \frac{1}{2}\frac{MIL_0}{2\pi}\int_C D_{ij}(\delta_{ij} - v_i v_j)dC \\ &= MIL_0\left(\delta_{ij} - \frac{1}{2}D_{ij}\right)v_i v_j \end{aligned} \tag{5.48}$$

Comparison of Eq.(5.48) with Eq.(5.45) yields:

$$D_{ij}^{A} = -\frac{1}{2} D_{ij} \tag{5.49}$$

which means that

$$\omega_2 = -0.5\omega_1 \tag{5.50}$$

To further verify the above correlation between ω_1 and ω_2, two different particle/void systems are generated and these two measures are computed using the program developed in Chapter 4. In case 1, the void is assumed as an ellipsoid with cross-anisotropy (Fig. 5.4). A series of ellipsoidal voids with different aspect ratios are examined. ω_1 and ω_2 are calculated to determine F_{ij}^{MIL} and F_{ij}^{APS} respectively. In case 2, the particles are assumed to be cross-anisotropic ellipsoids with different aspect ratios. Periodical packing shown in Fig. 5.5 is examined. ω_1 and ω_2 are determined by varying the aspect ratio of the particles.

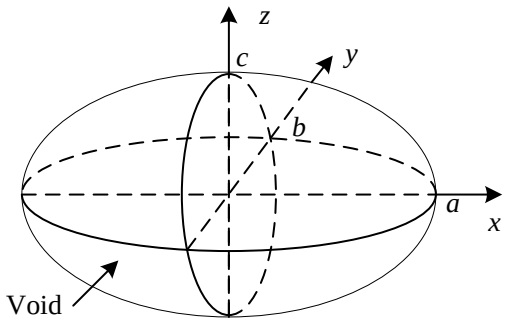

Fig. 5.4 Illustration of cross-anisotropic material

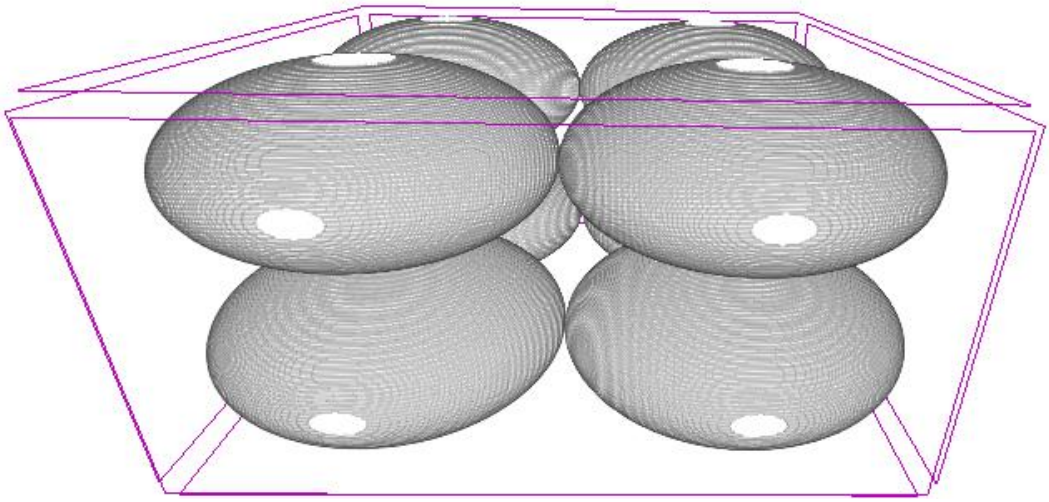

Fig. 5.5 Packing of ellipsoidal particles

The values of ω_1 and ω_2 of different cases with varying aspect ratios of particle/void are computed and presented in Fig. 5.6. For comparison purposes, the laboratory tested materials, Sand O and Lentils, are also included. According to Fig. 5.6, the values of ω_1 (or ω_2) are almost identical no matter the particle is assumed ellipsoid or the void is assumed to be ellipsoid. ω_1 or ω_2 are both functions of the aspect ratio. The absolute of ω_1 and ω_2 increases with the increase of aspect ratio, which means the degree of anisotropy increases. For Sand O, the aspect ratio of the particles is close to 1 and the degree of anisotropy follows the same trend with the ideal particle/void system. For the Lentils, however, the values of ω_1 and ω_2 deviate from ideal particle/void systems.

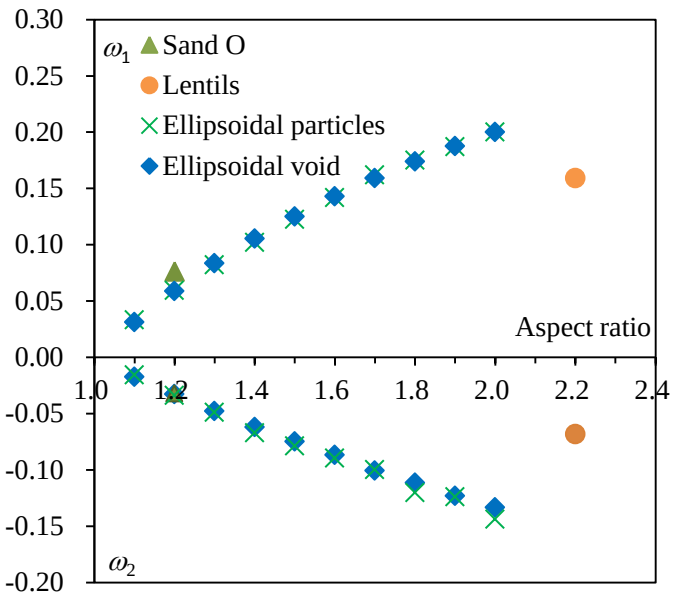

Fig. 5.6 ω_1 and ω_2 of different particle/void system

Fig. 5.7 presents the correlation between ω_1 and ω_2 for all cases examined. It shows that the relation between ω_1 and ω_2 is almost linear. For ideal particle/void system, the ratio of ω_2 to ω_1 is about -0.63~-0.66. While for Sand O and Lentils, the ratio is about -0.42~-0.43. From the statistical point of view, -0.5 is a reasonable estimate of the relation between the two quantities, i.e., ω_2=-0.5ω_1. which justifies the analytical relation in Eq.(5.50).

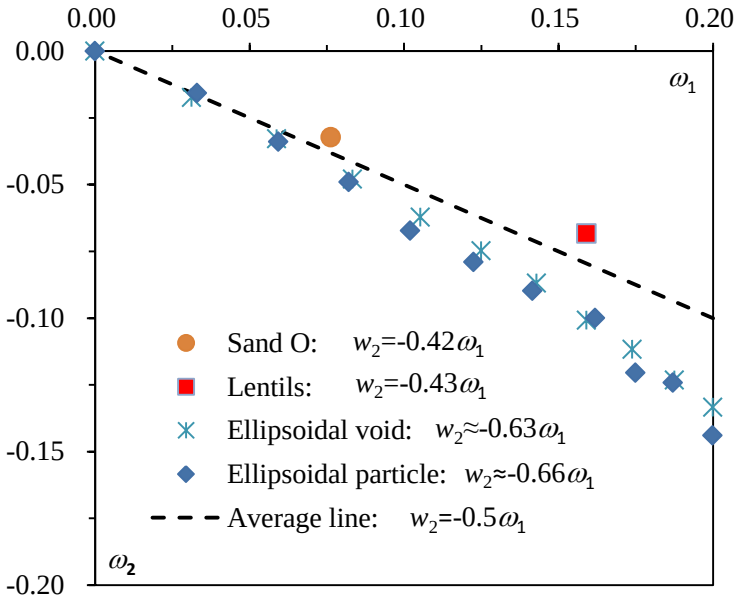

Fig. 5.7 The correlation between ω_1 and ω_2

5.3.3 Permeability anisotropy ratio

The permeability equation in Guo (2012) neglects the directional variation of pore size perpendicular to the flow direction:

$$k_{ij} = \frac{\phi \bar{\Delta}_\alpha^2}{C_\alpha} \alpha_{il}^{-1} T_{lj}^* \tag{5.51}$$

with $\alpha_{ij} = (2\delta_{ij} + T_{ij}^*)/3$. The tortuosity tensor $T_{ij}^* = \phi\left(\frac{2}{5} D_{ij} + \delta_{ij}\right)$ is related to the fabric tensor defined by the Mean Intercept Length:

$$T_{ij}^* = \frac{\phi}{5}(2F_{ij}^{MIL} + 3\delta_{ij}) \tag{5.52}$$

Eq.(5.37), however, takes into account the effect of directional variation of both *MIL* and *APS*. This section explores the importance of *APS* in the determination of permeability by

examining the permeability anisotropy ratio.

Using Eq.(5.51), the permeability anisotropy ratio defined as the permeability in the bedding plane (*x*-O-*y*) to the permeability normal to the bedding plane (*z*-direction) can be calculated as:

$$r_k^G = \frac{k_h}{k_v} = -\frac{(2\omega_1+5)(5\phi-4\phi\omega_1+10)}{(4\omega_1-5)(5\phi+2\phi\omega_1+10)} \tag{5.53}$$

substituting Eq.(5.44) and Eq.(5.45) into Eq.(5.37) yields the permeability ratio as:

$$\begin{aligned} r_k &= \frac{k_h}{k_v} = -\frac{(\omega_1+1)(\omega_2+1)}{(2\omega_1-1)(2\omega_2-1)} \frac{(2\omega_1+5)(5\phi-4\phi\omega_1+10)}{(4\omega_1-5)(5\phi+2\phi\omega_1+10)} \\ &= \frac{(\omega_1+1)(\omega_2+1)}{(2\omega_1-1)(2\omega_2-1)} r_k^G \end{aligned} \tag{5.54}$$

Based on the correlation between ω_1 and ω_2, the degree of anisotropy in Eq.(5.54) can be rewritten as

$$r_k = \frac{k_h}{k_v} = \frac{(\omega_1+1)(\omega_2+1)}{(2\omega_1-1)(2\omega_2-1)} r_k^G = \frac{0.5\omega_1-1}{2\omega_1-1} r_k^G \tag{5.55}$$

According to Eq.(5.53) and Eq.(5.54), the permeability anisotropy ratio is a function of the volumetric porosity and the fabric of the medium. The predicted hydraulic conductivity anisotropy ratio by these two models is presented in Fig. 5.8. In general, the permeability anisotropy ratio decreases with the increase of porosity. However, when the material anisotropy is weak (smaller ω_1), the decrease is insignificant. For a given porosity, the permeability ratio considering both F_{ij}^{MIL} and F_{ij}^{APS} is higher than that predicted by the equation in Guo (2012). Actually, from Fig. 5.7, it can be seen that

ω_1=0.16 corresponds to Lentils. In Fig. 5.8, at ϕ=0.347 which also corresponds to Lentils, the permeability anisotropy ratio predicted by the equation in Guo (2012) is 1.2 while that predicted in this study is about 1.6. Experimental results in Chapter 3 shows that the permeability anisotropy ratio for Lentils is 1.28~1.78, demonstrating that the model proposed in this study is more reliable by taking into account pore sizes in both flow direction and the direction perpendicular to flow direction.

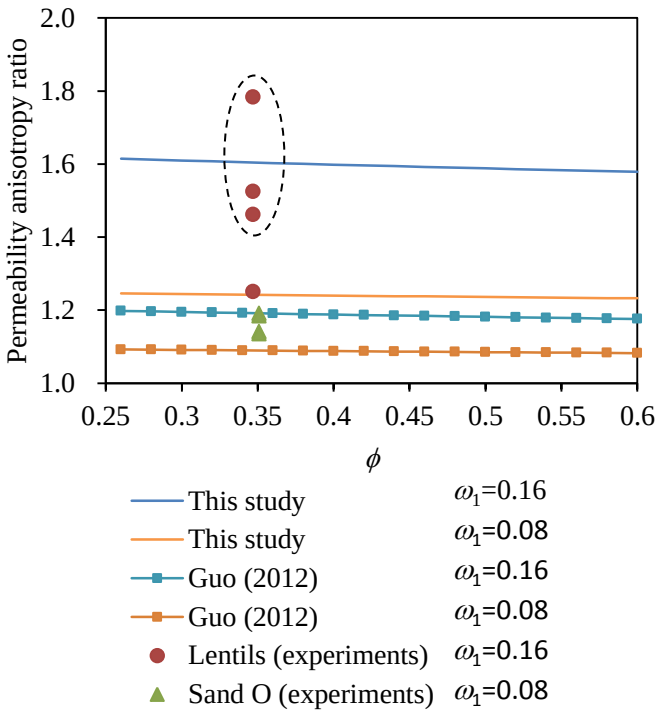

Fig. 5.8 The variation of permeability anisotropy with different porosity

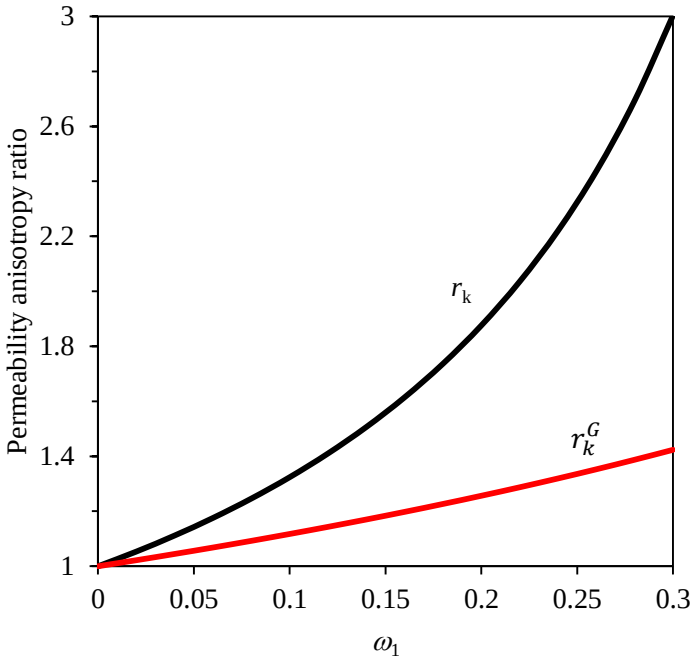

Fig. 5.9 The variation of permeability anisotropy ratio with the anisotropy of the fabric

Refer to Fig. 5.9, with the increase of material fabric anisotropy (increase of ω_1), the predicted permeability anisotropy both increase. However, the permeability anisotropy ratio predicted by the model neglecting the pore size perpendicular to the flow direction (denoted as r_k^G) is lower than that by the model considering pore size in both directions (denoted as r_k). When ω_1 reaches 0.3, the aspect ratio of particle/void is almost 3 (see Fig. 5.6), and r_k^G is about 1.4, while r_k can reach as high as 3.0. According to the data reported in the literature, e.g., Chapuis and Gill 1989 (more details can be found in Section 2.2, Chapter 2), the permeability anisotropy ratios of the materials having similar aspect ratios are in the range of 2.0~2.5. It again justifies that neglecting the pore size perpendicular to the flow direction tends to underestimate the permeability anisotropy

ratio.

5.4 Simplified approach

The micromechanical model proposed in this chapter employs two different tensorial measures of fabric, i.e., Mean Intercept Length and Areal Pore Size. For the sake of simplicity and easy application, it might be useful to provide an alternative, relatively simple, framework that incorporates a priori assumption of coaxiality between the principal directions of fabric and those of hydraulic conductivity.

(*i*) *Spectral decomposition of hydraulic conductivity tensor*

As discussed in Section 3.3.2, Chapter 3, the hydraulic conductivity K could be represented by a second order tensor. Assuming that its eigenvectors are coaxial with the material directions, the general representation of this operator takes the form:

$$K_{ij} = K_1 e_i^{(1)} e_j^{(1)} + K_2 e_i^{(2)} e_j^{(2)} + K_3 e_i^{(3)} e_j^{(3)} \qquad (5.56)$$

where e_i^{α} $(\alpha = 1,2,3)$ specifies the principal direction, while K_α define the eigenvalues. It should be noted that both materials tested in this study (i.e., Sand O and Lentils) display a transverse isotropy; so that if $e_i^{(1)}$ is the preferred orientation then K_2=K_3. Also, it needs to be emphasized that for porous media both fabric descriptors, i.e., Mean Intercept Length and Areal Pore Size, have virtually the same eigenvectors (Inglis and Pietruszczak, 2003).

The spectral decomposition Eq.(5.56) requires the specification of K_α, which can

be identified by performing standard permeability tests on samples oriented along the principal material axes. In case of induced anisotropy, an appropriate evolution law needs to be formulated that relates the evolution of principal axes of fabric to those of the strain tensor.

(*ii*) *Alternative representation* (*Cayley-Hamilton theorem*)

Another simple way of defining the permeability tensor k_{ij} is to assume

$$k_{ij} = c_1 F_{ij} + c_2 F_{ip} F_{pj} + ... \tag{5.57}$$

where c's are constants and F_{ij} is the second order tensor. Note that the above representation also implies the coaxiality of both tensors. When selecting F_{ij} as the fabric tensor and omitting the higher order product of fabric tensor, Eq.(5.57) is simplified as:

$$k_{ij} = c_1 F_{ij} \tag{5.58}$$

where c_1 may be estimated from basic micromechanical considerations. Adopting, for example, Kozeny-Carman equation,i.e., Eq.(5.41) and employing MIL, i.e., F_{ij}^{MIL}, as a measure of microstructure, one can write

$$k_{ij} = \frac{\phi \bar{\Delta}_\alpha^2}{C_\alpha \tau^2} F_{ij}^{MIL} \tag{5.59}$$

where the tortuosity factor may be estimated as $\tau = \phi^{-p}$ with p=0.4 (see Section 5.3.1). Thus, the hydraulic conductivity tensor is defined as

$$K_{ij} = \frac{\rho g}{\mu} \frac{\phi \bar{\Delta}_\alpha^2}{C_\alpha \tau^2} F_{ij}^{MIL} \tag{5.60}$$

The performance of this equation will be examined in next section.

5.5 Analytical results and comparison with experiments

5.5.1 Micromechanical model

Assume the cross section of pores are circle in shape, the shape factor can be selected as $C_\alpha = 2.0$. Note that the hydraulic conductivity of a certain fluid flowing through a medium is defined as $K_{ij} = \frac{\rho g}{\mu} k_{ij}$ where ρ and μ is the density and dynamic viscosity of the fluid and g is the acceleration due to gravity.

Table 5.1 Physical properties of the porous medium and the fluid

Materials	ϕ	Δ_α (mm)	Fluid	μ (Pa s)	ρ (kg/m^3)
Sand O	0.351 ± 0.002	0.024	Water	0.001	1000
Lentils	0.347 ± 0.002	0.285	Mineral oil	0.098	865

The properties of the materials are listed in Table 5.1. The fabric tensors of the corresponding medium can be found in Section 4.5, Chapter 4. Substituting all the parameters into Eq.(5.37), the hydraulic conductivity tensors and the anisotropy ratio of these two series of tests are predicted as:

Sand O $$K_{ij} = \begin{bmatrix} 0.48 & -0.00 & 0.00 \\ -0.00 & 0.48 & 0.00 \\ 0.00 & 0.00 & 0.38 \end{bmatrix} \text{ mm/s } r=1.26 \quad (5.61)$$

Lentils $$K_{ij} = \begin{bmatrix} 0.62 & -0.01 & 0.00 \\ -0.01 & 0.60 & -0.00 \\ 0.00 & -0.00 & 0.38 \end{bmatrix} \text{ mm/s } r=1.65 \quad (5.62)$$

where r is the anisotropic ratio defined as the ratio of the maximum to the minimum eigenvalues of the hydraulic conductivity tensors.

Both of the hydraulic conductivity tensors show cross-anisotropic features. The axis of symmetry is in z-direction, which is perpendicular to the bedding plane. The off-diagonal values of the hydraulic conductivity tensors are close to zero, which means that the principal directions of the hydraulic conductivity tensors are in x, y and z-directions. Refer to the fabric tensors of the materials in Subsection 4.5.2, the principal directions of the fabric tensors are also in x, y and z-directions, showing that the hydraulic conductivity tensors are coaxial with the principal directions of the internal structure.

The permeability test results for the two materials examined from Chapter 3 are presented again in Table 5.2. The predicted hydraulic anisotropic ratio (k_h/k_v =1.26) of Sand O is slightly higher than that of the laboratory tests k_h/k_v = 1.13-1.19. The predicted anisotropic ratio of Lentils (k_h/k_v = 1.65) is right in the range of the experimental results (k_h/k_v = 1.25-1.78).

Table 5.2 Permeability test results on Sand O and Lentils

Material	k_h (mm/s)	k_v (mm/s)	k_h/k_v
Sand O	0.543±0.001	0.467±0.010	1.13-1.19
Lentils	0.598±0.059	0.400±0.031	1.25-1.78

The predicted hydraulic conductivity of Sand O in the bedding plane (*x*-*y* plane) and the normal of bedding plane is 0.48mm/s and 0.38mm/s respectively. Compared to the experimental results 0.543 and 0.467 in these two directions, the analytical result is rather accurate. Same conclusion can be drawn for lentils as well. Good agreement is found in both directions between predicted and experimental results.

In this case, the hydraulic conductivity tensors could be simplified to 2D form which keeps only the principal values in horizontal (bedding plane) and vertical (normal of the bedding plane) directions.

Sand O
$$K_{ij} = \begin{bmatrix} K_h & 0 \\ 0 & K_v \end{bmatrix} = \begin{bmatrix} 0.48 & 0.00 \\ 0.00 & 0.38 \end{bmatrix} \text{ mm/s} \qquad (5.63)$$

Lentils
$$K_{ij} = \begin{bmatrix} K_h & 0 \\ 0 & K_v \end{bmatrix} = \begin{bmatrix} 0.61 & 0.00 \\ 0.00 & 0.38 \end{bmatrix} \text{ mm/s} \qquad (5.64)$$

Using the transformation rule in Eq.(5.56), the spectral decomposition of hydraulic conductivity tensor of the two materials are presented in Fig. 5.10.

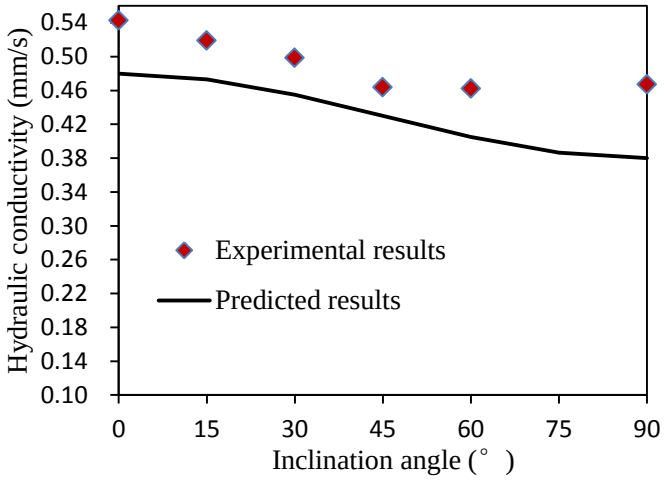

(a) Sand O (e=0.54)

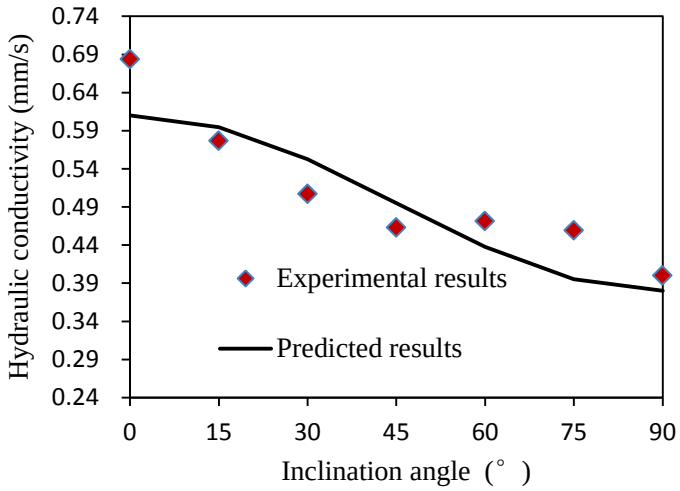

(b) Lentils Lentils (e=0.53)

Fig. 5.10 Comparison of predicted results and experimental results

5.5.2 Simplified approach

Substituting all material parameters in Table 5.1 and fabric tensors in Section 4.5, Chapter 4 into Eq.(5.60), the hydraulic conductivity tensors of the two material are predicted as:

$$\text{Sand O} \qquad K_{ij} = \begin{bmatrix} 0.47 & 0.00 & 0.00 \\ 0.00 & 0.47 & 0.00 \\ 0.00 & 0.00 & 0.37 \end{bmatrix} \text{ mm/s } r=1.27 \qquad (5.65)$$

$$\text{Lentils} \qquad K_{ij} = \begin{bmatrix} 0.62 & -0.01 & -0.00 \\ -0.01 & 0.59 & -0.00 \\ -0.00 & -0.00 & 0.37 \end{bmatrix} \text{ mm/s } r=1.70 \qquad (5.66)$$

Since they exhibit cross-anisotropic feature, they can all be simplified into 2D form:

$$\text{Sand O} \qquad K_{ij} = \begin{bmatrix} K_h & 0 \\ 0 & K_v \end{bmatrix} = \begin{bmatrix} 0.47 & 0.00 \\ 0.00 & 0.37 \end{bmatrix} \text{ mm/s} \qquad (5.67)$$

$$\text{Sand O} \qquad K_{ij} = \begin{bmatrix} K_h & 0 \\ 0 & K_v \end{bmatrix} = \begin{bmatrix} 0.61 & 0.00 \\ 0.00 & 0.37 \end{bmatrix} \text{ mm/s} \qquad (5.68)$$

Following Eq.(5.56), the spectral decomposition of the hydraulic conductivity tensor are presented in Fig. 5.11. The predicted results are in good agreement with experimental results. It follows the same trend: the hydraulic conductivity in the bedding plane is the greatest and that in the normal of the bedding plane is the lowest. The predicted permeability anisotropy ratio is also comparable for both materials.

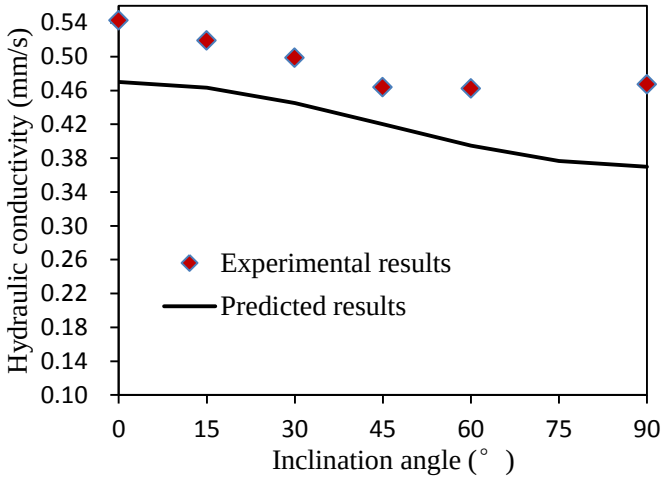

(a) Sand O (e=0.54)

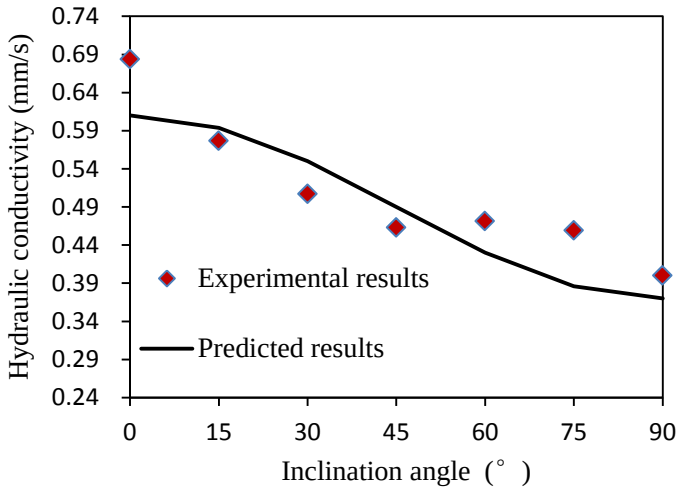

(b) Lentils Lentils (e=0.53)

Fig. 5.11 Comparison of predicted results and experimental results

5.6 Summary

In this chapter, a theoretical model is developed to describe flow in porous medium with internal structures using the technique of homogenization. With the fluid-solid interaction taking into account on the particle level, the permeability tensor of a porous

medium is derived from the macroscopic momentum balance equation of the fluid. The microstructure of the porous media is characterized by fabric tensors defined by Mean Intercept Length and Area Pore Size, which are measures for pore structures. The results obtained from the theoretical model and a simplified model is in good agreement with laboratory test data. In closing this chapter, the following remarks are made:

1) When interpreted in the classical meaning, the influence of internal structures manifest themselves as directional dependency of hydraulic diameter and the tortuosity. More specifically, the tortuosity is related to the probability a test line intersects the void on the surface of a REV to the Normalized Mean Intercept Length;

2) The variation of areal pore size (*APS*) reflects the directional dependency of hydraulic diameter. However, the fabric tensor based on *APS* can be related to that defined according to the Mean Intercept Length;

3) For isotropic materials, the proposed model well matches the Kozeny-Carman equation;

4) For porous materials with weak anisotropy, a simplified approach is proposed by assuming coaxiality between the principal directions of fabric tensor and those of hydraulic conductivity tensor. Analytical results using the proposed model are compared with that of laboratory tests. Good agreement is found in terms of hydraulic conductivity ratio as well as the hydraulic conductivity;

5) When considering the permeability tensor as a second-rank tensor, only permeability tests in principal directions and the fabric tensor are needed to determine the hydraulic conductivity tensor.

Chapter 6 Numerical simulation of fluid flow in porous media using Pipe Network Model

6.1 Introduction

As has been discussed in the literature review (Chapter 2), many numerical modelling methods require detailed internal structure data and expensive computation effort. The model construction of those methods may also over-simplify the structure to make meshing work.

In Chapter 4, it is discussed that the fabric tensor based on Mean Intercept Length is able to capture the anisotropy of a media. However, it may not be comprehensive as it only uses the average pore size as the descriptor and ignores the coefficient of variation of the pore size distribution. This may undermine some important features of granular materials under some circumstances.

It has been shown by Pietruszczak and Pande (2012) that the directional variation in permeability can be captured if the corresponding pore size distribution is given. In their work, a concept of "areal pore size" is employed. Due to the lack of experimental results, they use generated input data to calculate the hydraulic conductivity.

This chapter explores the capability of an alternative approach using the Pipe Network Model (PNM) to simulate flow in porous media. It utilizes CT scan results and

the technique of digital image analysis to obtain the information of the pore size distribution. Both the average size and the deviatoric components are considered. The model has also been modified to be applied to anisotropic materials. This methodology can be considered as a supplement of the analytical model presented in Chapter 5.

6.2 Percolation theory and Pipe network model

The model used here is similar to the cubic lattice models described by Chatzis and Dullien (1977) and Diaz et al.(1987). Detailed algorithm and explanation can be found in Kralj and Pande (1994). Only a brief description of the model is outlined here for the sake of completeness.

6.2.1 Percolation through the model

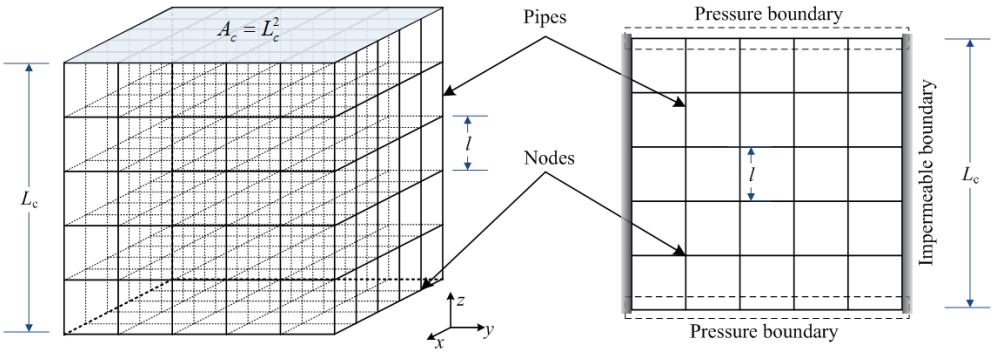

(a) 3D cubic pipe network (b) Simplified 2D network

Fig. 6.1 Illustration of typical pipe networks

A cubic lattice network is generated with nodes and capillary pipes (Fig. 6.1) to represent the pore structure. In such a cubic lattice network, a node is the point of connection of pores and a pipe represent a pore or capillary segments. The diameter of

the pipes follows lognormal distribution with the probability density function being defined as:

$$P(d) = \frac{1}{d\sigma\sqrt{2\pi}} e^{\frac{-(\ln(d-d_{mean})}{2\sigma^2}} \tag{6.1}$$

where $P(d)$ is the probability density when the pipe diameter is d; d_{mean} is the mean diameter of all pipes; and σ is the standard deviation. Another parameter that is used more often is the Coefficient of Variation (c_v) defined as $c_v = \sigma / d_{mean}$.

Fig. 6.2 shows examples of different pipe diameter distributions with same Mean Diameter (d_{mean}) but different Coefficients of Variation (c_v). Even though the mean values of the pipe diameter are the same, the distribution could be rather different depending on the value of c_v.

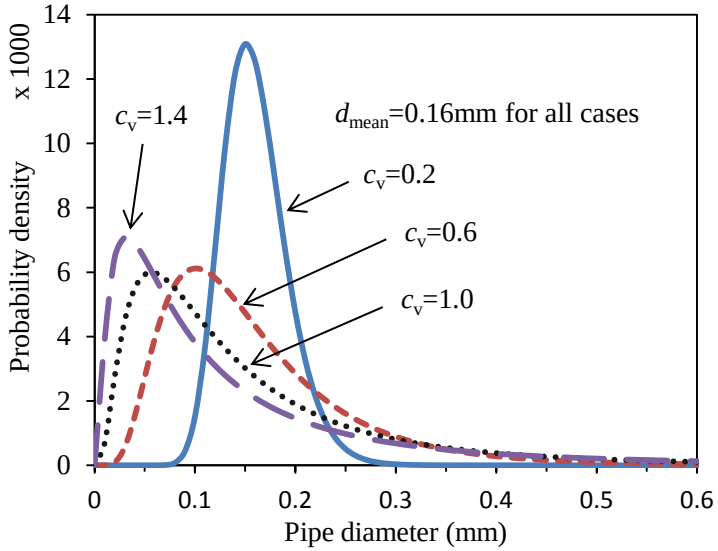

Fig. 6.2 Illustration of probability density distributions of pipe diameters with the same Mean Diameter d_{mean}=1.6×10^{-4}m but different Coefficients of Variation

When constructing the pipe network, pipe diameters following lognormal distribution are generated and assigned randomly to the pipe segments connecting nodes in a pipe network. The pipe length is then calculated based on the overall porosity of the actual porous medium. When modelling flow in the pipe network, all pipes are assumed to be open and empty before percolation starts. The opposite two faces of the cubic are chosen as inlet and outlet boundaries on which constant pressures are applied. The other four faces parallel to the direction of hydraulic gradient are considered as impermeable boundary to simulate flow in a single direction.

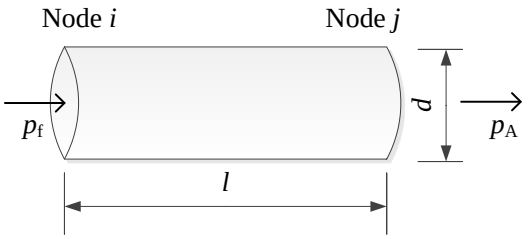

Fig. 6.3 Illustration of a single pipe

Percolation through the network is calculated in a manner of iterations. In each iteration, the pipe connected to a node may or may not be penetrated by fluid depending on its diameter and the pressure difference. The minimum diameter of a capillary tube that is filled by percolating fluid under a certain pressure difference is determined by Washburn (1921) equation

$$p_c = p_f - p_A = \frac{4T\cos\theta}{d} \tag{6.2}$$

where p_c is the capillary pressure, p_f is the fluid pressure at the node filled with fluid (water),

p_A is the air pressure at an empty node (air), T is the surface tension of the pore fluid, θ is the contact angle of the fluid with the pipe and d is the pipe diameter.

After identifying all capillary pipes that are invaded by fluid in a particular iteration, the pressure drop through a single pipe (as shown in Fig. 6.3) can be calculated based on the Hagen-Poiseuille equation (Sutera and Skalak, 1993):

$$\Delta H = \frac{128\mu l Q}{\gamma \pi d^4} \tag{6.3}$$

where ΔH is the head loss along the pipe, μ is the viscosity of the fluid, l is the length of the pipe, Q is the flow rate through the pipe and γ is the unit weight of fluid.

Equilibrium is approached when the overall flow rate, Q_c, becomes a constant, and the process of iteration can stop. The overall hydraulic conductivity can be computed based on Darcy's law as:

$$K = \frac{Q_c L_c}{A_c \Delta H_c} \tag{6.4}$$

where A_c is the cross section area of the cubic normal to the flow direction, L_c is the length of the cubic along the flow direction as shown in Fig. 6.1 and ΔH_c is the head loss across the entire cubic.

A program "*PERMIA*" has been previously developed in the Department of Civil Engineering, University of Wales, Swansea, to evaluate the permeability of porous media such as soil and rock (Kralj and Pande, 1994). In this study, *PERMIA* is modified to

simulate flow in anisotropic materials, based on the pore size distribution data obtained by Micro-CT scan and digital image analysis.

6.2.2 Parametric study

The Pipe Network Model requires the following set of input parameters: Overall porosity ϕ of the specimen, mean diameter of all pipes d_{mean}, the coefficient of variation c_v of the pipe diameters, the number of pipes along each side of the cubic lattice NP, head difference ΔH_c across the specimen, surface tension, density and dynamic viscosity of the permeating fluid T, ρ and μ, as well as the contact angle θ between the fluid and the solid phase. The influence of the parameters on the performance of the pipe network model and the calculation of permeability will be investigated. The focus will be placed on improved understanding of the internal pore structure on the permeability of granular materials.

6.2.2.1 Mean diameter and variation of the percolating pipes

A series of simulations are performed with varying mean diameters and coefficients of variation. The mean diameter changes from 0.1mm to 0.2mm and the coefficient of variation ranges from 0.1 to 1.5. The other parameters to define the pipe network are listed in Table 6.1.

Fig. 6.4 presents the variation of hydraulic conductivity obtained from simulations with different mean pipe diameters and coefficients of variation. The pipe diameter

distributions of four of those simulations can be seen in Fig. 6.2. The hydraulic conductivity increases with the increase of mean diameter which reflects the average pore size. However, the mean diameter or the average pore size cannot uniquely determine the hydraulic conductivity which also depends on the coefficient of variation of pipe diameter. The Mean Diameters of these four cases are all 0.16mm. For example, when d_{mean}=0.16mm, the hydraulic conductivity at c_v=0.2 is 6 times higher than that when c_v=1.4. Referring to Fig. 6.2, for the same mean diameter of 0.16mm, the pipe diameters in the case of c_v=1.4 vary over a relatively large range with more pipes of smaller diameter. In reality, if an interconnected network has more smaller pipes, it becomes harder for the fluid to permeate through. This again confirms that the average value of the pore size is not enough to evaluate the hydraulic conductivity of porous media. The coefficient of variation is also important.

Table 6.1 Input parameters

ϕ	NP	l (mm)	L_c (mm)	θ (°)	μ (Pa s)	ρ (kg/m^3)	T (N/s)
0.351	11	0.57	6.27	27	0.001	1000	7.29E-02

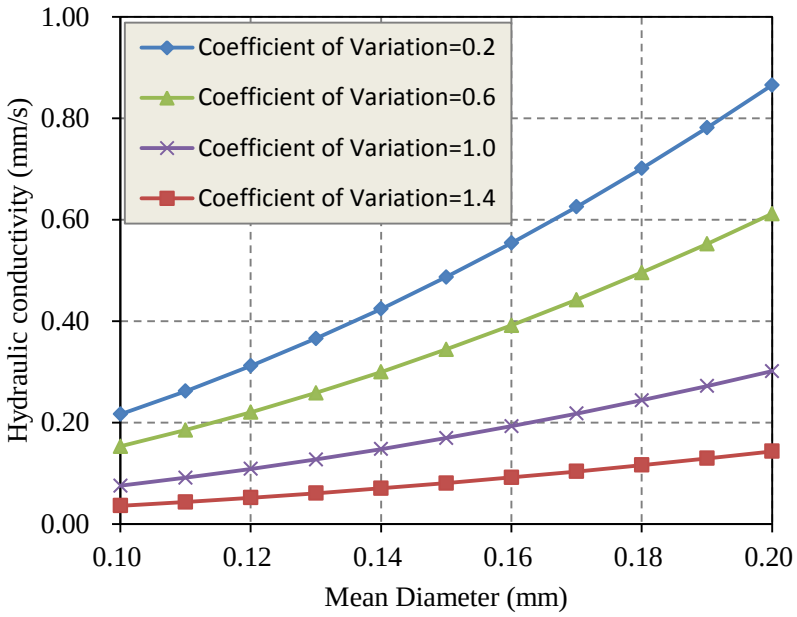

Fig. 6.4 The variation of hydraulic conductivity Vs. mean diameter with different coefficient of variation (c_v)

6.2.2.2 Applied head difference on the model

According to Darcy's Law, for laminar flow in a fully saturated porous material, the hydraulic conductivity should be independent of the applied pressure head difference. In this study, however, the pressure difference tends to affect the percentage of the percolated pores, which leads to different degrees of saturation (S_r). The degree of saturation in turn affects the calculation of hydraulic conductivity. To illustrate this phenomenon, a series of simulations using different pressure head differences were carried out, using the model parameters listed in Table 6.2.

Table 6.2 Input parameters

ϕ	d_{mean} (mm)	c_v	NP	l (mm)	L_c (mm)	θ (°)	μ (Pa s)	ρ (kg/m^3)	T (N/s)
0.351	0.160	0.5752	11	0.57	6.27	27	0.001	1000	7.29E-02

The ultimate degree of saturation when steady flow is achieved is plotted against the applied pressure head difference in Fig. 6.5. As can be seen, with the increase of pressure head, the degree of saturation goes up and approaches a constant value. This can be explained by the mechanism of percolation theory. When the pressure difference is low, only bigger voids are invaded. With the increase of the pressure head difference, more pores with smaller diameters become accessible to the fluid. The degree of saturation increases accordingly.

Fig. 6.5 presents the hydraulic conductivity at different level of degree of saturation at the steady state. When the degree of saturation is low, the hydraulic conductivity is very low. With the increase of degree of saturation, more voids are occupied by fluid, while the hydraulic conductivity increases and approaches a constant value eventually. When S_r approaches 100%, the required pressure head difference has gone higher than 10m (see Fig. 6.5), which is unlikely to happen in a real laboratory permeability test.

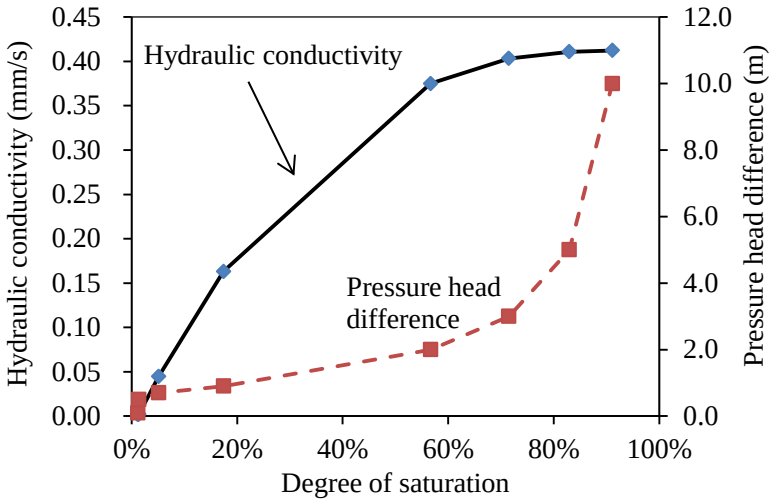

Fig. 6.5 The influence of pressure head difference on the degree of saturation

It should be noted that the flow processes as described by the pipe network model based on the percolation theory are different from the standard laboratory permeability tests. In standard permeability tests, the sample must be first saturated by a vacuum (ASTM 2006) at a pressure of -50 ~ -60kPa. At the same time, water is allowed to flow slowly through the sample to help remove trapped air bubbles. The hydraulic conductivity is then measured under saturated conditions. In other words, the results only reflect flow under fully saturated conditions. The percolation theory, on the other hand, mimics a different process. Starting at dry state, and gradually increasing fluid pressure and pressure difference, it allows the fluid to invade bigger voids first under a certain level of pressure difference. With the increase of the pressure/pressure difference, smaller voids are filled by water and hence the degree of saturation increases. In other word, this method takes into account the effect of trapped air bubbles in the voids between particles. Higher pressure is

needed to obtain higher degree of saturation.

In real granular materials, a high pressure difference may cause turbulent flow or piping. Since laminar flow is a premise in pipe network model, the Reynolds number in every simulation is checked using:

$$R_n = \frac{\rho v d}{\mu} \tag{6.5}$$

where v is the velocity of fluid flow, d is the pipe diameter, and μ and ρ are the dynamic viscosity and density of water, respectively. The maximum Reynolds number in all simulations is 0.07, which satisfies the requirement of laminar flow (Das, 1983).

6.2.2.3 Intrinsic permeability of porous media

One interesting fact about Pipe Network Model is that it is capable of computing the intrinsic permeability that is solely a function of the pore structure. To this end, more simulations were carried out using two other fluids, one with high dynamic viscosity (motor oil) and the other having high contact angle (mercury). The properties of the permeating media are the same as those in Table 6.2. The properties of these two fluids and water are listed in Table 6.3.

Table 6.3 Properties of permeating fluids

Fluid	θ (°)	μ (Pa s)	ρ (kg/m^3)	T (N/s)
Mercury	130	1.526e-3	13534	0.48650
Motor oil	70	0.250	899	0.03100
Water	27	0.001	1000	0.07288

A series of simulations were performed under different pressure head difference using each fluid. The permeability of each simulation was calculated by

$$k = K\frac{\mu}{\rho g} \tag{6.6}$$

where k is the intrinsic permeability of a percolating media, K is the hydraulic conductivity, ρ is the density of the fluid and g is acceleration due to gravity.

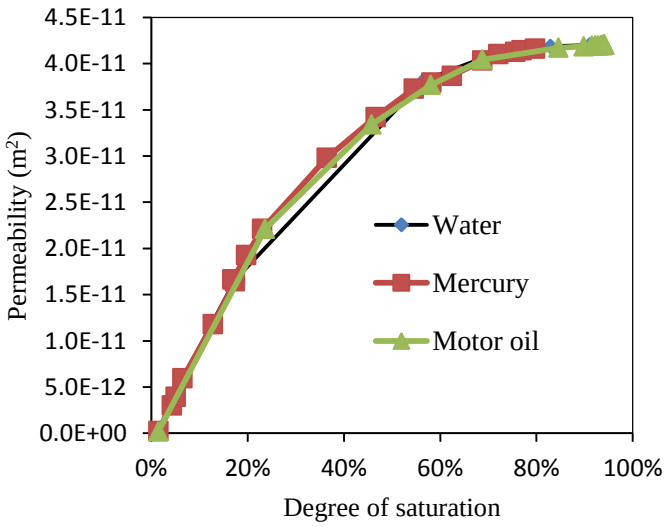

Fig. 6.6 Permeability results using different fluids (d_0=0.16mm, c_v=0.5752)

Fig. 6.6 presents the variation of permeability of the material with the degree of saturation using different fluids. As can be seen in Fig. 6.6 the intrinsic permeability values under different degree of saturation are independent of the fluid, confirming that the permeability is uniquely determined by the pore structure of the media.

6.2.2.4 Pipe network model for anisotropic distribution of pore size

In the pipe network model simulations presented previously, pipe diameters are

generated following a lognormal distribution and assigned to pipes randomly. In other words, this distribution is direction independent, corresponding to isotropic pore structures. In reality, however, the pore size distribution may vary in different directions, as discussed in Chapter 4. Fig. 6.7 shows the images of two sections in a specimen made of Eaton Lentils (Chapter 3). It can be seen that the displayed "particles" in the vertical section are more like lenticular and that in horizontal section are more circular in shape. Although not very straightforward, the pore size distributions in the vertical and horizontal sections are different.

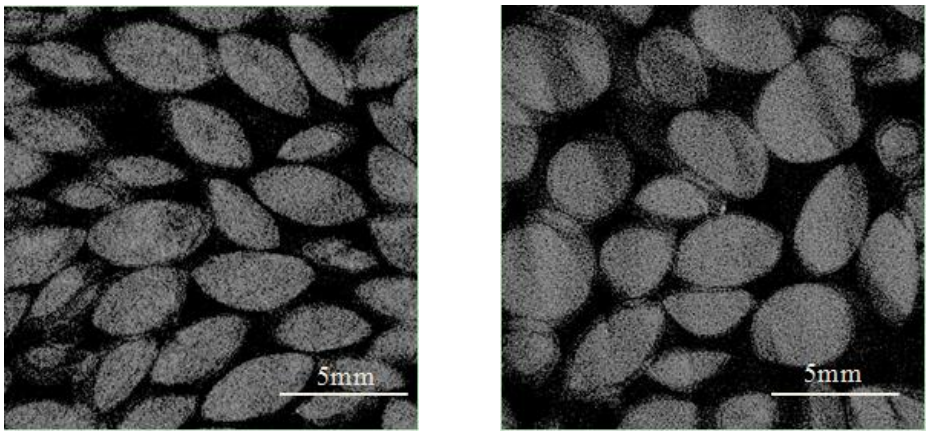

(a) Vertical section (b) Horizontal section

Fig. 6.7 Micro-CT section image of Lentils in different directions; (a) Vertical section: section in the direction of deposition; (b) Horizontal section: section in bedding plane.

In order to capture the anisotropic pore distribution and the corresponding permeability anisotropy, the pipe network model is modified to reflect the direction variation of pore size and hence the pipe diameters. In the modified algorithm, pipes in different directions follow different distributions. Refer to Fig. 6.1, three lognormal

distributions are generated and assigned to the pipes in *x*, *y* and *z* directions separately. The overall porosity of the model must be the same as that of the specimen. The mean diameter and coefficient of variation in the *x*, *y* and *z* directions are denoted as: (d^x_{mean}, c^x_v), (d^y_{mean}, c^y_v) and (d^z_{mean}, c^z_v), respectively. The following simulations use the same material properties in Table 6.1, while the mean pipe diameter and the coefficient of variation in each direction are summarized in Table 6.4. Fluid flow in each direction is simulated and the corresponding hydraulic conductivity is obtained. Table 6.4 summarizes the hydraulic conductivity for flow in different directions with various d_{mean} and c_{v}.

Table 6.4 Application of the modified algorithm to anisotropic materials

Case #	d^x_{mean} (mm)	c^x_v	d^y_{mean} (mm)	c^y_v	d^z_{mean} (mm)	c^z_v	K_x (mm/s)	K_y (mm/s)	K_z (mm/s)
1	0.160	0.5	0.160	0.5	0.160	0.5	0.708	0.708	0.708
2	0.080	0.5	0.160	0.5	0.160	0.5	0.118	0.713	0.714
3	0.160	0.5	0.160	0.5	0.160	1.0	0.536	0.535	0.477
4	0.080	0.5	0.120	0.5	0.160	0.5	0.128	0.370	0.741
5	0.160	0.5	0.160	1.0	0.160	1.5	0.317	0.276	0.243

Note: 1: isotropic; 2~3: cross anisotropic; 4~5: orthotropic

In Case 1, the pore size distribution is isotropic, which yields identical hydraulic conductivity in all directions. The materials in Cases 2 and 3 are cross anisotropic such that the pore size distributions in two orthogonal directions are identical while in the third direction is different. The varying parameter of the in Case 2 and Case 3 are the mean diameter and the coefficient of variation, respectively. In Case 2, the axis of symmetry is

x-direction and the mean pipe diameter in this direction is smaller than that of the other two directions. The values of c_v in all three directions are identical. As a result, the hydraulic conductivity for flow in *x*-direction is smaller than that in the other two directions. In Case 3, the axis of symmetry is in *z*-direction and the coefficient of variation in this direction is greater than that in the other two directions. Even though the mean pipe diameter is identical in all three directions, the larger c_v value in *z*-direction results in smaller hydraulic conductivity K_z than K_x and K_y.

The fourth and fifth cases are orthotropic materials. For Case 4, the mean diameters in *x*, *y* and *z*-directions are ranked as $d_{mean}^{x} < d_{mean}^{y} < d_{mean}^{z}$ while the coefficient of variation keeps the same. The results show different hydraulic conductivity in three directions, with $K_x<K_y<K_z$. On the other hand, for the same mean pipe diameter, hydraulic conductivity decreases with the increase of coefficients of variation in any direction, as can be observed from Case 5. These observations are consistent with the conclusions drawn in Subsection 6.2.2.1.

The calculated hydraulic conductivity for flow in anisotropic pipe network shows that as long as appropriate pore size distribution is attributed to different directions, the model is able to capture the anisotropic hydraulic conductivity properties. Consequently, the success of using a PNM to determine permeability depends on the proper characterization of pore size distributions.

6.3 Determination of pore size distribution

Different from the method used in Chapter 4, PNM requires the distribution of the pore size, including the mean and the coefficient of variation. Therefore, the fabric descriptors of Mean Intercept Length and Areal Pore Size are not sufficient for the PNM. Traditional method of determining pore size distribution, e.g., Mercury Intrusion Test, is usually destructive and may raise the concern of poison issue. In this section, a method based on the technique of image analysis is utilized to compute the pore size distribution of the granular materials.

6.3.1 Computation algorithm

The binarized micro-CT images obtained in Section 4.5, e.g., Fig. 6.9(a), is used to determine the pore size distribution. A Matlab script was developed to implement the analysis automatically.

Fig. 6.8 illustrates a simple example to determine the pore size among particles. The black ellipses in Fig. 6.8(a) are the solid phase and the rest is the void. If the void space is assumed as interconnected pipes, the pore size can be viewed as the distance between the centerline of the pipe and the surface of the surrounding particles as illustrated in Fig. 6.8. To determine the pore size, the distance between every void pixel and its closest solid pixel is computed using the Matlab built-in function *bwdist*(). This distance value of

every pixel is next used as gray-scale value and presented in Fig. 6.8(b) as a Distance Transformation Map (DTM). The grayscale value for display has been equalized to 0~255 for better visualization, but the original values remain unchanged.

We next find out which part of DTM should be used to represent the centerline of the void space. This study employs the concept of watershed segmentation, originally developed for the separation of terrains in hydrological applications (Beucher and Lantuejoul, 1979). The original idea of the watershed segmentation is to find out the ridgeline of the terrains on which the rain droplets have equal probability to flow to either side of the line. The local minimum altitude is defined as the catchment basin. In this study, the distance is used as the altitude of the terrain and the solid pixels are the catchment basin. Another Matlab built-in function *watershed*() is utilized to find out the "ridge line" of the terrain. By applying the watershed segmentation algorithm, the ridgeline is obtained as the "axis" line of a pipe in the pore network. Finally, the grayscale values (distance) of pixels on DTM along ridgelines are selected as the pipe radius and statistical data are derived.

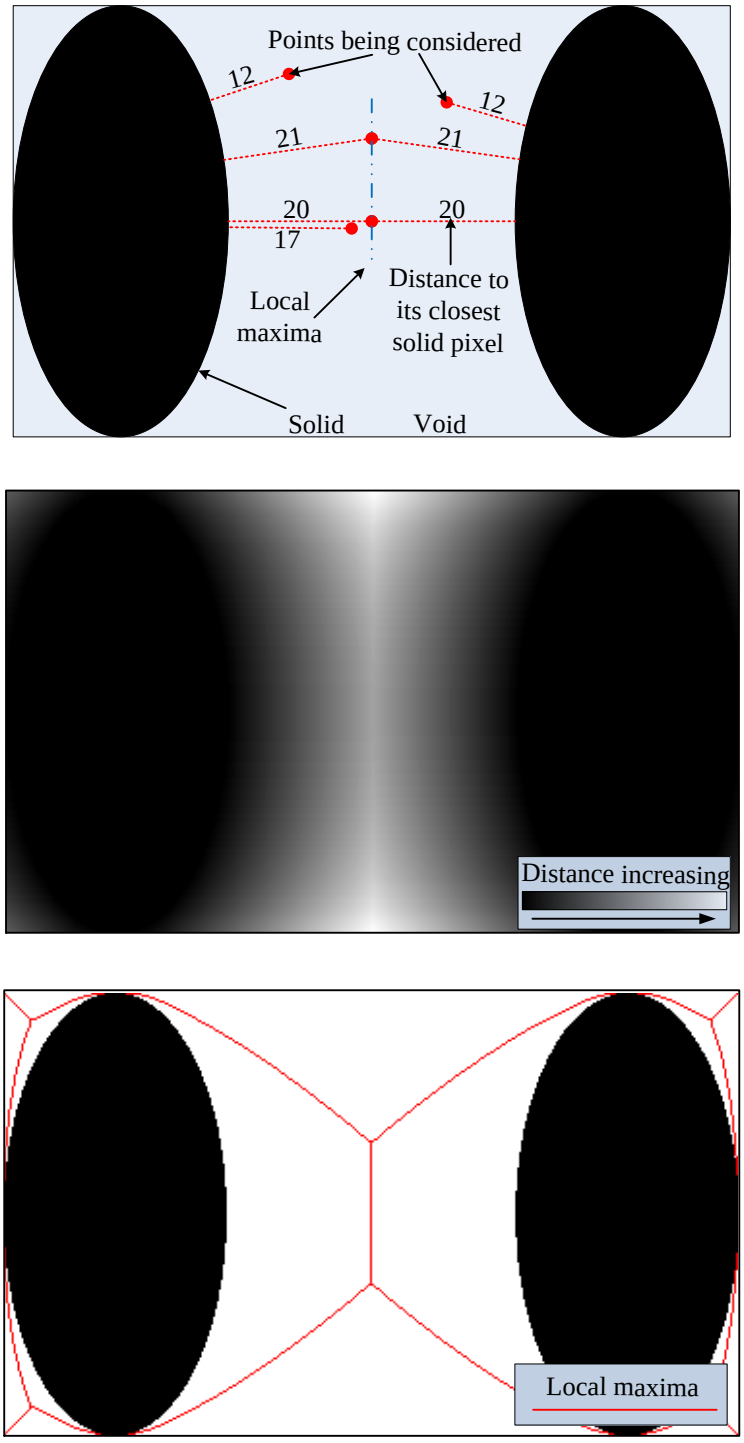

Fig. 6.8 Illustration of the algorithm calculating the pore size distribution; (a) compute the distance between every pixel to its closet solid pixel and find out the local maxima of the distance; (b) Distance Transformation Map obtained from step (a); (c) centerline (local maxima) of pipes superimposed on the binary image.

6.3.2 Pore size distribution of investigated materials

The algorithm developed in the previous section is used to determine the pore size distribution of specimens discussed in Chapter 3. Fig. 6.9 shows an example of the application of this algorithm. Fig. 6.9 (a) is the original μCT image obtained from Sand O and (b) is the filtered image. This pre-processing algorithm has been discussed in Section 4.5. Fig. 6.9(c) is the binarized image and (d) is the Distance Transformation Map. Fig. 6.9 (e) illustrates the ridgeline superimposed on the binary image. Fig. 6.9 (f) gives the statistical results of an image. The abscissa axis represents the pore radius in pixels and the ordinate axis represents the number of a specific radius value. With the resolution being 26.3μm/pixel, the mean diameter and the coefficient of variation can be computed as 1.77×10^{-4}m and 0.5662, respectively.

Table 6.5 summarizes the pore size distribution of the specimens investigated in this study by using Micro-CT scan and the technique of image analysis. These data will be used as input in the PNM simulations in later sections. The pore size distributions of Sand O and Lentils in different directions are also presented in Fig. 6.10.

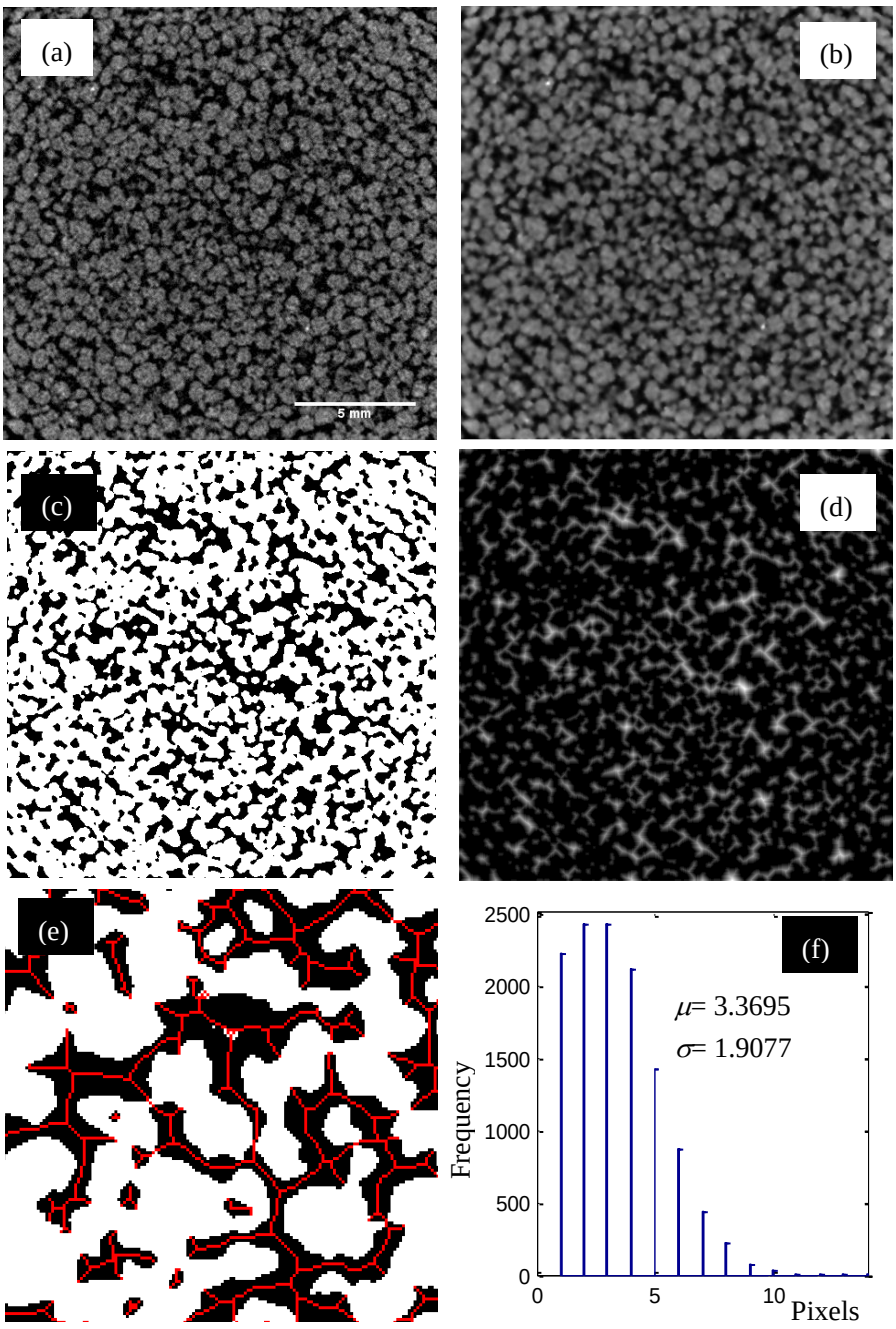

Fig. 6.9 Application of the developed code on images obtained from Sand O; (a) the original grayscale bitmap of Sand O; (b) filtered image; (c) binarized image; (d) distance transformation map (DTM); (e) ridge lines superimposed on the binary image (zoomed in); (f) histogram of the pore size distribution (pipe radius in pixel).

Table 6.5 Pore size distribution of all investigated specimens

Materials	Classification	ϕ	Direction	d_{mean} (mm)	c_v
Sand O	Isotropic	0.351	All	0.160	0.5752
Sand L	Isotropic	0.397	All	0.114	0.6240
Sand O	Anisotropic	0.362	Horizontal	0.175	0.5621
			Vertical	0.158	0.5555
Lentils	Anisotropic	0.355	Horizontal	1.020	0.5322
			Vertical	0.827	0.5100

Note: Horizontal means the plane is normal to the deposition direction and Vertical means the plane is in the direction of deposition

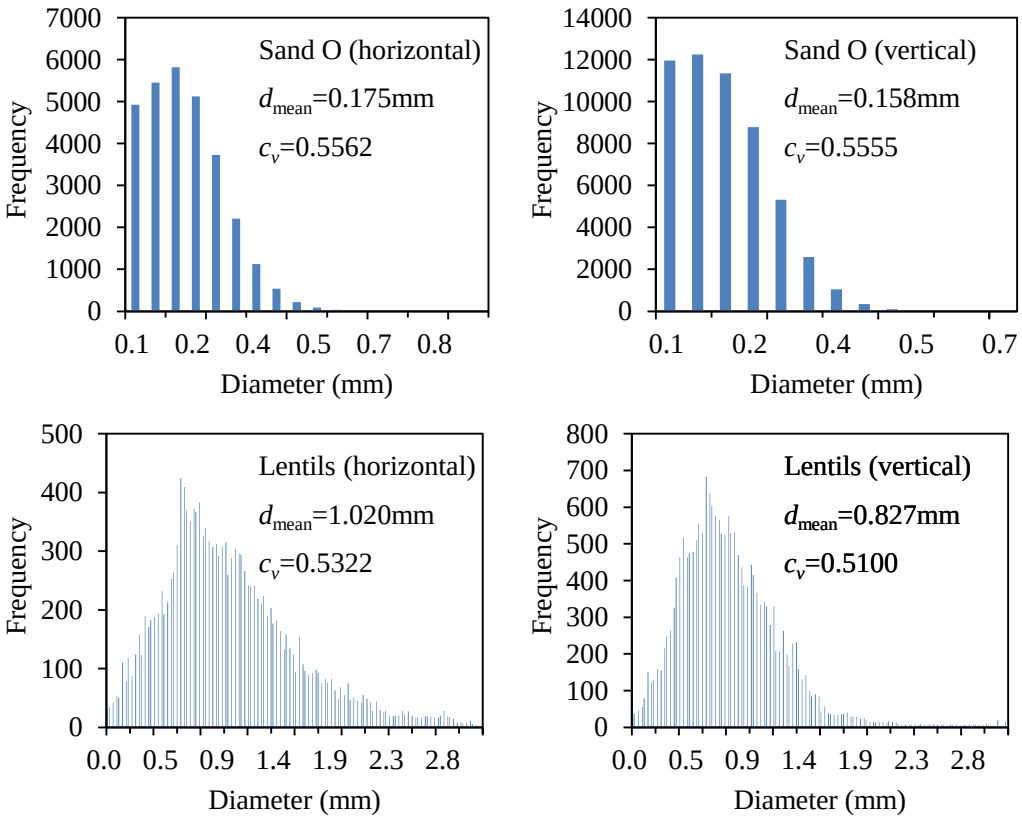

Fig. 6.10 Pore size distributions of anisotropic materials

6.4 Verification and discussions

A total number of 4 specimens are studied using the methodology proposed in this

chapter. The experimental permeability tests have been performed on specimens made of different materials and the results have been presented in Chapter 3. Separate specimens with very close porosity to these used in permeability tests are prepared using the same sample preparation method and scanned using Micro-CT scanner. The pore size distributions of these specimens are computed using the image analysis method presented in Section 6.3. This information summarized in Table 6.5 is used as input for the PNM simulations to determine the permeability of different materials.

6.4.1 Isotropic specimens

Two specimens made of Sand O and Sand L are examined in this section. The properties of the fluid and the cubic lattice used in the PNM simulations are listed in Table 6.6.

Table 6.6 Input parameters of the material being investigated

Materials	ϕ	d_{mean} (mm)	c_v	NP	θ (°)	μ (Pa s)	ρ (kg/m^3)	T (N/s)
Sand O	0.351	0.160	0.5752	11	27	0.001	1000	7.29E-02
Sand L	0.397	0.114	0.6240	11	27	0.001	1000	7.29E-02

Fig. 6.11 presents the PNM simulation results for Sand O and Sand L. The computed hydraulic conductivity is plotted against the degree of saturation. The experimental hydraulic conductivity of saturated specimens is also presented for the purpose of comparison. For Sand O, the ultimate hydraulic conductivity (0.41mm/s) when S_r approaches 100% is slightly higher than experimental value (0.39 ± 0.001mm/s). However,

the simulation result (0.28mm/s) of Sand L nearly saturated is lower than the corresponding experimental hydraulic conductivity (0.30±0.005mm/s).

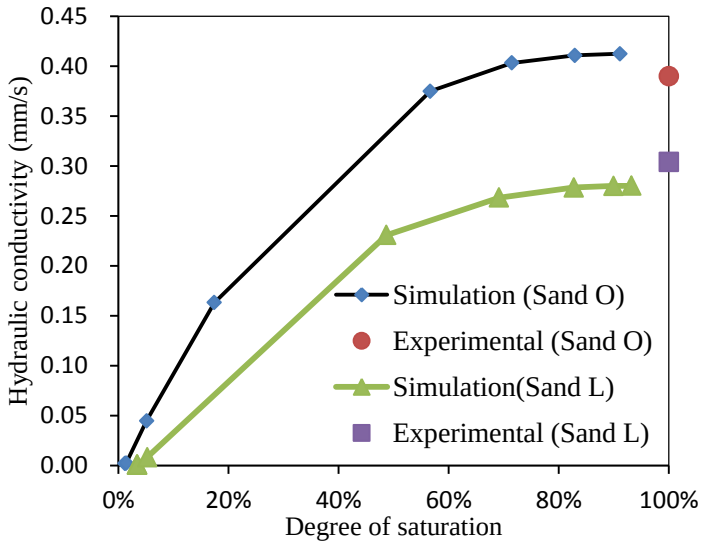

Fig. 6.11 Hydraulic conductivity results from experiments and simulations

There are several possible sources of error when using the PNM to simulate flow in porous media:

1) The information of pore size distribution is derived from separate specimens that may not exactly be the same as the specimens used in permeability tests. Although effort has been made to reproduce the specimens used in permeability tests, it is inevitable to have some differences between any two specimens;

2) The process for internal structure reconstruction and image analysis may induce some errors in characterizing the internal structure of a specimen. For instance, the obtained CT images always have some noises, even though it is minimized by applying

noise filtering algorithms;

3) The pipe network model used in this study employs three dimensional cubic lattice network. The direction of flow is restricted in three orthogonal directions. In reality, however, the "pipes" are curved and randomly interconnected. This can be improved by modifying the algorithm to construct the pipe network directly from the internal structure of pores obtained from digital image analysis. For example, rather than having regularly positioned nodes and pipes, their locations can be determined directly from the CT-scan images. In addition, instead of using fixed pipe diameter and length for a pipe segment between two lattice layers, the length and diameter of a pipe between two nodes can be made varying in space.

6.4.2 Anisotropic materials

The anisotropy of fluid flow through Ottawa Sand (Sand O) and Lentils is simulated using PNM. The information of pore structure, i.e., the mean pore size and coefficient of variation in the principal material directions, was obtained from digital image analysis and summarized in Table 6.5. The results from PNM simulations for flow in different directions are summarized in Table 6.7.

As shown in Table 6.7, for saturated Sand O specimens the values of hydraulic conductivity from experiments and PNM simulations are comparable. The calculated anisotropic permeability ratio, which is defined as the ratio of the hydraulic conductivity

in the bedding plane to that normal to the bedding plane, is also reasonable. The hydraulic conductivity of Eaton Lentils obtained from the simulations is on the same order with laboratory measurements, but the experimental results are 3.6~3.7 times of the simulation results. The anisotropic ratio, on the other hand, is comparable with the experimental result. One possible reason causing the discrepancy between simulation and experiments is that the PNM considers the pore structure as circular pipe which has a shape factor of 2. Because the Lentils are flat in shape, the cross section of the resulting pores is more like triangle which has a shape factor about 1.65 (Bear and Bachmat 1990). According to the theory in Chapter 5 (Eq.(5.60)), the increase of shape factor will lead to lower hydraulic conductivity.

Table 6.7 Anisotropic permeability of Ottawa sand and Lentils

Material	Method	e	K_h (mm/s)	K_v (mm/s)	K_h / K_v
Sand O	Experiments	0.54±0.002	0.543±0.001	0.467±0.010	1.13-1.19
	PNM (S_r≈93.6%)	0.568	0.681	0.555	1.23
Lentils	Experiments	0.531±0.002	0.598±0.059	0.400±0.031	1.25-1.78
	PNM (S_r≈94.4%)	0.550	0.161	0.110	1.46

Note: K_h and K_v represent the hydraulic conductivity in and normal to the bedding plane respectively.

In the following section, this method will be used to simulate some reported problems in the literature to verify its feasibility when the pore sizes are in different ranges.

6.5 Comparison with data in the literature

This section utilizes data in the literature to verify the feasibility of the PNM model in predicting the permeability of porous materials. More specifically, an asphalt concrete (Gruber et al., 2012) having large pores and a peat material (Rezanezhad et al., 2010) with very small pores are used for the verification.

The asphalt concrete examined is made of coarse and fine aggregates, pores and bituminous binder, mainly used for road pavement. The experimental and numerical results by Gruber et al. (2012) show that the asphalt concrete is highly anisotropic in terms of hydraulic conductivity and the anisotropic permeabiltiy ratio is around two. Six cylindrical specimens with 15cm diameter were investigated in their work but only one cross section CT image is available in their paper, i.e., slice No. 50 from a stack with total of 80 images from sample Nr. 15, as shown in Fig. 6.12.

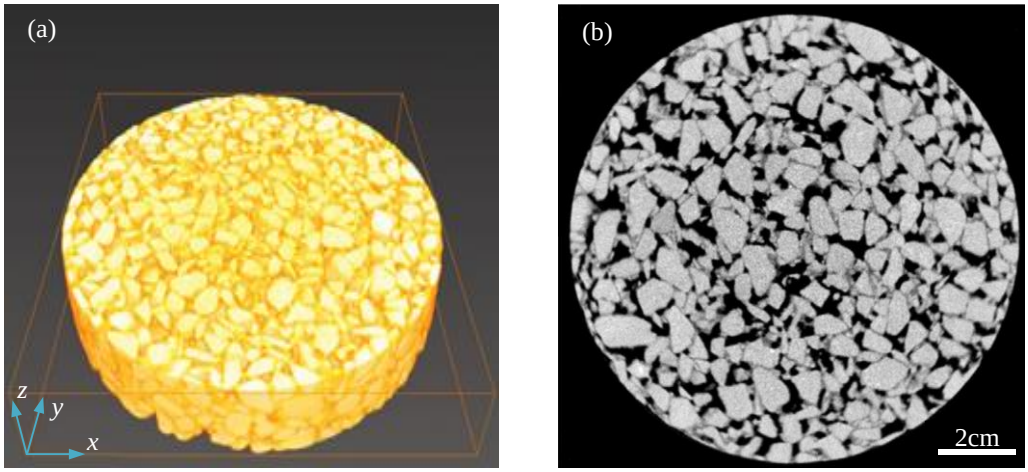

Fig. 6.12 (a) 3D reconstruction of the solid phase in CT-scan from sample Nr. 15 (diameter 15cm); (b) a 2D slice image of the sample Nr. 15. Reproduced from Gruber et al. (2012)

Following the procedures stated in previous sections, using the CT scan image in Fig. 6.12(b), characteristics of the asphalt concrete specimens are determined as: d_{mean}=0.74mm, c_v=0.665. Fig. 6.13 presents the PNM simulation results and the result from CFD for saturated specimens.

In the experimental work of Gruber et al (2012), permeability test was only conducted for flow in *z* direction, i.e., direction of the axis of symmetry. The hydraulic conductivity in the *x*-o-*y* plane is not available. In this study, however, it is only possible to evaluate the hydraulic conductivity based on cross section CT image in *x*-o-*y* plane. Our results are compared with their simulation results using Computation Fluid Dynamics (CFD) for flow in *x*-O-*y* plane, as shown in Fig. 6.13. Good agreement is found between the result by PNM and CFD. In Gruber's work, 2,500,000 elements are used, which is very computation effort intensive. However, only 4,752 elements are used in PNM simulations and the computation time is less than 5 seconds.

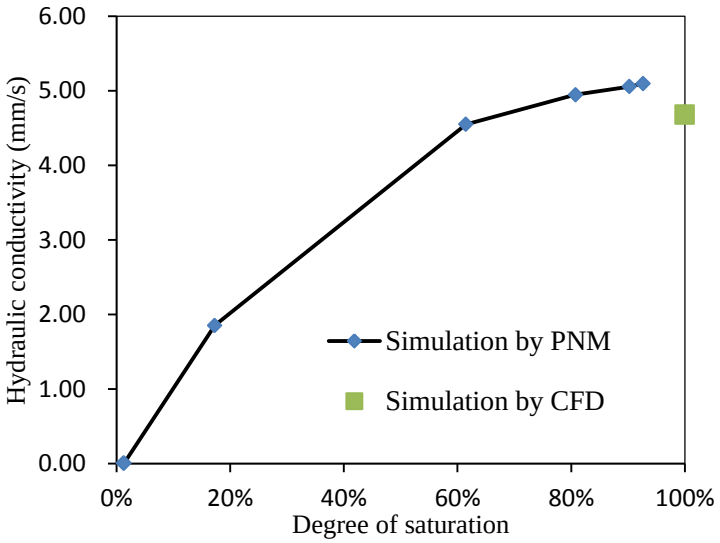

Fig. 6.13 Hydraulic conductivity results from experiment and simulation (Asphalt concrete).

The peat investigated by Rezanezhad et al. (2010) has large pores and the total porosity can go up to 90%. However, the plant tissues tend to segment the pores into very small parts, producing closed and dead-end pores that do not conduct water. In addition, the natural deposition and layering process may lead to inhomogeneous and anisotropic pore network. The detailed properties of the material can be found in Rezanezhad et al. (2010).

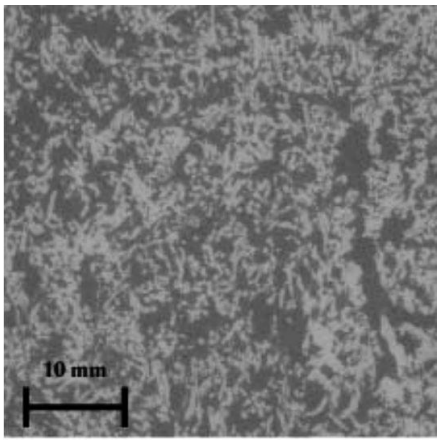

Fig. 6.14 2D CT image from a peat sample (reproduced from Rezanezhad et al., 2010)

One of the CT images (Fig. 6.14) in Rezanezhad et al. (2010) is utilized to characterize the pore structure of the material. It is a 2D cross section CT image of the sample from the depth of 61~67cm underneath the ground surface. For this set of samples, the unsaturated hydraulic conductivity is determined experimentally as K=4.7$\times$10^{-7}m/s and the degree of saturation is 46.7%. The developed image analysis code in this study is applied and the mean pore size is computed as d_{mean}=0.41mm with the coefficient of variation being c_v=0.64. A series of simulations were conducted and the hydraulic conductivity at S_r=46.7% was obtained as 2.8$\times$10^{-3}m/s. It is way off the experimental result (4 orders higher). There might be three possible reasons:

1) The image used in this study is captured from the paper of which the resolution has been significantly reduced from the original one. Therefore, the smaller pores were smoothed out or hard to be distinguished from the surrounding pixels. This will lead to an over-estimated mean diameter. The image analysis result by Rezanezhad et al. (2010)

indicates that the hydraulic diameter is around 0.11mm, which is only 26.7% of that obtained by this study.

2) The pore structure is highly inhomogeneous and anisotropic. Important assumptions made in PNM are that the pore network is homogeneous and the pore size distribution follows a lognormal distribution. The pore network of the cubic lattice is generated randomly based solely on d_{mean} and c_{v}. If the actual pore network is inhomogeneous, it is impossible to reproduce the pore structure using the above two parameters only. Therefore, one possible improvement on the current PNM lies in the generation of cubic lattice. Rather than reconstructing a pore network based on the statistical data of the CT images, it might be more accurate and reliable to construct one directly from the CT images. Specifically, the local void ratio can be captured following a similar method proposed by Frost and Kuo (1996). Since the local porosity is a normalized quantity reflecting the relative changes of pore size, it can be treated as a measure of the pipe diameter. By multiplying a coefficient to all local porosity, the overall porosity can be satisfied. In this manner, not only the anisotropy of the structure can be captured, but also the heterogeneity may be can be modelled properly.

3) The mechanisms of unsaturated fluid flow is different from that assumed in PNM, even though follows a similar decreasing trend when the degree of saturation reduces.

6.6 Summary

1) Within the framework of the pipe network model and the percolation theory, an integrated methodology is developed to evaluate the hydraulic properties of porous media based on the microstructure obtained from CT scans. Both the average and the variation of pore sizes are taken into account when constructing the pipe network model. It is proven that the hydraulic conductivity cannot be uniquely determined from the mean pore size (or the diameter of the pipes). The variation of the pore size also has significant effect on the calculated hydraulic conductivity;

2) A new method is proposed to compute the pore size distribution based on CT-scan images. This method is advantageous over the traditional Mercury Intrusion Test in several aspects. For example, the new method is non-destructive and poison free. Another more important merit is that the new method is able to obtain the pore size distribution in different directions;

3) With proper pore structure information obtained from the re-construction of pore structures, the method is capable of capturing the hydraulic conductivity of anisotropic porous media. It should be emphasized that any successful use of the proposed methodology highly depends on reliable description of pore structures, including both the mean pore size and its variation;

4) The pipe network model is able to capture the intrinsic permeability of porous

media which is solely a function of pore structure;

5) Since the pipe network model is able to compute the hydraulic conductivity when the system is not fully saturated, it gives a possibility to apply this method to simulated flow in unsaturated porous materials;

6) The proposed methodology is verified with laboratory tests on different materials and data in the literature, with some limitations being identified;

7) It should be noted that cubic lattice networks are used in this study to simulate flow in the principal material directions. In other words, only the principal components of the permeability tensor are determined. Comparing with the theoretical approach in Chapter 5, the variability of the pore size is taken into account explicitly, while the direction variation of pore size is only taken into account in the principal directions.

Chapter 7 Conclusions and recommendations for future work

7.1 Conclusions

In this study, the main focus has been placed on the quantification of the permeability of porous media with internal structures. The starting point is the reconstruction and the characterization of the pore structure of the material. Then the macroscopic permeability is related to the internal structure using different approaches, including laboratory tests, theoretical analysis using the theory of homogenization, and modelling using Pipe Network Model. The following conclusions can be made based on the research accomplished in this thesis:

1) A new permeameter is designed to prepare specimens of cohesionless materials with different bedding plane inclination angles to carry out permeability tests in which the direction of pressure gradient is different from the principal direction of the materials. This device is required for laboratory determination of anisotropic permeability of granular materials;

2) The hydraulic conductivity of Ottawa Sand C109 (Sand O) and Eaton Lentils are investigated using the newly designed permeameter. Using sand rain method to prepare the specimens, they both display anisotropy in terms of hydraulic conductivity. The

anisotropic permeability ratio is in the range of 1.13~1.19 for Sand O and 1.25~1.78 for Eaton Lentils. The particle shape and particle aspect ratio has significant influence on the anisotropic ratio of hydraulic conductivity;

3) A new procedure is established to reconstruct the microstructure of a porous material using 3D CT-scan images. A new algorithm is developed to quantify the internal structure based on the 3D CT-scan images. More specifically, two fabric descriptors, Mean Intercept Length and Areal Pore Size, are employed to construct fabric tensors as measures to the internal structure;

4) The internal structure of specimens made of Sand O, Sand L (crushed limestone) and Eaton Lentils are obtained using Micro-CT scanner and the new algorithm developed in this study. Cross anisotropy is found in Sand O and Eaton Lentils specimens fabricated using the method of sand rain. The axis of symmetry is the normal of the bedding plane. For a given material, the fabric tensor constructed by Mean Intercept Length displays greater degree of anisotropy than that by Areal Pore Size. It is also found that the fabric tensor of Eaton Lentils consisting of lenticular particles is greater than that of Sand O of which the particles are mainly rounded or sub-rounded;

5) An analytical model is developed to describe flow in porous medium with internal structures using the technique of homogenization. With the fluid-solid interaction taking into account on the particle level, the permeability tensor of a porous medium is

derived from the macroscopic momentum balance equation of the fluid. The microstructure of the porous media is characterized by fabric tensors defined by Mean Intercept Length and Area Pore Size, which are measures for pore structures. The results obtained from the theoretical model and a simplified model are in good agreement with laboratory test data;

6) Pipe Network Model can also be used to determine the permeability of granular materials when the pore structure is properly characterized. Different from fabric tensors that focus on directional variation of pore spaces on the average meaning, classical Pipe Network Models consider the entire pore size distribution characterized by the average and the standard variation rather than the directional variation of pore voids. The microstructure reconstruction using 3D CT-scan images can provide all information required by the pipe network model. A new algorithm is developed to compute the pore size distribution of porous media based on the CT images;

7) When taking into account the directional variation of pore size distributions, PNM can be used to determine the principal permeability of an anisotropic porous material. The success of this approach highly depends on reliable characterization of pore structures.

7.2 Recommendations for future work

1) The Mean Intercept Length (*MIL*) is referred to as the mean value of the

intercept length in a given direction. For flow in porous media, the variation of pore size in a specific direction instead of the mean is important. Hence, if the directional variation of deviation of pore size from the mean could be incorporated in the construction of the fabric tensor, an improved constitutive model could be obtained;

2) More general procedure to reconstruct 3D structures of porous media (including dense packing of granular particles) needs to be developed to verify the methods of microstructure quantification and the analytical model developed in this thesis. With high-quality 3D image of pore structures, it is possibly to carry out Finite Element Method simulations to compute the hydraulic conductivity directly and to verify the analytical model in this thesis;

3) Instead of reconstructing a 3D cubic lattice pore network based on the statistical data of the CT-scan images, it might be more accurate and reliable to construct an irregular pore network model directly from the CT-scan images;

4) It is necessary to extend the analytical model developed in this thesis to induced anisotropy of hydraulic conductivity of porous media. More materials and tests should be performed to verify the model.

References

Adler, P. M., Jacquin, C. and Quiblier, J. 1990. "Flow in simulated porous media". International Journal of Multiphase Flow. 16 (4): 691-712.

Adler, P. M. 1992. "Porous media: geometry and transports". Boston: Butterworth-Heinemann.

Ahmadi, M., Mohammadi, S. and Hayati, A. 2011. "Analytical derivation of tortuosity and permeability of monosized spheres: A volume averaging approach". Physical Review E. 83 (2) (February): 026312.

Alam, P., Byholm, T. and Toivakka, M. 2006. "Calculating tortuosity in quasi-random anisotropic packings". Nordic Pulp & Paper Research Journal. 21 (5): 670-675.

Alshibli, K. A., Batiste, S. N., Swanson, R.A., Sture, S., Costes, N. C. and Lankton, M. R. 2000. "Quantifying void ratio variation in sand using computed tomography". Geotechnical Special Publication. 106: 30-43.

Altuhafi F., Sullivan, O. C., and Cavarretta, I. 2013. "Analysis of an image-based method to quantify the size and shape of sand particles". Journal of Geotechnical and Geoenvironmental Engineering. 139 (8): 1290-1307.

ASTM Committee D-18 on Soil and Rock. 2007. "Standard test method for particle-size analysis of soils". Philadelphia, Pa: ASTM International.

ASTM Committee D-18 on Soil and Rock. 2010. "Standard test methods for specific gravity of soil solids by water pycnometer". Philadelphia, Pa: ASTM International.

ASTM Committee D-18 on Soil and Rock. 2006. "Standard test method for permeability of granular soils (constant head) ". Philadelphia, Pa: ASTM International.

Aydilek, A. H., Seyfullah, Oguz, H., and Tuncer, B. E. 2002. "Digital image analysis to determine pore opening size distribution of nonwoven geotextiles". Journal of Computing in Civil engineering .16 (4): 280-290.

Bachmat, Y., Bear, J. 1986. "Microscopic modelling of transport phenomena in porous media". I: the continuum approach. Transp. Porous Media 1, 213-240.

Bear, J., Bachmat, Y. 1990. "Introduction to Modelling of Transport Phenomena in Porous Media". Kluwer Academic Publishers, Dordrecht.

Bear, J. 1991. "Introduction to Modeling of Transport Phenomena in Porous Media". Dordrecht; Boston: Kluwer Academic Publishers.

Bear, J. 1972. "Dynamics of fluids in porous media". New York: American Elsevier Pub. Co.

Bernhoft, R. A. 2011. "Mercury toxicity and treatment: a review of the literature." Journal of environmental and public health 2012.

Beucher, S. and Lantuejoul, C. 1979. "Use of watersheds in contour detection". Rennes, France: CCETT; 1979.

Bird, R., Byron, Stewart, W. E. and Lightfoot, E.N. 2007. "Transport phenomena". New York: J. Wiley.

Bolton, A. J., Maltman, A. J., and Fisher, Q. 2000. "Anisotropic permeability and bimodal pore-size distributions of fine-grained marine sediments". Marine and Petroleum Geology. 17 (6): 657-672.

Bourbie, T., and Zinszner, B. 1985. "Hydraulic and acoustic properties as a function of porosity in Fontainebleau sandstone". Journal of Geophysical Research: Solid Earth (1978–2012). 90 (B13): 11524-11532.

Broshtein, I. N., Semendyayev, K.A. and Musiol, G. 2012. "Handbook of mathematics". 5th ed. [S.l.]: Cram101.

Brun, M., Lallemand, A., Quinson, J. F., and Eyraud, C. 1977. "A new method for the simultaneous determination of the size and shape of pores: the thermoporometry". Thermochimica Acta. 21 (1): 59-88.

Carman, P. C. 1937. “Fluid flow through granular beds. Transactions-Institution of Chemical Engineeres”. 15: 150-166.

Chapuis, R.P. 2012. "Predicting the saturated hydraulic conductivity of soils: A review". Bulletin of Engineering Geology and the Environment. 71 (3): 401-434.

Chapuis, R. P., and Denis, E. G. 1989. "Hydraulic anisotropy of homogeneous soils and rocks: influence of the densification process". Bulletin of the International Association of Engineering Geology. 39 (1): 75-86.

Chapuis, R. P., Baass, K. and Davenne, L. 1989. "Granular soils in rigid-wall permeameters: method for determining the degree of saturation". Canadian Geotechnical Journal. 26 (1): 71-79.

Chatterji, S. 2001. "A discussion of the paper “Mercury porosimetry—an inappropriate method for the measurement of pore size distributions in cement-based materials” by S. Diamond". Cement and Concrete Research. 31 (11): 1657-1658.

Chatzis, I., and Dullien, F. 1977. "Modelling pore structure by 2-D and 3-D networks with application to sandstones". Journal of Canadian Petroleum Technology.

Childs, E. C., and Collis-George, E. 1950. "The permeability of porous materials." Proceedings of the Royal Society of London. Series A. Mathematical and Physical Sciences. 201 (1066): 392-405.

Das, B. M. 1983. "Advanced Soil Mechanics ". Mc-GrawHill, New York.

Deans, S. R. 1983. “The Radon transform and some of its applications”. New York: Wiley.

Diamond, S. 1971. "A critical comparison of mercury porosimetry and capillary condensation pore size distributions of portland cement pastes." Cement and concrete research. 1 (5): 531-545.

Diamond, S. 2000. "Mercury porosimetry: an inappropriate method for the measurement of pore size distributions in cement-based materials." Cement and Concrete Research. 30 (10): 1517-1525.

Diaz, C.E., Chatzis, I. and Dullien, F.A.L. 1987. "Simulation of capillary pressure curves using bond correlated site percolation on a simple cubic network". Transport in Porous Media. 2 (3).

Dullien, F. A. L. 1979. “Porous media: fluid transport and pore structure”. New York: Academic Press.

Dullien, F. A. L. 1991. “Porous media: fluid transport and pore structure”. Academic press.

Edén, M. 1999. “Solid State NMR of Multiple-spin Systems”. Stockholm.

Elliott, J.C. and Dover, S. D. 1982. "X-ray microtomography". Journal of Microscopy. 126: 211-3.

Epstein, N. 1989. "On tortuosity and the tortuosity factor in flow and diffusion through porous media". Chemical Engineering Science. 44 (3): 777-779.

Escobar, F., Cubillos, J. and Montealegrem, M. 2008. "Estimation of horizontal reservoir anisotropy without type-curve matching". Journal of Petroleum Science and Engineering. 60 (1): 31-38.

Feldkamp, L. A., Goldstein, S. A., Parfitt, M.A., Jesion, G. and Kleerekoper, M. 1989. "The direct examination of three-dimensional bone architecture in vitro by computed tomography". Journal of Bone and Mineral Research. 4 (1): 3-11.

Feng, Y., and Yu, B. 2007. "Fractal dimension for tortuous streamtubes in porous media". Fractals. 15 (04): 385-390.

Fontugne, D. J. 1969. “Permeability measurement in anisotropic media”. Thesis (M.S.)--Syracuse University.

Freeze, R. A., and Cherry, J. A. 1979. “Groundwater”. Englewood Cliffs, N.J.: Prentice-Hall.

Frost, J. D., and Kuo, C. 1996. "Automated Determination of the Distribution of Local Void Ratio from Digital Images". Geotechnical Testing Journal. 19 (2): 107.

Galindo-Torres S. A., Scheuermann, A. and Li, L. 2012. "Numerical study on the permeability in a tensorial form for laminar flow in anisotropic porous media". Physical Review. E, Statistical, Nonlinear, and Soft Matter Physics. 86 (4).

Ghedia, R., and O'Sullivan, C. 2012. "Quantifying void fabric using a scan-line approach". Computers and Geotechnics. 41: 1-12.

Giesche, H. 2006. "Mercury porosimetry: a general (practical) overview." Particle & particle systems characterization. 23 (1): 9-19.

Goldman, L.W. 2007. "Principles of CT and CT technology". Journal of Nuclear Medicine Technology. 35 (3): 115-28.

Gommes, C. J., Bons, J., Blacher, S. Dunsmuir, J.H. and Tsou, A. H. 2009. "Practical methods for measuring the tortuosity of porous materials from binary or gray‐tone tomographic reconstructions". AIChE journal. 55 (8): 2000-2012.

Gruber, I., Zinovik, I., Holzer, L., Flisch, A. and Poulikakos, L.D. 2012. "A computational study of the effect of structural anisotropy of porous asphalt on hydraulic conductivity". Construction and Building Materials. 36: 66-77.

Guo, P., and Su, X. 2007. "Shear strength, interparticle locking, and dilatancy of granular materials". Canadian Geotechnical Journal. 44 (5): 579-591.

Guo, P. 2008. "Modified Direct Shear Test for Anisotropic Strength of Sand". Journal of Geotechnical and Geoenvironmental Engineering. 134(9): 1311-1318.

Guo, P. 2012. "Dependency of Tortuosity and Permeability of Porous Media on Directional Distribution of Pore Voids". Transport in Porous Media. 95 (2): 285-303.

Harr, M. E. 1962. “Groundwater and Seepage”. New York: McGraw-Hill.

Harr, M. E. 1977. "Mechanics of particulate media: a probabilistic approach". New York: McGraw-Hill.

Allen, H. 1911. “Discussion of ‘Dams on sand foundations’”. Transactions. ASCE. 73: 199 -203.

Herman, G. T. 2009. “Fundamentals of computerized tomography image reconstruction from projections”. Dordrecht: Springer.

Herzer, G. "Grain size dependence of coercivity and permeability in nanocrystalline ferromagnets." Magnetics, IEEE Transactions on 26, no. 5 (1990): 1397-1402.

Hillel, Daniel. 1980. "Fundamentals of soil physics". New York: Academic Press.

Hillel, Daniel. 2003. "Introduction to environmental soil physics". Academic press.

Hsieh, J. 2009. “Computed tomography: principles, design, artifacts, and recent advances”. Hoboken, N.J.: Wiley Interscience.

Ho, F., and Striender, W. 1981. "A variational calculation of the effective surface diffusion coefficient and tortuosity". Chemical Engineering Science. 36 (2): 253-258.

Inglis, D. 2001. “Description of anisotropic properties of trabecular bone”. Thesis (Ph. D.)--McMaster University.

Inglis, D., and Pietruszczak, S. 2003. "Characterization of anisotropy in porous media by means of linear intercept measurements". International Journal of Solids and Structures. 40 (5): 1243-1264.

Currie, J. A. 1960. "Gaseous diffusion in porous media. Part 2. - Dry granular materials". British Journal of Applied Physics. 11 (8): 318-324.

Darcy, H. 1856. “Les Fontaines publiques de la ville de Dijon ; Exposition et application des principes à suivre et des formules à employer dans les questions de distribution d'eau”. Paris: V. Dalmont.

Juang, C. H., and Holtz, R. D. 1986. "A probabilistic permeability model and the pore size density function." International Journal for numerical and analytical methods in geomechanics. 10 (5): 543-553.

Katz, A. J., and Thompson, A. H. 1986. "Quantitative prediction of permeability in porous rock." Physical review B. 34 (11): 8179-8181.

Kaye, P. H., Alexander, K., Hirst, E., Saunders, S. and Clark, J. M. 1996. "A real-time monitoring system for airborne particle shape and size analysis". Journal of Geophysical Research: Atmospheres (1984–2012). 101 (D14): 19215-19221.

Kenoyer, G. J. 1988. "Tracer test analysis of anisotropy in hydraulic conductivity of granular aquifers". Groundwater Monitoring & Remediation. 8 (3): 67-70.

Ken-Ichi, K. 1984. "Distribution of directional data and fabric tensors". International Journal of Engineering Science. 22 (2): 149-164.

Koponen, A., Kataja, M. and Timonen, J. 1996. "Tortuous flow in porous media". Physical Review E. 54 (1): 406-410.

Koza, Z., Matyka, M. and Khalili, A. 2009. "Finite-size anisotropy in statistically uniform porous media". Physical Review. E, Statistical, Nonlinear, and Soft Matter Physics. 79 (6).

Kozeny, J. 1927. “Über Kapillare Leitung Des Wassers Im Boden (Aufstieg, Versickerung U. Anwendung Auf Die Bewässerg) Gedr. Mit Unterstützg Aus D. Jerome U. Margaret Stonborsugh-Fonds”. Wien: Hölder-Pichler-Tempsky A.-G. [Abt.] Akad. d. Wiss.

Kralj, B., and Pande, G. N.. 1994. A stochastic model for the permeability characteristics of saturated porous media undergoing freezing. Swansea: University of Wales Swansea, Dept. of Civil Engineering.

Kriss, T. C., and Kriss, V. M. 1998. "History of the operating microscope: from magnifying glass to microneurosurgery". Neurosurgery. 42 (4): 899-907.

Kuo, C.Y., Frost, J. D. and Chameau, J. L. A. 1998. "Image analysis determination of stereology based fabric tensors". GEOTECHNIQUE. 48 (4): 515-526.

Kurzydlowski, Jan, K., and Ralph, B. 1995. “The quantitative description of the microstructure of materials”. Vol. 3. CRC press, 1995.

Latini, R. G. 1967. “Measurement of directional permeabilities”. Thesis (M.S.)--Syracuse University.

Leroueil, S., Bouclin, G., Tavenas, F., Bergeron, L. and Rochelle, P. L. 1990. "Permeability anisotropy of natural clays as a function of strain". Canadian Geotechnical Journal. 27 (5): 568-579.

Liakopoulos, A. C. 1965. "Darcy's hydraulic conductivity as symmetric tensor of second rank". International Association of Scientific Hydrology. Bulletin. 10 (3): 41-48.

Li, B., Wong, R.C.K. and Milnes, T. 2014. "Anisotropy in capillary invasion and fluid flow through induced sandstone and shale fractures". International Journal of Rock Mechanics and Mining Sciences. 65: 129-140.

Lim, J. S. 1990. "Two-dimensional signal and image processing". Englewood Cliffs, N.J.: Prentice Hall.

Liu, S. H., and Matsuoka, H. 2003. "Microscopic interpretation on a stress-dilatancy relationship of granular materials". Soils and Foundations. 43 (4): 73.

Lowenfels, J. and Lewis, W. 2010. "Teaming with microbes: the organic gardener's guide to the soil food web". Portland, Or: Timber Press.

Marshall, T. J. 1958. "A relation between permeability and size distribution of pores". Journal of Soil Science. 9 (1): 1-8.

Masad, E., and Muhunthan, B. 2000. "Three-dimensional characterization and simulation of anisotropic soil fabric". Journal of geotechnical and geoenvironmental engineering. 126: 199-207.

Matthews, G. P., Moss, A. K., Spearing, M. C. and Voland, F. 1993. "Network calculation of mercury intrusion and absolute permeability in sandstone and other porous media". Powder technology. 76 (1): 95-107.

Mas-Pla, J., Yeh, T. C. J., Williams, T. M. and McCarthy, J. F. 1997. "Analyses of slug tests and hydraulic conductivity variations in the near field of a two-well tracer experiment site". Groundwater. 35 (3): 492-501.

Mauret, E., and Renaud, M. 1997. "Transport phenomena in multi-particle systems-I. Limits of applicability of capillary model in high voidage beds-application to fixed beds of fibers and fluidized beds of spheres". Chemical engineering science .52 (11): 1807-1817.

Meegoda, N. 1989. “An expression for the permeability of anisotropic granular media”. International Journal for Numerical and Analytical Methods in Geomechanics. 13 (6): 575 – 598.

McGlinchey, D. 2005. "Characterisation of bulk solids". Oxford: Blackwell.

Millington, R. J., and Quirk, J. P. 1961. "Permeability of porous solids". Transactions of the Faraday Society. 57: 1200-1207.

Mitchell, J.K. 1993. “Fundamentals of soil behaviour”. New York,N.Y.: Wiley.

Mitchell, J. K. and Soga, K. 2005. “Fundamentals of soil behavior”. Hoboken, N.J.: John Wiley & Sons.

Mitchell, J., Webber, J. W. B. and Strange, J. H. 2008. "Nuclear magnetic resonance cryoporometry". Amsterdam [u.a.]: Elsevier.

Miura, Kinya, Maeda, K., Furukawa, M. and Toki, S. 1997. "Physical characteristics of sands with different primary properties". Soils and Foundations. 37 (3): 53.

Moore, P. 1981. "Determination of permeability anisotropy in a two-way permeameter. Technical note Geotech Test J, V2, N3, Sept 1979, P167–169". International Journal of Rock Mechanics and Mining Sciences & Geomechanics Abstracts. 18 (1): 7-7.

Muhunthan, B, Masad, E. and Assaad, A. 2000. "Measurement of uniformity and anisotropy in granular materials". Geotechnical Testing Journal. 23 (4): 423.

Nakao, S. 1994. "Determination of pore size and pore size distribution: 3. Filtration membranes". Journal of Membrane Science. 96 (1): 131-165.

Oda, M. 1985. "Stress-induced anisotropy in granular masses". Soils and foundations. 25 (3): 85 – 97.

Odong, J. 2007. "Evaluation of empirical formulae for determination of hydraulic conductivity based on grain-size analysis". Journal of American Science. 3 (3): 54-60.

Otsu, N.. 1979. "A threshold selection method from gray-level histograms". IEEE Transactions on Systems, Man, and Cybernetics. 9 (1): 62-66.

Parra, J. O. 2000. "Poroelastic model to relate seismic wave attenuation and dispersion to permeability anisotropy". GEOPHYSICS. 65 (1): 202-210.

Phillips, D. 1997. "Measuring physical density with X-ray computed tomography". NDT & E International. 30 (6): 339-350.

Pietruszczak, S., and Inglis, D. 2003. “Characterization of anisotropy in porous media by means of linear intercept measurements”. International Journal of Solids and Structures”. 40: 1243-1264.

Pietruszczak, S. and Pande, G. 2012. “Description of hydraulic and strength properties of anisotropic geomaterials”. Studia Geotechnica et Mechanica, 34 (3): 3-72.

Renard, Philippe, Genty, A., and Stauffer, F. 2001. "Laboratory determination of the full permeability tensor". Journal of Geophysical Research: Solid Earth. 106 (B11): 26443-26452.

Revil, A. and Cathles, L. M. 1999. "Permeability of shaly sands". Water Resources Research. 35(3): 651-662.

Rezanezhad, F., Quinton, W.L., Price, J.S., Elliot, T.R., Elrick, D. and Shook, K.R. 2010. "Influence of pore size and geometry on peat unsaturated hydraulic conductivity computed from 3D computed tomography image analysis". Hydrological Processes. 24 (21): 2983-2994.

Rice, P. A., Fontugne, D. J., Latini, R. G., and Barduhn, A. J. 1970. "Anisotropic permeability in porous media". Industrial & Engineering Chemistry. 62 (6): 23-31.

Sahimi, M. 1988. "Diffusion-controlled reactions in disordered porous media-I. Uniform distribution of reactants". Chemical engineering science. 43 (11): 2981-2993.

Salem, Hilmi, and Chilingarian, G. 2000. "Influence of porosity and direction of flow on tortuosity in unconsolidated porous media". Energy Sources. 22 (3): 207-213.

Scheidegger, A. E. 1974. "The physics of flow through porous media". Toronto: University of Toronto Press.

Scholes, O. N., Clayton, S.A., Hoadley, A. F. A. and Tiu, C. 2007. "Permeability anisotropy due to consolidation of compressible porous media". Transport in Porous Media. 68 (3): 365–387.

Schopper, J. R. 1966. "A theoretical investigation on the formation factor/permeability/porosity relationship using a network model". Geophysical Prospecting. 14 (3): 301-341.

Seiyama, T., Yamazoe, N. and Arai, H. 1983. "Ceramic humidity sensors". Sensors and Actuators. 4: 85-96.

Shepherd, R. G. 1989. "Correlations of permeability and grain size". Groundwater. 27 (5): 633-638.

Shinohara, K. and Ramey, H. J. 1979. "Analysis of "Slug Test" Dst flow period data with critical flow". Society of Petroleum Engineers.

Smit, V. 1998. "Star length distribution: a volume-based concept for the characterization of structural anisotropy". Journal of Microscopy. 191 (3): 249-257.

Stewart, M.L., Ward, A.L. and Rector, D.R. 2006. "A study of pore geometry effects on anisotropy in hydraulic permeability using the lattice-Boltzmann method". Advances in Water Resources. 29 (9): 1328-1340.

Sutera, S. 1993. "The history of poiseuille's law". Annual Review of Fluid Mechanics. 25 (1): 1-19.

Taylor, D. W. 1948. "Fundamentals of Soil Mechanics". New York, Jhon Wiley & Sons, Inc.

Tiedje, E.W. and Guo, P. 2014. "Modeling the influence of particulate geometry on the thermal conductivity of composites". Journal of Materials Science. 49 (16): 5586-5597.

Wan, R. G., and Guo, P. 2001. "Effect of microstructure on undrained behaviour of sands". Canadian Geotechnical Journal. 38 (1): 16-28.

Washburn, E. 1921. "The dynamics of capillary flow". Physical Review. 17 (3): 273-283.

Weeks, E. P. 1969. "Determining the Ratio of Horizontal to Vertical Permeability by Aquifer-Test Analysis". Water Resources Research. 5 (1): 196-214.

Whitaker, S. 1999. "The method of volume averaging". Dordrecht: Kluwer Academic.

White, D. J. 2003. "PSD measurement using the single particle optical sizing (SPOS) method". GEOTECHNIQUE -LONDON-. 53: 317-326.

Winsauer, W. O., Shearin, H. M., Masson, P. H. and Williams, M. 1952. "Resistivity of brine-saturated sands in relation to pore geometry". AAPG bulletin. 36 (2): 253-277.

Wong, R. C. K. and Li, Y. 2000. "A Stress-Dependent Model for Permeability Changes in Oil Sand Due to Shear Dilation". Evaluation.

Wong, R. C. K. and Li, Y. 2000. "A stress-dependent model for permeability changes in oil sand due to shear dilation". In Canadian International Petroleum Conference. Petroleum Society of Canada.

Wyckoff, R. D., and Botset, H. G. 1936. "The flow of gas-liquid mixtures through unconsolidated sands". Physics. 7 (9): 325.

Wyllie, M. R. J. 1954. "The fundamentals of electric log interpretation". New York: Academic Press.

Zhao, C., Zhou, X., and Yue, Y. 2000. "Determination of pore size and pore size distribution on the surface of hollow-fiber filtration membranes: a review of methods". Desalination. 129 (2): 107-123.